APPLICATION OF METAL ORGANIC FRAMEWORKS (MOFs) TO CAPTURING CO_2 DIRECTLY FROM AIR

A Dissertation
Presented to
The Academic Faculty

by

Lalit A. Darunte

In Partial Fulfillment
of the Requirements for the Degree
Doctor of Philosophy in the
School of Chemical and Biomolecular Engineering

Georgia Institute of Technology
May 2018

APPLICATION OF METAL ORGANIC FRAMEWORKS (MOFs) TO CAPTURING CO_2 DIRECTLY FROM AIR

Approved by:

Dr. Christopher W. Jones, Advisor
School of Chemical and Biomolecular Engineering
Georgia Institute of Technology

Dr. David S. Sholl, Co-advisor
School of Chemical and Biomolecular Engineering
Georgia Institute of Technology

Dr. Krista S. Walton, Co-advisor
School of Chemical and Biomolecular Engineering
Georgia Institute of Technology

Dr. Matthew Realff
School of Chemical and Biomolecular Engineering
Georgia Institute of Technology

Dr. Ryan Lively
School of Chemical and Biomolecular Engineering
Georgia Institute of Technology

Dr. Athanasios Nenes
School of Earth and Environmental Science
Georgia Institute of Technology

Date Approved: March 26, 2018

The greatest challenge to any thinker is stating the problem in a way that will allow a solution

- Bertrand Russell

To my family

ACKNOWLEDGEMENTS

I spent a large part of the 20s at this wonderful yet competitive place called Georgia Tech and as I draw curtains to my academic life here, a reflection on many years spent is the most favorite part of my thesis. I was fortunate enough to interact with more than 100 people in my three research groups, follow different research approaches and learn from them. This thesis would not have been possible without many people and I would like to acknowledge following people and my learnings from them:

Thesis advisors:

Dr. Christopher Jones: Hard work and brilliance will allow one to scale heights that are beyond imagination.

Dr. David Sholl: Begin with the end in mind. Perfection is possible with meticulous planning.

Dr. Krista Walton: Graduate school is a fun opportunity to learn, take it with both hands.

Committee members:

Dr. Matthew Realff: System design and materials engineering go hand in hand, a perfect system is not achievable without a two-way communication.

Dr. Ryan Lively: Think big, plan well, and communicate clearly.

Dr. Athanasios Nenes: Complex problems can be solved with a simpler and fundamental analysis. There is a beauty in simplicity.

Undergraduate researchers:

Davin Oetomo, Yuri Terada, Jo Han Bin, Andrew Morris, Brandon Harris, & Chiraag Bhawanani: There is a no bigger joy than watching people grow. Communicate clearly and give freedom to smart people to achieve results.

Modeling collaborators:

Trisha Sen, Anshuman Sinha: Seamless collaboration between modeling and experimental groups is essential to unlocking a complete picture.

Jones, Walton and Sholl groups**:** Smart eco-system and critical peer-feedback pushes everybody to be their best.

Georgia Tech SGA: Passionate and committed student leaders can make a big difference in the life of a graduate student.

Pradnya Samant: An act of achieving a right balance between professional and personal life is much enjoyable with a perfect partner.

ATL friends: Thank you for great memories. It was fun exploring this great city of Atlanta.

Family: Ph.D. is teamwork with lots of tough choices and sacrifices, although my name is on the degree, the trophy belongs to my family who dreamed and supported my every effort.

Eastman Chemical: Summer 2015 fellowship is acknowledged for conference travels

National Science Foundation: CBET award 1336386 is gratefully acknowledged for graduate school funding

TABLE OF CONTENTS

LIST OF TABLES

LIST OF FIGURES

SUMMARY

The CO_2 concentration in the atmosphere has increased more than 50% in last 250 years. This increase in CO_2 concentration is also widely linked to the climate change. There is a considerable interest in developing next generation of technologies that can capture CO_2 from both concentrated feeds like power plants and dilute feeds like air at a lower cost. Current 'Amine scrubbing' technology to capture CO_2 from power plants has been around for decades and suffers from a high penalty associated with the parasitic energy to heat water in the solution.

Amine functionalized solid adsorbents are promising materials for the capture of CO_2 because of their high CO_2 adsorption capacity for a wide range of CO_2 partial pressures and lower heat capacity compared to liquid amine solutions. However, there are many challenges to overcome before a practical realization. This thesis focuses on the use of solid-supported amines for CO_2 capture, with emphasis on amine-functionalized metal-organic framework (MOF) materials. The use of MOFs as supports for amines could be a versatile approach to the creation of effective amine sorbents because of the tunability of MOF structures. Many MOFs have shown high pore volumes, open metal sites, and novel mechanisms to allow a systematic tuning to obtain a high CO_2 adsorption at ultra-dilute partial pressures. However, many considerations are required before deploying MOFs for practical applications. Firstly, MOFs candidates are required that show a high CO_2 adsorption at air capture conditions and a stable performance under humidity. Once suitable MOF candidates are identified, they need to be adapted in practical supports such as hollow fibers and honeycomb monoliths that can handle high flowrates at low pressure drops. Finally, an understanding of mass transfer and controlling resistance in the system will allow a better design of the practical system.

In the present thesis, we tested different MOF candidates based on their stability under humid conditions, open metal sites, and pore volume to identify MIL-101(Cr), Mg_2(dobpdc) and Mg-MOF-74 as suitable candidates. Functionalization of open metal sites or physical impregnation with amines are two common strategies to enhance CO_2 adsorption for direct air capture. MIL101 (Cr) was chosen for its exceptional stability under humid conditions, the presence of open metal sites, and high pore volume. This framework was functionalized with two amines tris (2-amino ethyl) (TREN) and low molecular weight, branched poly(ethylene imine) (PEI-800), at different amine loadings. Suitable loading of amine was identified based on the balance between adsorption and kinetics of adsorption at 400 ppm CO_2 concentration. Another MOF candidate that was chosen is diamine functionalized Mg_2(dobpdc) system reported by the Long group in Berkeley. The N-N' dimethyl ethylene diamine (mmen) functionalized Mg_2(dobpdc) has shown the highest equilibrium capacity at 400 ppm CO_2 concentration with uncharacteristic stepped isotherm.

Secondly, as a proof of the concept, the potential of using an amine-functionalized MOF, mmen-M_2(dobpdc) (M = Mg, Mn), supported on a structured monolith contactor for CO_2 capture from simulated flue gas was explored. The stability of the amine-functionalized mmen-Mg_2(dobpdc) and mmen-Mn_2(dobpdc) powders under humid conditions was also studied. Based on its superior stability to humidity, mmen-Mg_2(dobpdc) was selected for further growth on a honeycomb cordierite monolith that is washcoated with α-alumina. A simple approach for the synthesis of the Mg_2(dobpdc) MOF film using MgO nanoparticles as the metal precursor was employed. Rapid drying of MgO on the monolith surface followed by hydrothermal treatment was demonstrated to allow for the synthesis of a MOF film with good crystallite density and favorable orientation of the MOF crystals leading to high CO_2

adsorption capacities. This is one of the first examples of the deployment of an advanced MOF adsorbent in a scalable, low pressure drop gas-solid contactor. The versatility of the approach was also shown where the method was extended to grow Mg-MOF-74 on a honeycomb monolith using a modified recipe. Presence of water was found to expedite the conversion of MgO to MOF. In case of Mg-MOF-74, it was found that presence of water was also essential to obtain a phase-pure MOF. The optimized approach was applied to grow Mg-MOF-74 on the honeycomb monolith.

N,N'-dimethyl ethylene diamine (MMEN) and ethylene diamine (ED) functionalized Mg_2(dobpdc) have shown some of the highest capacities for CO_2 capture under simulated direct air capture (DAC) conditions i.e. at a CO_2 partial pressure at 0.4 mbar. However, nearly all analyses of such systems have focused on equilibrium adsorption assessments. In the closing chapter, the adsorption of CO_2 under ultra-dilute conditions relevant to DAC was studied using a packed bed breakthrough system. The effects of flowrate, temperature and CO_2 concentration on the breakthrough profiles were elucidated. Using the equilibrium wave theory, different breakthrough profile zones were identified. Furthermore, deviations of the observed experimental data from the simulated breakthrough profiles were systematically identified, and linked to mass transfer resistances in the bed. A packed-bed model that accounts for the cooperative reaction mechanism for adsorption of CO_2 in mmen-Mg_2(dobpdc) was subsequently developed in collaboration with the systems group. The avrami model with a fractional order with respect to time was found to have a best fit to the TGA uptake despite a limited physical justification. Overall, this thesis addressed many aspects that can make or break the deployment of novel adsorbents for practical applications.

1 CO_2 CAPTURE USING AMINE-FUNCTIONALIZED METAL ORGANIC FRAMEWORKS (MOFs): INTRODUCTION & ASSESSMENT OF CRITICAL RESEARCH NEEDS

Parts of this chapter are reproduced from Darunte, L. A.; Walton, K. S.; Sholl, D. S.; Jones, C. W., CO_2 Capture Via Adsorption in Amine-Functionalized Sorbents. Current Opinion in Chemical Engineering 2016, 12, pp 82-90 with permission from Elsevier.

1.1 Introduction

The concentration of CO_2 in air has increased from ~270 ppm before the industrial revolution to close to 405 ppm today.[1] The Intergovernmental Panel on Climate Change (IPCC) has forecast an increase in global temperature of 1.8° C by 2100, largely as a result of anthropogenic CO_2 emissions.[2] About half of these CO_2 emissions are from distributed sources such as transportation, with the remainder coming from concentrated sources such as fossil fuel-based power plants.[3] Research on carbon capture has primarily focused on capturing CO_2 from large point sources. Consideration has also been given to capturing CO_2 directly from ambient air (direct air capture (DAC)).[4] All CO_2 capture technologies come with an economic penalty, and as a result, lower-cost capture methods are continuously sought. Aqueous amine based technologies, which are the benchmark capture technologies, suffer from a high-energy penalty[5,6] because of the energy required to heat water during the CO_2 recovery step, which typically forms 70% of the amine solution.

Supported amine materials are an attractive class of solid adsorbents that have potential advantages relative to liquid amines.[7,8] Porous solids have intrinsically lower heat capacities than water, so they can have lower parasitic energy demands than liquid absorbents. Supported amine materials are most often employed in temperature swing adsorption (TSA) processes or similar cyclic processes, where adsorption is conducted at low temperature and desorption is induced by heating the adsorbent. In this chapter, I review recent advances with supported amine adsorbents for CO_2 capture. Supported amine materials are particularly effective for CO_2 capture at low CO_2 partial pressures, so this review will focus on materials for CO_2 capture from streams such as flue gas and ambient air. The chapter places an emphasis on current trends in development of these materials for practical CO_2 capture, focusing on (i) CO_2 adsorption mechanisms, (ii) novel materials (MOFs), (iii) the effect of humidity on CO_2 capture, and (iv) regeneration and practical implementation of amine sorbent materials.

Much of the work on supported amines has used ordered mesoporous oxide supports as illustrated in Figure 1.1. because of their excellent stability. Alumina and metal organic frameworks (MOFs) are among the other support materials that are gaining attention for use in supporting amines.[8,9] These materials have been classified into three groups based on the nature of the interaction with the support and the preparation method.[7,10] In class 1 materials, polymeric amines such as poly (ethylene imine) (PEI), are impregnated into the support's pores and have relatively weak, non-covalent interactions with the support surface. In class 2 materials, molecular amines such as aminopropyl silane (APS) are bound to the support surface through covalent bonds. In class 3 materials, *in-*

situ polymerization of an amine-containing monomer is used to create polyamines with both covalent and non-covalent interactions with the surface (for example: hyperbranched aminosilicas (HAS)).

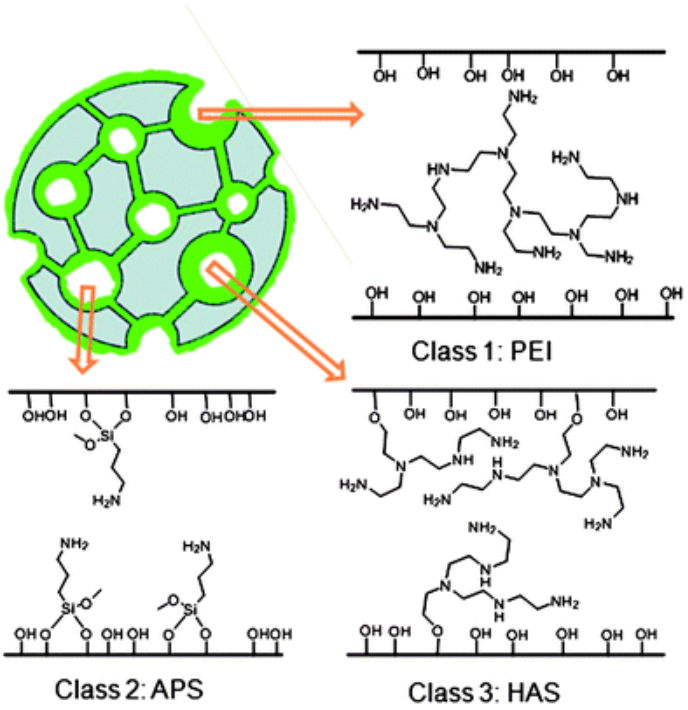

Figure 1.1. Classification of supported amine materials, illustrated for a silica support.[7] The schematic shows supported amines (green) in the pores of a support. Reproduced with permission from the Royal Society of Chemistry.

1.2 Mechanism of CO_2 capture in supported amine materials

The most common mechanism for CO_2 capture in supported amines (Figure 1.2) involves the formation of a zwitterion through the interaction of CO_2 and an amine, followed by deprotonation of the zwitterion by a base to produce a carbamate.[11–14] The amine efficiency, defined as the ratio of moles of CO_2 captured to moles of nitrogen in the material, is a useful metric to quantify the effectiveness of adsorbents for CO_2 capture. In the zwitterionic mechanism, a second amine typically acts as the base to produce an

ammonium carbamate, giving a theoretical maximum amine efficiency of 0.5. This suggests achieving a high density of amines in close proximity to each other can improve the amine efficiency. Under humid conditions, water or hydroxide ions can potentially act as the base, leading to theoretical amine efficiencies that approach 1. There is now experimental evidence[12] that a second mechanism producing ammonium bicarbonate can occur under humid conditions, also with a theoretical amine efficiency of 1. At low CO_2 partial pressures, amine efficiencies lower than these theoretical maxima are typically expected, depending on the equilibrium between the gaseous CO_2 and the bound states (shape of the adsorption isotherm) as well as kinetic limitations.

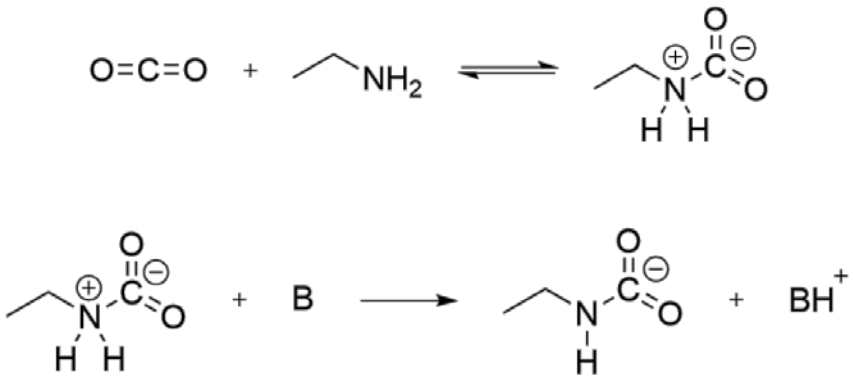

Figure 1.2. A zwitterion is formed by interaction of CO_2 with an amine, which is further deprotonated in the presence of another base to produce an alkyl carbamate.[7] Reproduced with permission from the Royal Society of Chemistry

1.3 Metal organic frameworks as supports for amine sorbents

Metal organic frameworks (MOFs) are hybrid materials consisting of metal ions or metal clusters bound together through organic linkers to create a multi-dimensional porous crystalline structure. Their high porosity and chemical diversity make MOFs highly

attractive candidates for gas adsorption.[15] MIL-101, MIL-100 and UiO-66 are some of the MOFs that have shown excellent stability under extreme conditions of temperature, humidity and pH.[16] Although stability is a concern for some materials, MOFs have potential as materials for CO_2 capture,[17] by showing high capacities associated with high surface areas[18,19] or via novel adsorption mechanisms.[20]

1.3.1 MOFs with amine functionalized ligands

Use of amine-functionalized ligands in the synthesis of MOFs is one approach to decorate MOF pores with amines. For example, An et al.[21] reported that Bio-MOF-11 with pores decorated with amine and adeninate groups could adsorb 1.30 mmol/g of CO_2 at 298 K and 0.15 bar CO_2 with a heat of adsorption of ~45 kJ/mol. Couck et al.[22] reported amine-functionalized MIL-53(Al) had significantly higher CO_2 adsorption capacities than the parent, amine-free MIL-53(Al). The material also demonstrated secondary gas uptake because of contraction of the framework, but at different pressures than conventional MIL-53(Al).

Use of amine linkers coupled with another pillaring ligand has been shown to enhance both CO_2 adsorption as well as CO_2 selectivity over nitrogen. Vaidyanathan et al.[23] used 3-amino-1,2,4-triazole ligands along with oxalic acid as pillaring linkers to create a narrow pore 3-D framework that adsorbed ~ 3 mmol/g CO_2 at 0.15 bar CO_2 and 273 K, but showed negligible N_2 adsorption because of its narrow pore-induced diffusion resistance. In other work, Halder et al.[24] reported two double catenated Cd-based frameworks with 2-amino,

1-4 benzenedicarboxylic acid (NH_2-BDC) and 1,2-bis-(4-pyridyl-methylene) hydrazine ligands. This framework adsorbed ~ 1.2 mmol/g CO_2 at 0.15 bar CO_2 and 273 K.

MOFs constructed with amine functionalized ligands are generally less effective for CO_2 capture compared to post synthetically modified MOFs containing amines because of delocalization of the electron pair on the aromatic amine ligand. This is manifested by relatively lower heats of adsorption (~30-40 kJ/mol)[21,22,24] for CO_2 capture over these materials compared to heats of adsorption (~60–90 kJ/mol) for post synthetically modified MOFs with amine alkyl groups.

1.3.2 MOFs with post synthetic amine functionalization

Post synthetic modification of MOF frameworks with alkylamines is another approach to improve CO_2 capture in MOFs at low partial pressures of CO_2. Some as synthesized MOFs such as MIL-101 (Cr) and Mg_2(dobpdc) have solvents attached to metal centers that can be removed under vacuum and/or high temperature to create unsaturated metal sites. These open metal sites can then be functionalized with diamine molecules, one amine bound to an open metal site and the other end exposed in the pore to capture CO_2. Conventional CO_2 capture with amines proceeds through the formation of ammonium carbamate, and it is important to have amines located close to each other. Open metal sites can be postsynthetically modified with small amines such as ethylene diamine (ED), dimethyl ethylene diamine (DMEN), and larger polyamines such as PEI. The MIL-101(Cr) framework has been reported to have a high BET surface area (~ 2600-4500 m^2/g) and outstanding water stability.[25] The framework offers open metal sites that are generated by

heating the framework under high vacuum at 423 K. Hwang et al.[26] first reported the post synthetic modification of MIL-101(Cr) with ED. Later, Jiang et al.[27] functionalized MIL-101(Cr) with ED (Figure 1.3), diethylene triamine (DETA), and diaminodipropylamine (DADPA) and studied CO_2 adsorption over the amine functionalized MIL-101(Cr). They observed that DETA showed the highest CO_2 capacity (2 mmol/g) at 0.15 bar CO_2 and 298 K. Chen et al.[28] studied MIL-101(Cr) loaded with PEI using PEI-300, PEI-1800 and PEI-10000 and found that PEI-300, at higher loadings, demonstrated the highest CO_2 capacity (4.2 mmol/g) 0.15 bar CO_2 and 298 K.

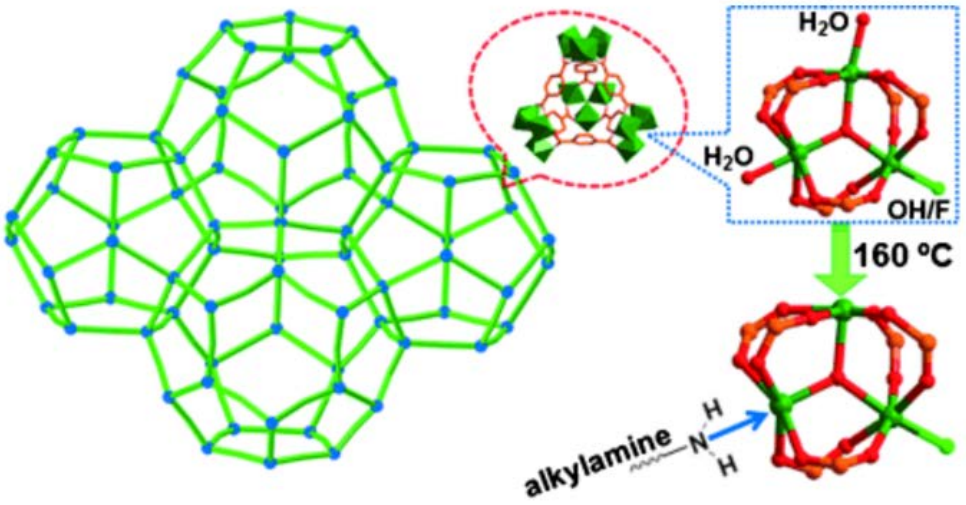

Figure 1.3. Functionalization of open metal sites in MIL-101(Cr) with an alkyl amine.[27] Reproduced from ref. 27 with permission from John Wiley and Sons

UiO-66 is another water stable MOF framework with weakly acidic zirconium open metal sites after the evacuation of guest molecules at high temperature. Zhang et al.[29]

grafted deprotonated monoethanol amine (MEA) onto the UiO-66 framework and obtained CO_2 capacities of 0.8 mmol/g at 0.15 bar CO_2 and 298 K.

Mg_2(dobdc) has been demonstrated to have the highest CO_2 capacity (6.1 mmol/g) at 298 K and 0.15 bar CO_2 among MOFs because of its strongly acidic open metal sites that effectively bind CO_2.[30] The presence of open metal sites also makes the MOF susceptible to degradation in the presence of moisture.[31] Kizzie et al.[31] reported that Mg-MOF-74 lost close to 80% of its CO_2 adsorption capacity upon exposure to 70% relative humidity. However, functionalization of the open metal sites by primary amines can enhance the water stability of MOFs and simultaneously allow for superior CO_2 capacities. Choi et al.[32] reported functionalization of Mg_2(dobdc) with ED and noted CO_2 capacities of 1.5 mmol/g at a CO_2 concentration of 400 ppm. Andirov et al.[33] exposed ED functionalized Mg_2(dobdc) and the parent Mg_2(dobdc) to an accelerated steam testing. ED-Mg_2(dobdc) showed a negligible loss in porosity and CO_2 capacity with some loss in the BET surface area. However, there are no studies to date that analyze CO_2 capture of ED-Mg-DOBDC after steam exposure over many cyclic adsorption-desorption cycles.

Recently Mcdonald et al.[34] expanded the terepthalic acid ligand to create M- 4,4'-dioxido-3,3'-biphenyldicarboxylate (M_2(dobpdc), M= Mg, Mn, Ni, Fe, Co and Zn) MOF materials (Figure 1.4). This MOF has one dimensional hexagonal pores like M_2(dobdc) that are 1.8 nm wide. Functionalization of the open metal sites with diamines such as N, N'-dimethyl ethylene diamine (MMEN) has equipped the framework with a unique performance for the CO_2 capture. The CO_2 adsorption isotherms show a step change as a function of the CO_2 partial pressure.[34] Mmen-Mg_2(dobpdc) adsorbed ~ 3 mmol/g CO_2 at

air capture conditions (400 ppm) which is the highest among the current MOFs available for air capture conditions. The material also has very high amine efficiencies at low partial pressures of CO_2, which is uncommon in traditional adsorbents. The step change pressure in the CO_2 adsorption isotherm changes as a function of temperature and metal.[20] This has created an opportunity to achieve temperature swing adsorption with a relatively small temperature change.[20,34] Diamines such as ED, MMEN and DMEN have been used for functionalization of Mg_2(dobpdc), resulting in subtle changes in the capacities and step initiation pressures of the MOFs.[34,35] The step initiation pressure is also a function of the metal, with the order Co>Zn>Fe>Mn>Mg.[20] Mmen-Ni_2(dobpdc) does not demonstrate a step change in CO_2 adsorption because of the strong bonding energy between the Ni and the amine, which prevents CO_2 insertion into the metal-amine bonds.

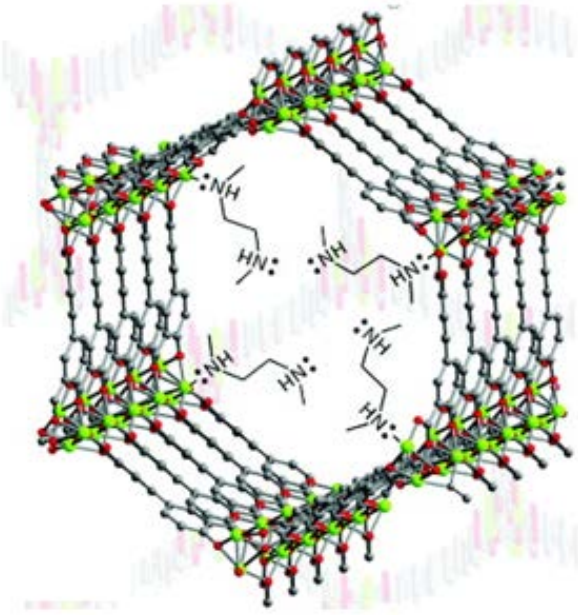

Figure 1.4. Functionalization of open metal sites of Mg_2(dobpdc) with diamines created a unique performance for CO_2 capture. Reprinted from ref. 34 with permission from the American Chemical Society

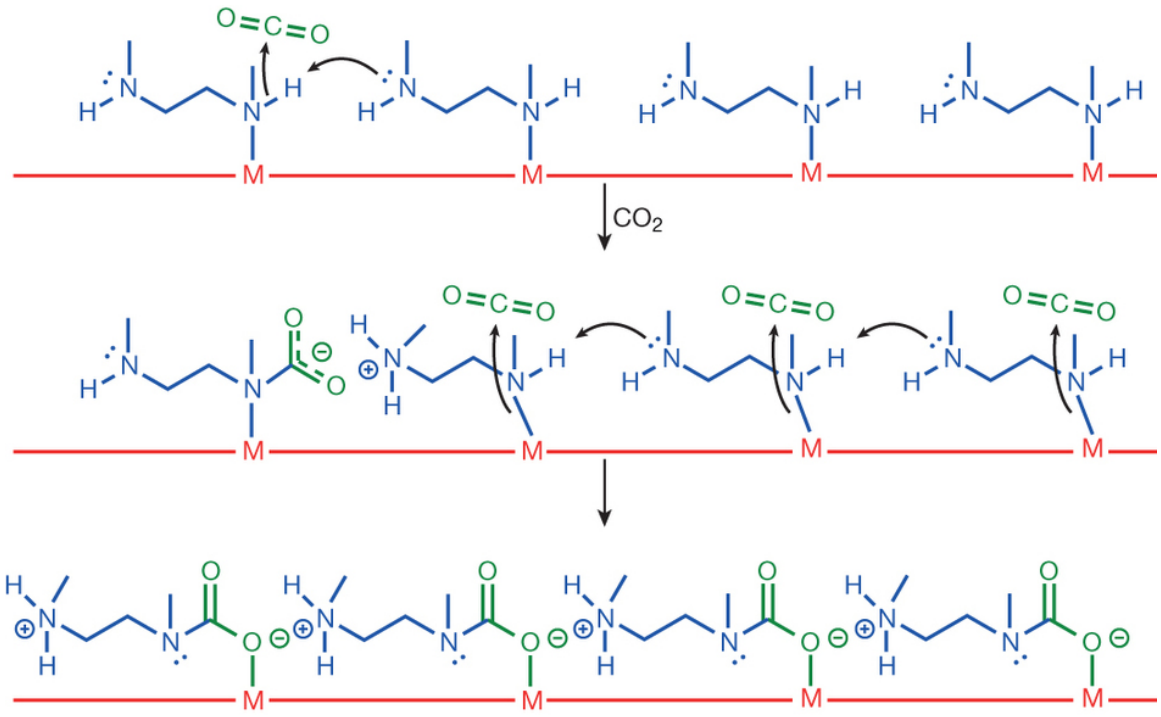

Figure 1.5 Mechanism of CO_2 capture in mmen-Mg_2(dobpdc).[20] Reprinted from ref 20 with permission from the Nature Publishing Group

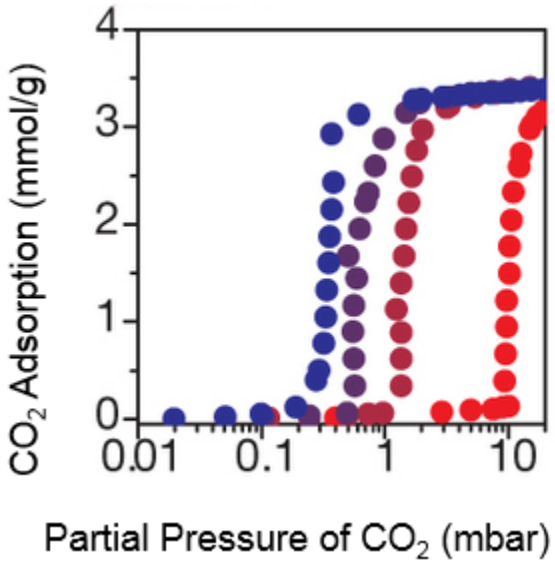

Figure 1.6 CO_2 adsorption as a function of temperature in Mg_2(dobpdc). Reprinted from ref. 20 with permission from the Nature Publishing Group

McDonald et al.[20] proposed a novel CO_2 adsorption mechanism whereby ammonium carbamate formation occurs via reversible insertion into the metal-amine bond, with the propagation of the effect along the pore length (Figure 1.5). This mechanism has been reported to result in the unique CO_2 adsorption isotherm shape (Figure 1.6) observed for these materials. CO_2 adsorption isotherm indicates phase change behavior, which is a function of temperature and metal in the framework. Use of in-situ-FTIR, structural models, and refinement against PXRD and NEXAFS[36] data all support the formation of the insertion structure along with an increase in the metal-nitrogen spacing. Calorimetric[37] and density functional theory (DFT) studies[38] further support the novel mechanism from an energetics perspective.

1.4 CO_2 capture under humid conditions

Humidity has been reported to have a significant impact on CO_2 capture with solid adsorbents. Humidity can influence CO_2 adsorption through both kinetic and thermodynamic factors and precise identification of the controlling factor is often difficult. Water has been shown to both enhance and hurt CO_2 adsorption, depending on the adsorbent and conditions used. Among kinetic factors, in conventional oxide-supported amine adsorbents water can alter the accessibility of amines by improving or impeding CO_2 transport through amine layers.[14] Goeppert et al.[39] investigated the effect of humidity on CO_2 capture from air for PEI-impregnated fumed silica. They observed that CO_2 capture under humid conditions is enhanced at lower PEI loadings and decreased at higher PEI loadings, effects attributed to a water-induced change in the accessibility of amines. In

other studies, Mebane et al.[14] hypothesized that humidity improves the accessibility of amines for CO_2 interaction.

Water can act as a base to create more alkyl carbamates or alkyl ammonium bicarbonate.[12,40,41] Ammonium bicarbonates are formed at a slower rate compared to more commonly observed alkyl ammonium carbonates. This makes it difficult to detect bicarbonate species through spectroscopic techniques using short adsorption and desorption times.[12,14] As discussed in section 1.2, bicarbonate formation can significantly improve amine efficiency as one amine can theoretically capture one CO_2 molecule. Serna-Guerrero et al. studied the effect of different relative humidities on pore expanded MCM-41 functionalized with 3-aminopropylsilyl groups (APS-MCM-41) and observed that capillary condensation of water improved CO_2 adsorption using 5% CO_2 in N_2.[40] They observed further amine efficiency improvement when the samples were prehydrated before CO_2 adsorption, suggesting the possibility of bicarbonate formation. Didas et al.[12] studied the effect of water on the amine efficiency for direct air capture conditions for different surface coverages of primary amines for APS-SBA-15 materials and observed that the maximum efficiency improvement was observed for low loadings of amines, representing sub-monolayer amine coverage. They probed the nature of the adsorbed species through *in-situ* FTIR spectroscopy and elucidated the formation of ammonium bicarbonate at longer times for low APS loading materials. Formation of ammonium bicarbonate was not observed for high APS loading materials for the time duration of the experiments. This was the first demonstration of formation of bicarbonate in humid studies for supported amine materials.

In MOFs, Mason et al.[42] analyzed the mmen-Mg_2(dobpdc) system for CO_2 adsorption in the presence of water, CO_2, and N_2 and noted slightly increased CO_2 capture in the presence of water. The metal-amine carbamate insertion was still observed in the presence of water, which was confirmed through *in-situ* FTIR spectra. Mmen-Ni_2(dobpdc), which does not show carbamate insertion in the presence of CO_2, showed a considerable increase in the CO_2 capture in the presence of moisture, possibly due to bicarbonate formation or the formation of more alkyl ammonium carbamate species.

Many MOFs[31,43] have reported a loss in crystallinity and BET surface area after exposure to humid conditions. Functionalization with amines is expected to improve the stability under humid conditions for MOFs with open metal sites. For amine sorbents, urea formation under dry conditions reduces sorbent capacity but its formation under humid conditions is not observed[44] thus enhancing water stability of the adsorbent.

1.5 Regeneration and Process Development

Higher heats of adsorption in supported amine adsorbents compared to conventional physisorbents create favorable thermodynamics for higher capacity at very low partial pressures of CO_2, such as those found in ambient air. Higher heats of adsorption also lead to the higher energy required to desorb CO_2 during adsorbent regeneration. Recovery can be achieved through pressure swing adsorption (PSA) or temperature swing adsorption (TSA). In pressure swing adsorption (PSA), the pressure change of the large volumes of gas associated with dilute gas streams may make PSA too energy intensive for cost-effective carbon capture and sequestration. Also, the complete desorption of CO_2 is

typically not achieved at room temperature with amine materials[45] because of chemisorbed nature of the CO_2, thereby necessitating an increase in the temperature.

Use of inert sweep gases for TSA is common in laboratory studies but is cost prohibitive in an industrial setting, as the output is a diluted CO_2 gas stream. To this end, two more practical approaches have been studied to achieve temperature swing (i) use of a pure CO_2 purge stream at elevated temperature to obtain a concentrated stream of CO_2, and (ii) use of steam for CO_2 desorption. [10] Degradation of amines through formation of urea linkages has been observed at high temperature in presence of pure CO_2.[46,47] Sayari et al.[48,49] systematically studied the stability of different amine types and observed that primary amines deactivate by forming ureas with relative ease compared to the secondary amines and proposed isocyanate intermediate and ammonium carbamate pathways for the deactivation of amine.[48] Their studies also reported that urea-induced deactivation was not observed in humid CO_2. DFT calculations by Didas et al.[50] supported the isocyanate pathway as energetically favorable. Also, as noted previously, M_2(dobpdc) (M = Mg, Mn, Zn, Co and Fe) are promising materials because regeneration is possible with a small change in the temperature compared to traditional amine materials. This presents an opportunity to use CO_2 for desorption at much lower temperatures, with the possibility of urea induced amine deactivation significantly lower.

With steam stripping, steam provides the impetus for CO_2 desorption via both a concentration and temperature driving force and a highly enriched stream of CO_2 can be achieved at the outlet after condensation of steam. Steam stripping has also been reported to provide faster desorption kinetics.[10,51] However, the effect of the steam on the stability

of the adsorbent materials is a critical factor, as water soluble PEI can in some cases leach out or reorganization of the amine materials on the support may occur.[51] Chaikittisilp et al.[52] reported that mesoporous γ-alumina supported PEI materials are more stable than mesoporous SBA-15 supported PEI materials under 24- hour accelerated steam testing and retained more than 80% of the initial CO_2 adsorption for 0.1 bar CO_2 in N_2. In further studies, Sakwa-Novak et al.[53] reported PEI leaching as the primary reason for loss in capacity for 24-hour accelerated steam testing but observed little PEI leaching up to 12 h or in extended short duration cycles. Also, it was shown that structural changes in γ-alumina through bohemite formation during the steam exposure did not have a significant impact on CO_2 adsorption for air capture conditions.

For process design, a variety of gas-solid contacting configurations have been studied. These include conventional fixed beds, which are commonly employed for lab scale studies, but are not viable for practical CO_2 capture at large scales. Among the recently studied novel contactor configurations employed for amine adsorbents, hollow fibers for flue gas capture have been described by Lively et al.[54,55] , monoliths for air capture by Eisenberger[56] and fluidized beds by Zhang et al.[57] Kulkarni et al.[58] analyzed a hypothetical monolith based supported amine CO_2 capture technology and determined that parasitic heat costs associated with the heat capacity of the monoliths were a key cost factor and they suggested the use of thin-walled monoliths. They also suggested that having a high equilibrium CO_2 capacity adsorbent was needed to achieve minimal energetic costs per unit CO_2 captured. In the future, an increased emphasis on co-developing sorbents and

contactors is needed, as the development of adsorbents that cannot be suitably deployed in a practical contactor will not lead to new, effective CO_2 separation technologies.

1.6 Direct Air Capture & Identification of Critical Research Needs

This chapter reviewed recent advances in amine-functionalized oxide and MOF materials for CO_2 separation from dilute gas mixtures such as flue gas and ambient air. CO_2 capture directly from air or direct air capture (DAC) is gaining attention as one of the few carbon negative technologies. The ultra-dilute concentration of CO_2 in air can present challenges to develop a practical economic process. Realff and Lively[59] analyzed a temperature swing adsorption (TSA) for a series of adsorbents with the different affinity between CO_2 and adsorbents and observed that the minimum thermodynamic energy of unmixing does not scale up linearly with the concentration. The minimum thermodynamic energy of unmixing for DAC is only ~2 times more than that of flue gas despite the dilution ratio of 375. They identified that optimal 2nd law efficiency of a TSA process is achieved when the heat of adsorption is ~ 65 kJ/mole for ultra-dilute conditions corresponding to DAC. They also suggested that most of the thermodynamic work in a TSA process happens during the desorption of CO_2, which is almost identical to both DAC and flue gas capture. System design is expected to play an important role to achieve deployment and for that, following aspects of DAC must be investigated.

1. Development of high capacity and humidity stable materials.

2. Water adsorption as a function of humidity. Some adsorbents such as silica, MOF tend to adsorb a high stoichiometric amount of water and resultant

adsorption and desorption of water during a process can result into high-energy penalty.

3. Scale-up of the system by the development of MOFs on a structured contactor with an effective performance compared to powders.

4. Structured contactor design to achieve a high loading of the adsorbent.

5. Understanding of adsorption and desorption kinetics of the combined system of MOF on a structured contactor.

The contribution in this thesis directly addresses many questions related to aspects one, two, three & four above. Porous oxide supported PEI materials are among the current state-of-the-art materials for CO_2 capture, with new MOF supported amine materials based on , M_2(dobpdc) (M = Mg, Mn, Zn, Co and Fe) showing the potential for substantial improvements in the CO_2 adsorption capacity as well as CO_2 separation energetics. Chapter 2 investigates amine-functionalized MIL-101(Cr) adsorbents for CO_2 adsorption at 400 ppm concentration. Chapter 3 investigates CO_2 adsorption, humid stability, and development of Mg_2(dobpdc) framework on a monolithic support and presents a generalized approach for the development of MOF films from oxide MOF precursors. Chapter 4 presents an investigation of kinetics for mmen-Mg_2(dobpdc) system using breakthrough curve analysis and application of wave theory. Stepped-isotherms demonstrated by this system are not common and analysis in this thesis identifies different zones of operation based on the concentration of CO_2 in the feed. The kinetics of CO_2 adsorption is studied using an Avrami model and it was found to have a good fit for the

TGA updatake. Chapter 5 outlines current challenges and path forward. Overall, this thesis has led to an improved understanding of novel materials for a practical CO_2 capture.

1.7 References

1. Trends in Atmospheric Carbon Dioxide. National Oceanic & Atmospheric Administration **2015**.

2. Kirtman, B.; Power, S. B.; Adedoyin, J. A.; Boer, G. J.; Bojariu, R.; Camilloni, I.; Doblas-Reyes, F. J.; Fiore, A. M.; Kimoto, M.; Meehl, G. A.; et al. Chapter 11: Near-Term Climate Change: Projections and Predictability. C*lim. Chang. 2013 Phys. Sci. Basis. Contrib. Work. Gr. I to Fifth Assess. Rep. Intergov. Panel Clim. Chang.* **2013**, No. June, 953–1028.

3. EPA. Inventory of U.S. Greenhouse Gas Emissions and Sinks: 1990–2011. US Environ. Prot. Agency **2013**, ES1-ES26.

4. Lackner, K. S.; Brennan, S.; Matter, J. M.; Park, A. H.; Wright, A.; van der Zwaan, B. The Urgency of the Development of CO_2 Capture from Ambient Air. *Proc Natl Acad Sci U S A* **2012**, 109 (33), 13156–13162.

5. Ahn, H.; Luberti, M.; Liu, Z.; Brandani, S. Process Configuration Studies of the Amine Capture Process for Coal-Fired Power Plants. Int. *J. Greenh. Gas Control **2013***, 16, 29–40.

6. Goto, K.; Yogo, K.; Higashii, T. A Review of Efficiency Penalty in a Coal-Fired Power Plant with Post-Combustion CO_2 Capture. *Appl. Energy* **2013**, 111, 710–720.

7. Bollini, P.; Didas, S. A.; Jones, C. W. Amine-Oxide Hybrid Materials for Acid Gas Separations. *J. Mater. Chem*. **2011**, 21 (39), 15100–15120.

8. D'Alessandro, D. M.; Smit, B.; Long, J. R. Carbon Dioxide Capture: Prospects for New Materials. *Angew. Chemie Int. Ed*. **2010**, 49 (35), 6058–6082.

9. Lu, C.; Bai, H.; Wu, B.; Su, F.; Hwang, J. F. Comparative Study of CO_2 Capture by Carbon Nanotubes, Activated Carbons, and Zeolites. J. Name *Energy Fuels*; J. Vol. 22; J. Issue 5; **2008**, pp 3050-3056.

10. Li, W.; Choi, S.; Drese, J. H.; Hornbostel, M.; Krishnan, G.; Eisenberger, P. M.; Jones, C. W. Steam-Stripping for Regeneration of Supported Amine-Based CO_2 Adsorbents. *ChemSusChem* **2010**, 3 (8), 899–903.

11. Pinto, M. L.; Mafra, L.; Guil, J. M.; Pires, J.; Rocha, J. Adsorption and Activation of CO_2 by Amine-Modified Nanoporous Materials Studied by Solid-State NMR and $13CO_2$ Adsorption. *Chem. Mater.* **2011**, 23 (6), 1387–1395.

12. Didas, S. A.; Sakwa-Novak, M. A.; Foo, G. S.; Sievers, C.; Jones, C. W. Effect of Amine Surface Coverage on the Co-Adsorption of CO_2 and Water: Spectral Deconvolution of Adsorbed Species. *J. Phys. Chem. Lett*. **2014**, 5 (23), 4194–4200.

13. Donaldson, T. L.; Nguyen, Y. N. Carbon Dioxide Reaction Kinetics and Transport in Aqueous Amine Membranes. *Ind. Eng. Chem. Fundam*. **1980**, 19 (3), 260–266.

14. Mebane, D. S.; Kress, J. D.; Storlie, C. B.; Fauth, D. J.; Gray, M. L.; Li, K. Transport, Zwitterions, and the Role of Water for CO_2 Adsorption in Mesoporous Silica-Supported Amine Sorbents. J. Phys. Chem. C **2013,** 117 (50), 26617–26627.

15. Chung, Y. G.; Camp, J.; Haranczyk, M.; Sikora, B. J.; Bury, W.; Krungleviciute, V.; Yildirim, T.; Farha, O. K.; Sholl, D. S.; Snurr, R. Q. Computation-Ready, Experimental Metal–Organic Frameworks: A Tool To Enable High-Throughput Screening of Nanoporous Crystals. Chem. Mater. **2014**, 26 (21), 6185–6192.

16. Burtch, N. C.; Jasuja, H.; Walton, K. S. Water Stability and Adsorption in Metal–Organic Frameworks. Chem. Rev. **2014**, 114 (20), 10575–10612.

17. Keskin, S.; van Heest, T. M.; Sholl, D. S. Can Metal–Organic Framework Materials Play a Useful Role in Large-Scale Carbon Dioxide Separations? ChemSusChem **2010**, 3 (8), 879–891.

18. Llewellyn, P. L.; Bourrelly, S.; Serre, C.; Vimont, A.; Daturi, M.; Hamon, L.; De Weireld, G.; Chang, J.-S.; Hong, D.-Y.; Kyu Hwang, Y.; et al. High Uptakes of CO_2 and CH4 in Mesoporous Metal—Organic Frameworks MIL-100 and MIL-101. Langmuir **2008**, 24 (14), 7245–7250.

19. Farha, O. K.; Özgür Yazaydın, A.; Eryazici, I.; Malliakas, C. D.; Hauser, B. G.; Kanatzidis, M. G.; Nguyen, S. T.; Snurr, R. Q.; Hupp, J. T. De Novo Synthesis of a Metal–organic Framework Material Featuring Ultrahigh Surface Area and Gas Storage Capacities. Nat Chem **2010**, 2 (11), 944–948.

20. Mcdonald, T. M.; Mason, J. A.; Kong, X.; Bloch, E. D.; Gygi, D.; Dani, A.; Crocellà, V.; Giordanino, F.; Odoh, S. O.; Drisdell, W. S.; et al. Cooperative Insertion of CO_2 in Diamine- Appended Metal-Organic Frameworks. *Nature* **2015,** 519, 303–308

21. An, J.; Geib, S. J.; Rosi, N. L. High and Selective CO_2 Uptake in a Cobalt Adeninate Metal−Organic Framework Exhibiting Pyrimidine- and Amino-Decorated Pores. J. Am. Chem. Soc. **2010**, 132 (1), 38–39.

22. Couck, S.; Denayer, J. F. M.; Baron, G. V; Rémy, T.; Gascon, J.; Kapteijn, F. An Amine-Functionalized MIL-53 Metal−Organic Framework with Large Separation Power for CO_2 and CH4. J. Am. Chem. Soc. **2009**, 131 (18), 6326–6327.

23. Vaidhyanathan, R.; Iremonger, S. S.; Dawson, K. W.; Shimizu, G. K. An Amine-Functionalized Metal Organic Framework for Preferential CO_2 Adsorption at Low Pressures. Chem Commun **2009**, No. 35, 5230–5232.

24. Haldar, R.; Reddy, S. K.; Suresh, V. M.; Mohapatra, S.; Balasubramanian, S.; Maji, T. K. Flexible and Rigid Amine-Functionalized Microporous Frameworks Based on Different Secondary Building Units: Supramolecular Isomerism, Selective CO_2 Capture, and Catalysis. Chemistry (Easton). **2014**, 20 (15), 4347–4356.

25. Hong, D.-Y.; Hwang, Y. K.; Serre, C.; Férey, G.; Chang, J.-S. Porous Chromium Terephthalate MIL-101 with Coordinatively Unsaturated Sites: Surface

Functionalization, Encapsulation, Sorption and Catalysis. *Adv. Funct. Mater.* **2009**, 19 (10), 1537–1552.

26. Hwang, Y. K.; Hong, D.-Y.; Chang, J.-S.; Jhung, S. H.; Seo, Y.-K.; Kim, J.; Vimont, A.; Daturi, M.; Serre, C.; Férey, G. Amine Grafting on Coordinatively Unsaturated Metal Centers of MOFs: Consequences for Catalysis and Metal Encapsulation. *Angew. Chemie* **2008**, 120 (22), 4212–4216.

27. Hu, Y.; Verdegaal, W. M.; Yu, S.-H.; Jiang, H.-L. Alkylamine-Tethered Stable Metal-Organic Framework for CO_2 Capture from Flue Gas. *ChemSusChem* **2014**, 7 (3), 734–737.

28. Lin, Y.; Lin, H.; Wang, H.; Suo, Y.; Li, B.; Kong, C.; Chen, L. Enhanced Selective CO_2 adsorption on polyamine/MIL-101(Cr) Composites. *J. Mater. Chem. A* **2014**, 2 (35), 14658.

29. Li, L.-J.; Liao, P.-Q.; He, C.-T.; Wei, Y.-S.; Zhou, H.-L.; Lin, J.-M.; Li, X.-Y.; Zhang, J.-P. Grafting Alkylamine in UiO-66 by Charge-Assisted Coordination Bonds for Carbon Dioxide Capture from High-Humidity Flue Gas. J. *Mater. Chem. A* **2015**.

30. Britt, D.; Furukawa, H.; Wang, B.; Glover, T. G.; Yaghi, O. M. Highly Efficient Separation of Carbon Dioxide by a Metal-Organic Framework Replete with Open Metal Sites. *Proc. Natl. Acad. Sci. U. S. A.* **2009**, 106 (49), 20637–20640.

31. Kizzie, A. C.; Wong-Foy, A. G.; Matzger, A. J. Effect of Humidity on the Performance of Microporous Coordination Polymers as Adsorbents for CO_2 Capture. *Langmuir* **2011**, 27 (10), 6368–6373.

32. Choi, S.; Watanabe, T.; Bae, T.-H.; Sholl, D. S.; Jones, C. W. Modification of the Mg/DOBDC MOF with Amines to Enhance CO_2 Adsorption from Ultradilute Gases. *J. Phys. Chem. Lett.* **2012**, 3 (9), 1136–1141.

33. Andirova, D.; Lei, Y.; Zhao, X.; Choi, S. Functionalization of Metal-Organic Frameworks for Enhanced Stability under Humid Carbon Dioxide Capture Conditions. *ChemSusChem* **2015**, 8 (20), 3405–3409.

34. McDonald, T. M.; Lee, W. R.; Mason, J. A.; Wiers, B. M.; Hong, C. S.; Long, J. R. Capture of Carbon Dioxide from Air and Flue Gas in the Alkylamine-Appended Metal–Organic Framework Mmen-Mg2(dobpdc). *J. Am. Chem. Soc.* **2012**, 134 (16), 7056–7065.

35. Lee, W. R.; Hwang, S. Y.; Ryu, D. W.; Lim, K. S.; Han, S. S.; Moon, D.; Choi, J.; Hong, C. S. Diamine-Functionalized Metal–organic Framework: Exceptionally High CO_2 Capacities from Ambient Air and Flue Gas, Ultrafast CO_2 Uptake Rate, and Adsorption Mechanism. *Energy Environ. Sci.* **2014**.

36. Drisdell, W. S.; Poloni, R.; McDonald, T. M.; Pascal, T. A.; Wan, L. F.; Pemmaraju, C. Das; Vlaisavljevich, B.; Odoh, S. O.; Neaton, J. B.; Long, J. R.; et al. Probing the Mechanism of CO_2 Capture in Diamine-Appended Metal-Organic Frameworks

Using Measured and Simulated X-Ray Spectroscopy. *Phys. Chem. Chem. Phys*. **2015**, 17 (33), 21448–21457.

37. Wu, D.; McDonald, T. M.; Quan, Z.; Ushakov, S. V; Zhang, P.; Long, J. R.; Navrotsky, A. Thermodynamic Complexity of Carbon Capture in Alkylamine-Functionalized Metal–organic Frameworks. *J. Mater. Chem. A* **2015**, 3 (8), 4248–4254.

38. Planas, N.; Dzubak, A. L.; Poloni, R.; Lin, L. C.; McManus, A.; McDonald, T. M.; Neaton, J. B.; Long, J. R.; Smit, B.; Gagliardi, L. The Mechanism of Carbon Dioxide Adsorption in an Alkylamine-Functionalized Metal-Organic Framework. *J Am Chem Soc* **2013**, 135 (20), 7402–7405.

39. Goeppert, A.; Czaun, M.; Surya Prakash, G. K.; Olah, G. A. Air as the Renewable Carbon Source of the Future: An Overview of CO_2 Capture from the Atmosphere. *Energy Environ. Sci.* **2012**, 5 (7), 7833.

40. Serna-Guerrero, R.; Da'na, E.; Sayari, A. New Insights into the Interactions of CO_2 with Amine-Functionalized Silica. *Ind. Eng. Chem. Res.* 2008, 47 (23), 9406–9412.

41. Chang, A. C. C.; Chuang, S. S. C.; Gray, M.; Soong, Y. In-Situ Infrared Study of CO_2 Adsorption on SBA-15 Grafted with γ-(Aminopropyl)triethoxysilane. *Energy & Fuels* **2003**, 17 (2), 468–473.

42. Mason, J. A.; McDonald, T. M.; Bae, T. H.; Bachman, J. E.; Sumida, K.; Dutton, J. J.; Kaye, S. S.; Long, J. R. Application of a High-Throughput Analyzer in Evaluating Solid Adsorbents for Post-Combustion Carbon Capture via Multicomponent Adsorption of CO_2, N_2, and H_2O. *J Am Chem Soc* **2015**, 137 (14), 4787–4803.

43. DeCoste, J. B.; Peterson, G. W.; Schindler, B. J.; Killops, K. L.; Browe, M. A.; Mahle, J. J. The Effect of Water Adsorption on the Structure of the Carboxylate Containing Metal–organic Frameworks Cu-BTC, Mg-MOF-74, and UiO-66. *J. Mater. Chem. A* **2013**, 1 (38), 11922.

44. Sayari, A.; Belmabkhout, Y. Stabilization of Amine-Containing CO_2 Adsorbents: Dramatic Effect of Water Vapor. *J. Am. Chem. Soc.* **2010**, 132 (18), 6312–6314.

45. Jones, C. W. CO_2 Capture from Dilute Gases as a Component of Modern Global Carbon Management. *Annu. Rev. Chem. Biomol. Eng.* **2011**, 2 (1), 31–52.

46. Drage, T. C.; Smith, K. M.; Arenillas, A.; Snape, C. E. Developing Strategies for the Regeneration of Polyethylenimine Based CO_2 Adsorbents. *Energy Procedia* **2009**, 1 (1), 875–880.

47. Drage, T. C.; Arenillas, A.; Smith, K. M.; Snape, C. E. Thermal Stability of Polyethylenimine Based Carbon Dioxide Adsorbents and Its Influence on Selection of Regeneration Strategies. *Microporous Mesoporous Mater.* **2008**, 116 (1–3), 504–512.

48. Sayari, A.; Heydari-Gorji, A.; Yang, Y. CO_2-Induced Degradation of Amine-Containing Adsorbents: Reaction Products and Pathways. *J. Am. Chem. Soc.* **2012**, 134 (33), 13834–13842.

49. Sayari, A.; Belmabkhout, Y.; Da'na, E. CO_2 Deactivation of Supported Amines: Does the Nature of Amine Matter? *Langmuir* **2012**, 28 (9), 4241–4247.

50. Didas, S. A.; Zhu, R.; Brunelli, N. A.; Sholl, D. S.; Jones, C. W. Thermal, Oxidative and CO_2 Induced Degradation of Primary Amines Used for CO_2 Capture: Effect of Alkyl Linker on Stability. *J. Phys. Chem. C* **2014**, 118 (23), 12302–12311.

51. Hammache, S.; Hoffman, J. S.; Gray, M. L.; Fauth, D. J.; Howard, B. H.; Pennline, H. W. Comprehensive Study of the Impact of Steam on Polyethyleneimine on Silica for CO_2 Capture. *Energy & Fuels* **2013**, 27 (11), 6899–6905.

52. Chaikittisilp, W.; Kim, H.-J.; Jones, C. W. Mesoporous Alumina-Supported Amines as Potential Steam-Stable Adsorbents for Capturing CO_2 from Simulated Flue Gas and Ambient Air. *Energy & Fuels* **2011**, 25 (11), 5528–5537.

53. Sakwa-Novak, M. A.; Jones, C. W. Steam Induced Structural Changes of a Poly(ethylenimine) Impregnated γ-Alumina Sorbent for CO_2 Extraction from Ambient Air. *ACS Appl. Mater. Interfaces* **2014**, 6 (12), 9245–9255.

54. Lively, R. P.; Chance, R. R.; Kelley, B. T.; Deckman, H. W.; Drese, J. H.; Jones, C. W.; Koros, W. J. Hollow Fiber Adsorbents for CO_2 Removal from Flue Gas. *Ind. Eng. Chem. Res.* **2009**, 48 (15), 7314–7324.

55. Rezaei, F.; Lively, R. P.; Labreche, Y.; Chen, G.; Fan, Y.; Koros, W. J.; Jones, C. W. Aminosilane-Grafted Polymer/Silica Hollow Fiber Adsorbents for CO_2 Capture from Flue Gas. *ACS Appl. Mater. Interfaces* **2013**, 5 (9), 3921–3931.

56. Eisenberger, P. Carbon Dioxide Capture/regeneration Aparatus. US 8696801 B2, **2014**.

57. Zhang, W.; Liu, H.; Sun, C.; Drage, T. C.; Snape, C. E. Capturing CO_2 from Ambient Air Using a Polyethyleneimine–silica Adsorbent in Fluidized Beds. *Chem. Eng. Sci.* **2014**, 116, 306–316.

58. Kulkarni, A. R.; Sholl, D. S. Analysis of Equilibrium-Based TSA Processes for Direct Capture of CO_2 from Air. *Ind. Eng. Chem. Res.* **2012**, 51 (25), 8631–8645.

59. Lively R.P.; Reallf M.J; *AIChE Journal.*, **2016**, 62(10), 3699-3705

2 DIRECT AIR CAPTURE OF CO_2 USING AMINE FUNCTIONALIZED MIL-101(Cr)

Parts of this chapter are reproduced from 'Darunte, L. A.; Oetomo, A. D.; Walton, K. S.; Sholl, D. S.; Jones, C. W., Direct Air Capture of CO_2 Using Amine-Functionalized MIL-101(Cr). ACS Sustainable Chemistry & Engineering 2016, 4 (10), pp 5761–5768' with permissions from American Chemical Society

2.1 Introduction

Anthropogenic CO_2 emissions have been identified as a primary cause of the increase in average global temperature due to greenhouse effects.[1] Almost half of the CO_2 emissions in the US are from point sources such as industrial installations and power plants.[2] Most carbon capture technologies developed to date focus on CO_2 capture from these large point sources. However, for widespread adoption, the energy use of these processes must be reduced and the cost effectiveness of the technologies must be improved. Today, the benchmark technology for post-combustion CO_2 capture is the aqueous monoethanolamine (MEA) based absorption technology, which suffers from a high-energy penalty in part due to the high heat capacity of water.[3-4]A complementary and much less studied approach to carbon capture is to capture CO_2 directly from the air, also denoted direct air capture (DAC), originally proposed by Lackner.[5] DAC has the advantage of location flexibility and the input gas stream, ambient air, is relatively clean, as the concentrations of SO_x and NO_x are low.[6-7] However, DAC has the disadvantage of having

a very dilute input stream, with air today containing about 400 ppm CO_2.[8] This necessitates the need for a high capacity adsorbent which can reversibly capture CO_2 at low net energy use.

Solid adsorbents have received considerable attention in recent years as alternatives to liquid amine solutions because of their lower heat capacities compared to aqueous amines.[9] Generally speaking, a lower energy penalty during the adsorption-desorption process is expected to create a lower cost of CO_2 capture. Amine functionalization of solid materials is one way of creating adsorbents for CO_2 capture.[10] Through the zwitterionic mechanism of CO_2 capture analogous to liquid amines,[11] the functionalization of solids with amine sites can lead to a significant increase of the heat of adsorption of CO_2 on various materials, leading to elevated adsorption capacities. Significant uptake of CO_2 is possible at very low CO_2 partial pressures in materials functionalized with amines due to the steep adsorption isotherm created by amine-functionalization. This makes such materials promising adsorbents for air capture applications.[10, 12-13]

One of the most important metrics used to analyze effectiveness of amine-based sorbents for applications in CO_2 capture is amine efficiency, defined as the moles of CO_2 adsorbed normalized by the moles of amine present in the material. The zwitterionic mechanism suggests a maximum chemisorptive amine efficiency of 0.5 for dry sorption conditions, as two amines are required to capture one CO_2 molecule.[11] Amine efficiencies observed during practical direct air capture conditions are often much lower than the theoretical maximum.[14] High amine efficiencies have been achieved by use of amine molecules or polymers that place many amines in close proximity to each other, and by

developing sorbents that allow sufficient accessibility to the various amine sites. Xu et al.[15] introduced the concept of "molecular basket" sorbents, where CO_2 was packed inside the pores of a mesoporous SBA-15 support using a polymer containing many amine groups. They observed confinement of polymer improved the effectiveness of the composite towards CO_2 capture. Poly(ethylene imine) (PEI) has been commonly used as the preferred polymer because of its high amine content, low volatility (relative to low molecular weight amines like MEA) and commercial availability.[16-19] Amine efficiencies associated with PEI have been found to be dependent on the loading of PEI in the material,[15] and the morphology of the PEI polymer in the porous support has been found to play a role as well.[20] In another approach, small molecules such as tetraethylene pentamine (TEPA),[21] diethyl tetramine (DETA)[22] and other small amines have been impregnated in supports such as mesoporous silica SBA-15 and activated carbon to enhance CO_2 capture, because of their high amine density and the improved packing of these small molecules in the pores. For a given support, it is not always straightforward to predict which amines will yield the most efficient adsorbents, and it is important to establish a structure-property relationship to identify optimum adsorbent designs.

Recently, metal organic frameworks (MOFs) have emerged as potential CO_2 sorbents as well as supports for amine-based CO_2 capture.[23-24] MOFs are hybrid materials with metal nodes connected by organic linkers to create two or three dimensional crystalline structures. There are over 20,000 metal organic frameworks reported in the open literature with a variety of combinations of metals and organic linkers.[25-26] There are a few potential advantages of MOFs compared to other commonly used substrates such as silica.

High BET surface areas and tunable pore characteristics make many MOFs attractive supports for a variety of gas separation applications. Also, a variety of open metal sites in some families of MOFs such as M_2(dobpdc)[27] (dobpdc^{4-} = 4,4′-dioxido-3,3′-biphenyldicarboxylate, M = Mg, Mn, Zn, Ni, Co,Fe) offer an opportunity for selective post synthetic functionalization to enhance the selectivity of gas adsorption. Stability under a wide range of conditions, high pore volume and high density of open metal sites are some desired features in a MOF framework for further functionalization with amines.[28] Two materials with these characteristics are MIL-101(Cr)[29] and Mg_2(dobpdc)[27], which are noted for their high density of open metal sites and high pore volume.

The MOF MIL-101(Cr) has a 3D framework, large pore volume, and high BET surface area (2600-4500 m^2/g), with open chromium metal site densities of up to 3 mmol/g MOF framework.[30] MIL-101(Cr) is stable in boiling water and over a wide range of pH conditions.[29] Liu et al.[31] observed good regenerability of MIL-101(Cr) after exposure to SO_2 and NO, further demonstrating a good stability of the framework. Both the Cr open metal sites and the open space within the porous framework can be loaded with various amine species for CO_2 capture applications. Hwang et al.[30] first reported the post-synthetic modification of MIL-101(Cr) with ethylene diamine (ED) and studied the resulting materials for catalytic applications. Subsequently, the framework was studied for CO_2 capture after functionalization with triethylenepentamine (TEPA)[32] or pentaethylenehexamine (PEHA)[33] for CO_2 capture under simulated flue gas conditions. Jiang et al.[34] ED, diethylene triamine (DETA), and diaminodipropylamine (DADPA) to the open metal sites in MIL-101 (Cr) and observed that DETA showed the best adsorption

capacity for flue gas capture conditions. Chen et al.[35-36] loaded MIL-101(Cr) using PEI-300, PEI-1800 and PEI-10000 and found that PEI-300, at higher loadings, demonstrated the highest CO_2 capacities for conditions similar to flue gas applications. They also demonstrated CO_2/N_2 selectivity ~2000 for partial pressures of (0.1 mbar) of CO_2.

MM_2(dobdc) (MM- Mg, Ni, Co, Zn, $dobdc^{4-}$ = 1,4-dioxido-2,5-benzenedicarboxylate) is another MOF with a high density of open metal sites. Choi et al.[37-38] modified Mg_2(dobdc) with ethylene diamine and demonstrated improved CO_2 capture and stability of the material under ultra-dilute conditions. In another study, diamine functionalized Mg_2(dobpdc) was demonstrated to have an exceptional performance for CO_2 capture.[27] Planas et al.,[39] McDonald et al.,[40] and Drisdell et al.[41] provided data supporting an unconventional CO_2 adsorption mechanism in this system, whereas the MIL-101(Cr) family of materials is presumed to adsorb CO_2 via conventional amine-CO_2 binding mechanisms. Although water stability of Mg_2(dobpdc) has not been systematically studied, breakdown of Mg_2(dobdc) under humid conditions has been reported.[42]

Considering the excellent stability of MIL-101(Cr), the goal of this work is to systematically study CO_2 adsorption from simulated air with a focus on understanding how the equilibrium adsorption capacity and uptake kinetics are affected by the composition of a family of MIL-101(Cr)-amine materials. High CO_2 equilibrium adsorption capacities and rapid kinetics are important to assess the possible merit of these adsorbents for future practical applications. For the present study, we have functionalized MIL-101(Cr) with both small and large polyamine molecules, as shown in Figure 2.1. Tris (2-amino ethyl) amine (TREN) is a small polyamine with a high density of primary amines. Branched

poly(ethylene imine) with a molecular weight of 800 (PEI-800) is among the most commonly used polyamines in studies of amine-functionalized mesoporous oxides such as SBA-15 and MCM-41.[9] The CO_2 uptake and corresponding amine efficiencies (mol CO_2 / mol amine) for different loadings of TREN and PEI-800 in MIL-101(Cr) are measured. The temperature dependence of CO_2 adsorption over MIL-101(Cr)-PEI-800 adsorbents has also been explored.

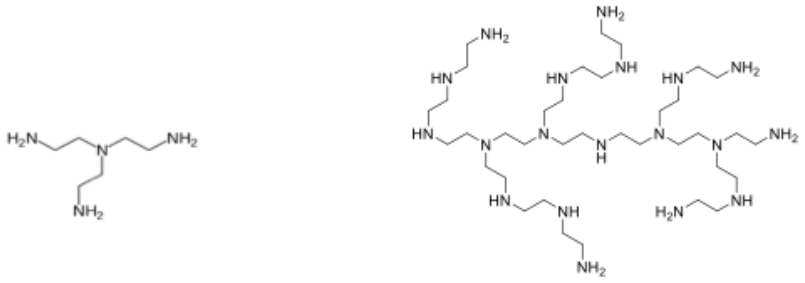

Tris (2-amino ethyl) amine (TREN) Poly (ethylene imine) (PEI)-800

Figure 2.1. Polyamines for the air capture studies

2.2 Experimental Section

2.2.1 Material synthesis

Chemicals: All the chemicals were used as purchased**.** $Cr(NO_3)_3$ (99%) and benzene dicarboxylic acid (H_2BDC) were purchased from Acros Chemicals. Dimethyl formamide (DMF), triethyl tetramine (TREN) (96%, Reagent Grade), poly(ethylene imine) (PEI) (Mw 800, Mn 600) were purchased from Sigma-Aldrich. Methanol (ACS grade) and toluene were purchased from BDH Chemicals.

MIL-101(Cr) was synthesized with a modified recipe from Hatton et al.[43] First, 800 mg of $Cr(NO_3)_3$ and 332 mg of H_2BDC were mixed in 10 mL of de-ionized (DI) water. Acetic acid was used at the modulator in the synthesis to adjust the crystal size. Different

ratios of acetic acid/ligand were used in the synthesis. Finally, based on the crystal size analysis, 1.5 mL of 36 % acetic acid was used as a modulator in the synthesis. About 5 mg of MIL-101 (Cr) crystals were used as a seed in the synthesis to obtain a uniform crystal size distribution. The solution was heated in the Teflon lined reactor at 200 °C for 12 h followed by cooling with 1 °C ramp to obtain large BDC crystals. The resultant slurry was washed repeatedly with MeOH, DMF and MeOH. The obtained powder was dried under vacuum at 150 °C.

MIL-101 (Cr)-TREN (grafted): MIL-101(Cr) was activated at 150 °C by heating under 20 mTorr vacuum for 12 h. 200 mg of activated MIL-101(Cr) and a stoichiometric amount of TREN were added to toluene and heated at 110 °C under reflux in N_2 atmosphere overnight. The solution was filtered and repeatedly washed with MeOH and then dried under 20 mTorr vacuum overnight.

MIL-101(Cr)-TREN; MIL-101(Cr)-PEI (Impregnated): MIL-101(Cr) was activated at 150 °C by heating under 20 mTorr vacuum for 12 h. A stoichiometric amount of TREN/PEI was dissolved in 10 mL MeOH and 200 mg of activated MIL-101(Cr) was added to the solution followed by stirring under N_2 atmosphere for 24 hrs. The methanol was removed by rotary evaporation and pale green MIL-101(Cr)-amine composites was later dried overnight under 20 mTorr vacuum.

2.2.2 Characterization

Nitrogen Physisorption: N_2 physisorption experiments at 77 K were performed using a Quantachrome Quadrasorb surface area analyzer. 50 mg of powder was activated at 60 °C under vacuum for 3h. The microporous surface area was estimated using BET method following criteria outlined by Walton et al.[44] in the P/P_0 range of 0.05-0.2. Pore volumes were estimated by N_2 physisorption at the partial pressure of 0.995. Surface area and pore volumes for MIL-101(Cr) and MIL-101(Cr)-amine samples were normalized to per gram of MIL-101(Cr) in the material. Amine contents were obtained from the elemental analysis for C, H and N content in the material.

Elemental Analysis: C, H, N content of the MIL-101(Cr) and amine impregnated samples were measured at Atlantic Microlabs (Norcross, GA). The N content was used to ascertain the amine loadings in the composite materials.

Powder X-ray diffraction (PXRD) measurements were made using a PANalytical X'Pert diffractometer using Cu Kα radiation.

CO_2 adsorption experiments: CO_2 adsorption experiments were performed using thermogravimetric analysis (TGA) using a TA instruments, Q 500 apparatus. In a typical experiment, 30 (+/- 3) mg of sample was pretreated with helium (flow rate: 90 mL/h) for 3 h at 110 °C followed by thermal equilibration at 25 °C. Subsequently, the sample was exposed to 400 ppm CO_2 in helium at the same temperature and flow rate for 6 h. For subsequent cycles, samples were reactivated in helium at 110 °C. A Micromeritics ASAP 2020 was used to measure CO_2 adsorption isotherms. Samples were activated at 60 °C

under vacuum for 3 h prior to analysis. Amine efficiencies were calculated by normalizing CO_2 adsorption capacities with the moles of amine determined by elemental analysis.

Scanning Electron Microscopy: A Hitachi SU 8230 cold field emission microscope was used to estimate crystal size of MIL-101(Cr). Measurements were made using an accelerating voltage of 1kV/10kV and 10 μA current. Particles were coated with gold-palladium for 5 min before the measurement.

2.3 Results & Discussion

A number of synthesis conditions were initially explored for the synthesis of MIL-101(Cr). Because the introduction of polyamines is expected to increase diffusional resistance for CO_2 uptake, a small crystal size is desired. Figure A.1 and A.2 show scanning electron microscope images of MIL-101(Cr) materials made with different ratios of acetic acid/BDC (4, 12.5 respectively). Bi-pyramidal crystals with crystal size ~150-200 nm and ~600-800 nm were obtained. Similar results have been observed with monocarboxylic acids in the case of MIL-101(Cr)[45] and Cu-BTC (BTC-benzene tricarboxylic acid),[46] where it was believed that a high concentration of acid controls the deprotonation of benzene dicarboxylic acid and can change the rate of crystal nucleation. MIL-101(Cr) with a small crystal size is expected to aid in the insertion of PEI in the crystals. To this end, further experiments were done with small crystals synthesized using an acetic acid/BDC ratio of 4.

2.3.1 TREN as the Amine Component

Two types of amine-loaded samples were prepared. Those labeled 'grafted' have a sufficiently limited amount of amine such that each molecule could, in principle, graft to an open Cr coordination site. Samples labeled 'impregnated' have additional amine added such that some of the molecules must be physically contained within the pore space without grafting on an open Cr coordination site. Figure 2.2 shows the CO_2 adsorption isotherms for MIL-101(Cr)-TREN (grafted) and MIL-101(Cr) at 298 K. As expected, the CO_2 adsorption is greatly improved as a result of functionalizing the framework with TREN. However, the adsorption at a CO_2 partial pressure of 0.4 mbar, the pressure of relevance for DAC, is only ~0.35 mmol/g. CO_2 capacities in a similar range were obtained by Hu et al.[26] for MIL-101(Cr) loaded with smaller amine molecules such diethylenetriamine (DETA) and diamino-dipropylamine (DADPA). The TREN loading for the material used in Figure 2.2 was 2.63 mmol/g MOF, so the amine efficiency at a CO_2 partial pressure of 0.4 mbar is only ~4%. Thus, despite the improved CO_2 adsorption as a result of functionalization with TREN, the material is unlikely to be effective for DAC. To improve CO_2 adsorption at the partial pressure of 0.4 mbar, a further increase in amine loading was sought through wet impregnation, whereby additional TREN molecules were deposited in the MOF pores, beyond the loading that can chemically bind to open metal coordination sites. As shown in Figure 2.3, observed CO_2 adsorption at 0.4 mbar partial pressure is 2.8 mmol/g which correspond to an improved amine efficiency of ~17% for the sample with an amine loading of 5.67 mmol/g MOF.

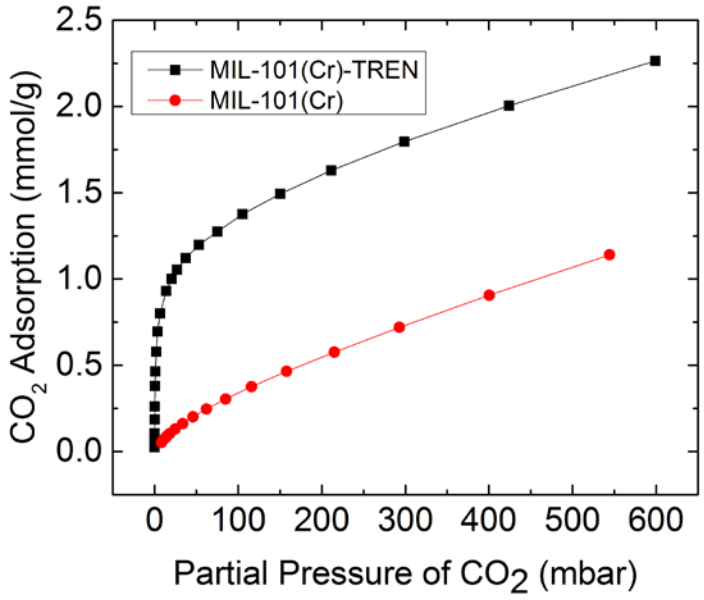

Figure 2.2. CO_2 adsorption as a function of CO_2 partial pressure for MIL-101(Cr)-TREN (grafted) and the bare MOF.

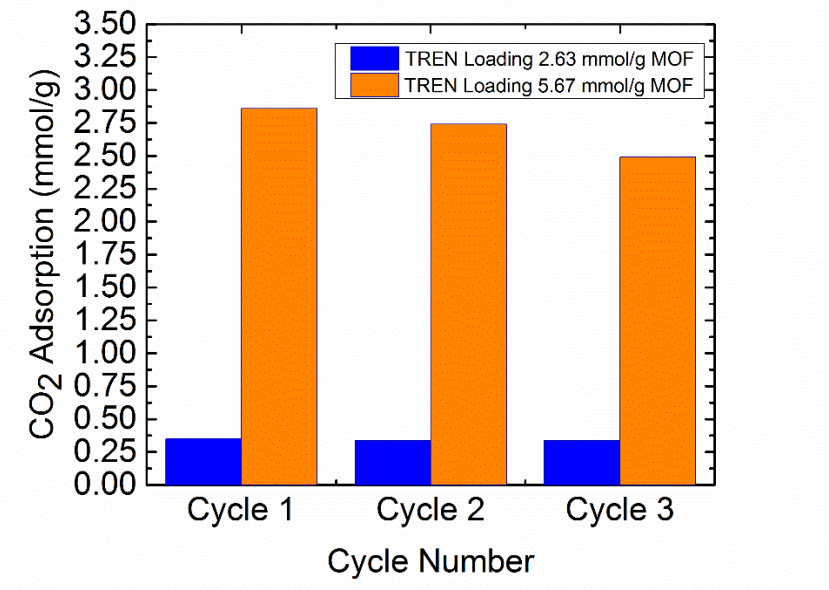

Figure 2.3. Cyclic CO_2 uptake at partial pressure of 0.4 mbar for MIL-101(Cr)-TREN (grafted) and MIL-101 (Cr)-TREN (impregnated).

Stable cyclic CO_2 adsorption with rapid kinetics is important for economical application of adsorbents. Here we first report cyclic adsorption of CO_2 for MIL-101(Cr)-TREN system for three adsorption-desorption cycles using a TGA flowing 400 ppm CO_2

(0.4 mbar partial pressure) in helium. The material was regenerated at 110 °C for 3 h between the cycles before adsorption at 25 °C. Different trends were observed for the two samples with different TREN loadings. The grafted TREN sample (Figure 2.3, blue) showed a stable cyclic performance over three cycles, whereas the impregnated TREN sample (Figure 2.3, orange) showed a significant decline in the capacity in subsequent cycles despite a superior initial adsorption capacity (~2.8 mmol/g). This is attributed to the high volatility of TREN (boiling point 265 °C), leading the weakly adsorbed TREN species to evaporate under the desorption conditions which can be observed as a change in the baseline in Figure A.6. Despite the stable cyclic adsorption capacity of 0.35 mmol/g, the MIL-101(Cr)-TREN (grafted) sample was not considered for further air capture studies, as the capacity is likely too low for practical use.[37]

2.3.2 PEI as the Amine Component

Because some of the lack of cyclic stability in the material discussed above is likely associated with the volatility of the low molecular weight amine (TREN) that was used, the use of less volatile PEI-800 was explored to test whether this would yield a material with improved cyclic adsorption stability. MIL-101(Cr)-PEI-800 samples were made with different loadings of PEI. Specifically, PEI loadings were varied from 0.18-1.8 mmol/g MOF to explore whether there was an optimal loading of PEI for CO_2 adsorption under air capture conditions. Table 2.1 captures the results of elemental analysis, relating the PEI loadings corresponding to the nitrogen content in the material.

Table 2.1. Amine loadings and elemental analysis results for MIL-101(Cr)-PEI-800 samples

Amine Loadings (mmol/g MOF)	C %	H %	N %
0.18	40.5	4.5	4.2
0.36	42.3	5.2	7.5
0.77	43.3	6.2	12.8
0.97	43.8	6.7	14.6
1.06	44.8	6.6	15.4
1.32	41.9	7.6	17.2
1.76	46.7	7.5	19.6

Table A2 lists the BET surface area reduction as a function of amine loading. Figures A.4 and A.5 show powder XRD patterns and N_2 physisorption isotherms for these materials. At higher loadings of PEI, a progressive decrease in intensity of the lower angle XRD peaks was observed. This is attributed to an increase in the organic matter in the material. All the materials showed a characteristic MIL-101(Cr) N_2 physisorption isotherm with secondary uptake around $p/p_0 = 0.2$, but the N_2 physisorption decreased progressively as the amine loadings increased.

Figure 2.4 depicts the pore volume of the sorbents as a function of the PEI-800 loading. The red points represent the pore volume calculated from the cryogenic nitrogen physisorption isotherm at $P/P_o = 0.995$. The black points, representing the theoretical pore volume, are the calculated pore volumes based on the PEI loadings obtained from the elemental analysis. This represents the total pore volume minus the volume occupied by the mass of PEI determined by elemental analysis, using the liquid density of PEI for the mass to volume conversion. Close agreement between the physisorption and theoretical

pore volumes strongly supports the hypothesis of effective insertion of PEI-800 inside the pores of MIL-101 (Cr).

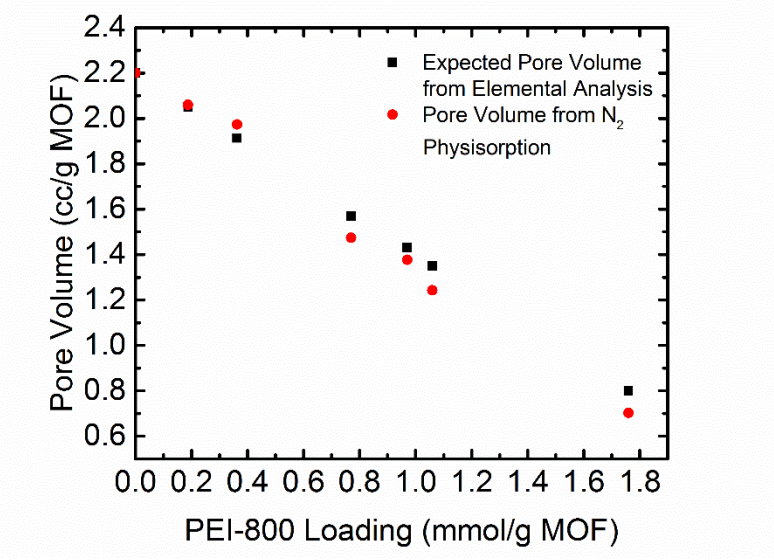

Figure 2.4. Comparison of pore volumes measured by nitrogen physisorption and calculated based on elemental analysis for MIL-101 (Cr)-PEI-800 samples with different loadings of PEI.

Figure 2.5 presents CO_2 adsorption uptakes measured on the TGA at 400 ppm CO_2 concentration by MIL-101-PEI (800) samples with different loadings of PEI-800. At lower PEI loadings, despite relatively higher pore volumes, low CO_2 adsorption capacities were obtained (0.2 – 0.3 mmol/g), representing only 1-3 % amine efficiency (Figure 2.5). As the PEI loading was increased further, despite a continual decrease in the pore volume, the CO_2 adsorption (1.1-1.35 mmol/g) and amine efficiency (~10%) increased dramatically. Improvements in amine efficiency with increasing amine loading have also been observed for mesoporous silica MCM-41/SBA-15 supported PEI samples.[15, 48] This has recently been attributed to changes in the morphology of PEI as the loading increases.[20] Here we hypothesize that at lower loadings of PEI, the polymer interacts strongly with the MOF

framework and many amine sites are not available for CO_2 capture, resulting in a low amine efficiency. It has also been widely empirically observed that amine efficiencies increase with amine loading up to a point where steric constraints prevent effective access to all the amine sites in oxide-supported amine sorbents.[15, 48]

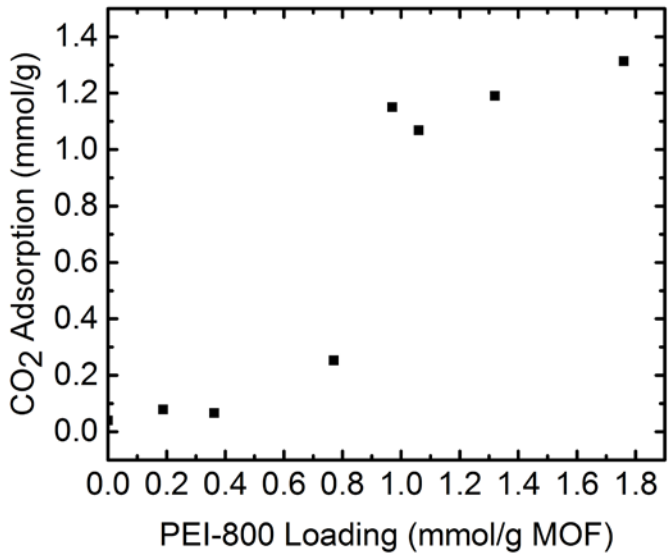

Figure 2.5. Gravimetric CO_2 uptake at 400 ppm for MIL-101 (Cr)-PEI-800 at different loadings of PEI.

While superior capacities were obtained for MIL-101(Cr)-PEI-800 at higher loadings of PEI, it is also worthwhile to compare the best adsorption capacity (1.35 mmol/g) achieved here with other adsorbents for air capture applications. Examples from the literature include: 0.98 mmol/g (TRI-PE-MCM-41[49]), 1.39 mmol/g (nanofibrillated cellulose (NFC) functionalized with N-(2-aminoethyl)-3 aminopropylmethyldimethoxysilane (AEAPDMS)[18]), 1.72 mmol/g (SBA-15 functionalized with hyper branched amino silica[10]), 1.72 mmol/g (Fumed silica functionalized with PEI-25000[7]), 2.2 mmol/g (SBA-15-PEI-800[50]) and 3 mmol/g (Mg_2(dobpdc) functionalized with N,N′-dimethylethylenediamine (mmen)[40]). For similar

amine loadings of PEI (45 wt%) in SBA-15-PEI-800, Choi et al.[10] obtained higher capacities (2.2 mmol/g) and amine efficiencies (22%) air capture studies. This suggests the importance of the interaction of the aminopolymer with the substrate in affecting the sorption accessibility of amine sites for CO_2 adsorption.

Sorbents with CO_2 adsorption capacities of more than 1 mmol/g at 400 ppm CO_2 concentration were explored further via isotherm studies at multiple temperatures, cyclic adsorption-desorption studies, and kinetic studies, as reported below.

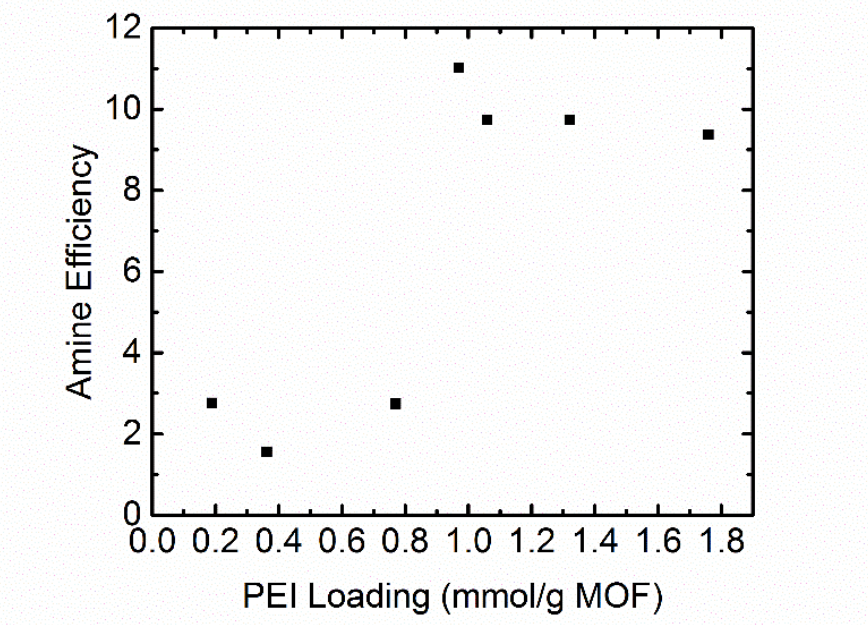

Figure 2.6. Amine efficiencies for MIL-101 (Cr)-PEI-800 samples with different PEI loadings at 400 ppm CO_2 concentration.

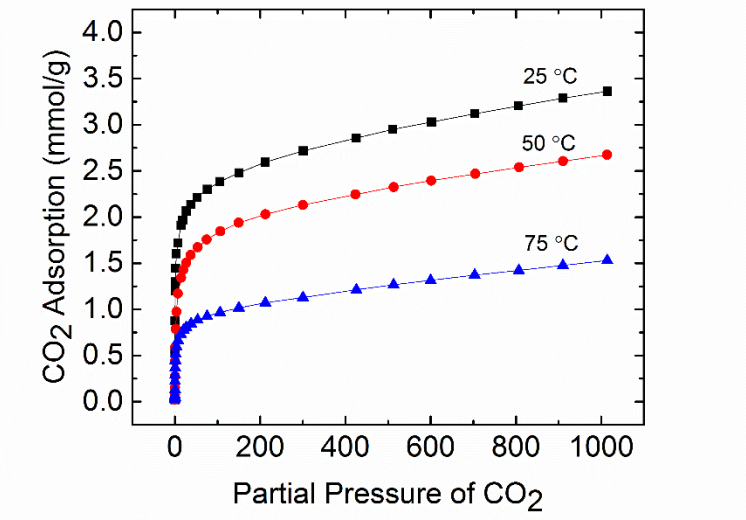

Figure 2.7. CO_2 uptake as a function of temperature for MIL-101(Cr)-PEI-800 with an amine loading of 1.06 mmol/gMOF.

CO_2 adsorption isotherms for a representative high adsorption capacity sample with PEI loading of 1.06 mmol/g MOF were measured at multiple temperatures. An isosteric heat of adsorption 70 kJ/mol of CO_2 adsorbed at very low coverage was obtained using the Clausius Clapeyron equation. As expected thermodynamically, as the temperature increased, the CO_2 adsorption progressively decreased. This is in contrast with sorbents based on PEI loaded into some other supports such as mesoporous silica SBA-15, where it has been reported that modest increases in temperature enhanced CO_2 capture due to kinetic effects.[12, 41]

Cyclic adsorption/desorption studies for MIL-101(Cr)-PEI (800) with a PEI loading of 1.06 mmol/g MOF (Figure 2.8) demonstrated that this material had less loss of capacity during cycling than the MIL-101(Cr)-TREN materials described above (Figure 2.3). The CO_2 uptake dropped 2.7 % and 1.9% after the first and second cycles,

respectively. This is attributed to lower volatility associated with the higher molecular weight of PEI-800 compared to TREN.

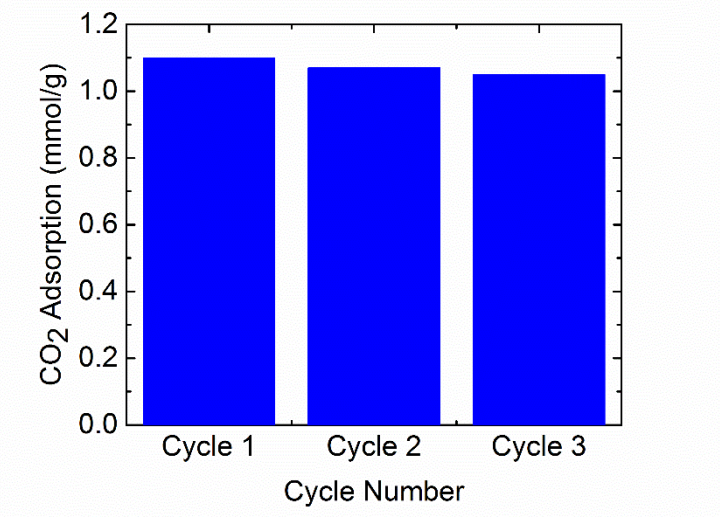

Figure 2.8. Cyclic CO_2 adsorption capacities for MIL-101 (Cr)-PEI with a PEI loading of 1.06 mmol/gMOF.

Figure 2.9 shows the kinetic performance of three MIL-101(Cr) samples with different loadings of PEI-800 via plots of normalized capacity as a function of time. Despite the increase in the CO_2 capacity from 1.1-1.35 mmol CO_2/g-sorbent as a result of higher PEI-loadings, the time required to reach adsorption equilibrium increased significantly with higher PEI loadings. Table 2.2 lists the CO_2 adsorption as a function of time for different PEI loadings (from 0.97-1.76 mmol/g MOF). Sample with PEI loading 0.97 mmol/g MOF achieved equilibrium CO_2 adsorption of 1.15 mmol/g in 240 min vs sample with PEI loading of 1.76 mmol/g MOF, which took 340 min to achieve adsorption of 1.35 mmol/g.

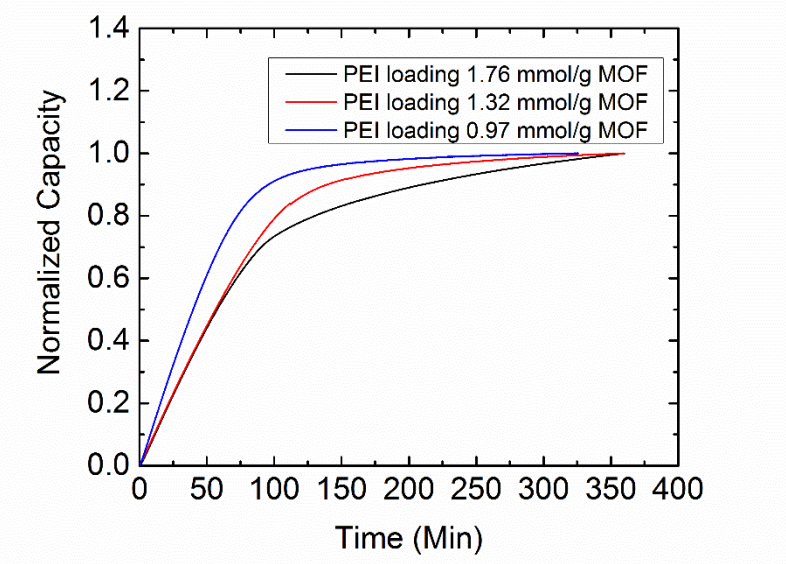

Figure 2.9. Normalized CO_2 uptake (capacity at t / capacity at t_∞) as a function of time for MIL-101(Cr)-PEI at different PEI loadings.

The difference in the kinetics of the samples with PEI loadings of 1.32 mmol/g MOF and 1.76 mmol/g MOF was quite significant, with a long tail for the sample with the higher PEI loading representing increased diffusion resistance encountered by CO_2 because of the high loading of PEI. Bollini et al. made similar observations for high loadings of aminopropyl silane in mesoporous silica SBA-15.[53]

Table 2.2. CO_2 adsorption (mmol/g) in MIL-101(Cr)-PEI-800 as a function of time (min)

Time (Min)	MIL-101(Cr)-PEI-0.97 (mmol/g)	MIL-101(Cr)-PEI-1.32 (mmol/g)	MIL-101(Cr)-PEI-1.76 (mmol/g)
25	0.42	0.27	0.29
50	0.70	0.52	0.58
75	0.93	0.76	0.80
100	1.04	0.95	0.98
Equilibrium	1.15 (237 min)	1.20 (306 min)	1.35 (341 min)

Even though high capacities are achievable at higher loadings, the tradeoffs between adsorption uptake and adsorption kinetics put practical limits on possible cyclic adsorption-

desorption cycles. Considering these tradeoffs between adsorption capacity and kinetics, a PEI loading of 1.0-1.1 mmol/ g MOF (~85 wt %) is suggested to be most useful for MIL-101(Cr) under the conditions employed.

2.4 Conclusions

The CO_2 adsorption uptake capacity and kinetics, along with the associated amine efficiencies for different masses of TREN and PEI-800 loaded into MIL-101(Cr), have been reported. MIL-101(Cr) grafted with TREN demonstrated enhanced CO_2 capture over the original, amine-free framework, but the amines were not very effective for CO_2 capture. Higher loadings of TREN obtained physical impregnation of an additional amine into the pore space improved the amine efficiency and CO_2 adsorption uptake, but the amines were labile and could be lost during thermal cycling because of the relatively high volatility of TREN. Similar CO_2 capacities[26] at 400 ppm with other small molecules such DETA, DADPA indicate that these adsorbents are not very effective for air capture applications. MIL-101(Cr) functionalized with PEI showed low amine efficiencies at low loadings of PEI, but amine efficiencies improved substantially as the loading of PEI-800 was increased. At the highest amine loadings, kinetic limitations associated with pore blockage led to only modest increases in uptake and substantially slowed adsorption kinetics. This suggests there is a compositional window where a balance of the CO_2 uptake and kinetics will be optimized for this family of materials. The amine-modified MOF adsorbents were also evaluated in a cyclic CO_2 adsorption/desorption cycles under simulated air capture conditions, demonstrating that the optimal MIL-101(Cr)-PEI material had relatively good stability under lab scale temperature swing adsorption conditions.

2.5 References

1. Kirtman, B.; Power, S. B.; Adedoyin, J. A.; Boer, G. J.; Bojariu, R.; Camilloni, I.; Doblas-Reyes, F. J.; Fiore, A. M.; Kimoto, M.; Meehl, G. A.; Prather, M.; Sarr, A.; Schär, C.; Sutton, R.; van Oldenborgh, G. J.; Vecchi, G.; Wang, H. J., Near-term Climate Change: Projections and Predictability. In *Climate Change 2013: The Physical Science Basis. Contribution of Working Group I to the Fifth Assessment Report of the Intergovernmental Panel on Climate Change*, Stocker, T. F.; Qin, D.; Plattner, G.-K.; Tignor, M.; Allen, S. K.; Boschung, J.; Nauels, A.; Xia, Y.; Bex, V.; Midgley, P. M., Eds. Cambridge University Press: Cambridge, United Kingdom and New York, NY, USA, **2013**; 953–1028.

2. U.S. Greenhouse Gas Inventory Report: 1990-2013. April 15, 2015 ed.; Environmental Protection Agency: **2015**.

3. Rao, A. B.; Rubin, E. S., A Technical, Economic, and Environmental Assessment of Amine-Based CO_2 Capture Technology for Power Plant Greenhouse Gas Control. *Environ. Sci. Technol.* **2002,** *36* (20), 4467-4475.

4. Goto, K.; Yogo, K.; Higashii, T., A review of efficiency penalty in a coal-fired power plant with post-combustion CO_2 capture. *Appl. Energy* **2013,** *111*, 710-720.

5. Lackner, K. S.; Brennan, S.; Matter, J. M.; Park, A. H.; Wright, A.; van der Zwaan, B., The urgency of the development of CO_2 capture from ambient air. *Proc. Natl. Acad. Sci. U S A* **2012,** *109* (33), 13156-62.

6. Jones, C. W., CO_2 capture from dilute gases as a component of modern global carbon management. *Annu. Rev. Chem. Biomol. Eng.* **2011,** *2*, 31-52.

7. Goeppert, A.; Czaun, M.; Prakash, G. S.; Olah, G. A., Air as the renewable carbon source of the future: an overview of CO_2 capture from the atmosphere. *Energy Environ. Sci.* **2012,** *5* (7), 7833-7853.

8. Trends in Atmospheric Carbon Dioxide. National Oceanic & Atmospheric Administration **2015**.

9. Bollini, P.; Didas, S. A.; Jones, C. W., Amine-oxide hybrid materials for acid gas separations. *J. Mater. Chem.* **2011,** *21* (39), 15100-15120.

10. Choi, S.; Drese, J. H.; Eisenberger, P. M.; Jones, C. W., Application of Amine-Tethered Solid Sorbents for Direct CO_2 Capture from the Ambient Air. *Environ. Sci. Technol.* **2011,** *45* (6), 2420-2427.

11. Donaldson, T. L.; Nguyen, Y. N., Carbon Dioxide Reaction Kinetics and Transport in Aqueous Amine Membranes. *Ind. Eng. Chem. Fund.* **1980,** *19* (3), 260-266.

12. Chaikittisilp, W.; Khunsupat, R.; Chen, T. T.; Jones, C. W., Poly (allylamine)–mesoporous silica composite materials for CO_2 capture from simulated flue gas or ambient air. *Ind. Eng. Chem. Res.* **2011,** *50* (24), 14203-14210.

13. Goeppert, A.; Czaun, M.; May, R. B.; Prakash, G. K. S.; Olah, G. A.; Narayanan, S. R., Carbon Dioxide Capture from the Air Using a Polyamine Based Regenerable Solid Adsorbent. *J. Am. Chem. Soc.* **2011,** *133* (50), 20164-20167.

14. Sakwa-Novak, M. A.; Tan, S.; Jones, C. W., Role of Additives in Composite PEI/Oxide CO_2 Adsorbents: Enhancement in the Amine Efficiency of Supported PEI by PEG in CO_2 Capture from Simulated Ambient Air. *ACS Appl. Mater. Interf.* **2015**, 7 (44), 24748-24759.

15. Xu, X.; Song, C.; Andrésen, J. M.; Miller, B. G.; Scaroni, A. W., Preparation and characterization of novel CO_2 "molecular basket" adsorbents based on polymer-modified mesoporous molecular sieve MCM-41. *Micropor. Mesopor. Mater.* **2003,** *62* (1–2), 29-45.

16. Sakwa-Novak, M. A.; Jones, C. W., Steam Induced Structural Changes of a Poly(ethylenimine) Impregnated γ-Alumina Sorbent for CO_2 Extraction from Ambient Air. *ACS Appl. Mater. Interf.* **2014,** *6* (12), 9245-9255.

17. Zhang, W.; Liu, H.; Sun, C.; Drage, T. C.; Snape, C. E., Capturing CO_2 from ambient air using a polyethyleneimine–silica adsorbent in fluidized beds. *Chem. Eng. Sci.* **2014,** *116*, 306-316.

18. Gebald, C.; Wurzbacher, J. A.; Tingaut, P.; Zimmermann, T.; Steinfeld, A., Amine-Based Nanofibrillated Cellulose As Adsorbent for CO_2 Capture from Air. *Environ. Sci. Technol.* **2011,** *45* (20), 9101-9108.

19. Chen, Z.; Deng, S.; Wei, H.; Wang, B.; Huang, J.; Yu, G., Polyethylenimine-Impregnated Resin for High CO_2 Adsorption: An Efficient Adsorbent for CO_2 Capture from Simulated Flue Gas and Ambient Air. *ACS Appl. Mater. Interf.* **2013,** *5* (15), 6937-6945.

20. Holewinski, A.; Sakwa-Novak, M. A.; Jones, C. W., Linking CO_2 Sorption Performance to Polymer Morphology in Aminopolymer/Silica Composites through Neutron Scattering. *J. Am. Chem. Soc.* **2015,** *137* (36), 11749-11759.

21. Yue, M. B.; Chun, Y.; Cao, Y.; Dong, X.; Zhu, J. H., CO_2 Capture by As-Prepared SBA-15 with an Occluded Organic Template. *Adv. Funct. Mater.* **2006,** *16* (13), 1717-1722.

22. Plaza, M. G.; Pevida, C.; Arenillas, A.; Rubiera, F.; Pis, J. J., CO_2 capture by adsorption with nitrogen enriched carbons. *Fuel* **2007,** *86* (14), 2204-2212.

23. Chung, Y. G.; Camp, J.; Haranczyk, M.; Sikora, B. J.; Bury, W.; Krungleviciute, V.; Yildirim, T.; Farha, O. K.; Sholl, D. S.; Snurr, R. Q., Computation-Ready,

Experimental Metal–Organic Frameworks: A Tool To Enable High-Throughput Screening of Nanoporous Crystals. *Chem. Mater.* **2014,** *26* (21), 6185-6192.

24. D'Alessandro, D. M.; Smit, B.; Long, J. R., Carbon Dioxide Capture: Prospects for New Materials. *Angew. Chem. Int. Ed.* **2010,** *49* (35), 6058-6082.

25. Furukawa, H.; Cordova, K. E.; O'Keeffe, M.; Yaghi, O. M., The Chemistry and Applications of Metal-Organic Frameworks. *Science* **2013,** *341* (6149).

26. Keskin, S.; van Heest, T. M.; Sholl, D. S., Can Metal–Organic Framework Materials Play a Useful Role in Large-Scale Carbon Dioxide Separations? *ChemSusChem* **2010,** *3* (8), 879-891.

27. McDonald, T. M.; Lee, W. R.; Mason, J. A.; Wiers, B. M.; Hong, C. S.; Long, J. R., Capture of carbon dioxide from air and flue gas in the alkylamine-appended metal-organic framework mmen-Mg_2(dobpdc). *J. Am. Chem. Soc.* **2012,** *134* (16), 7056-65.

28. Darunte, L. A.; Walton, K. S.; Sholl, D. S.; Jones, C. W., CO_2 capture via adsorption in amine-functionalized sorbents. *Curr. Opin. Chem. Eng.* **2016,** *12*, 82-90.

29. Hong, D.-Y.; Hwang, Y. K.; Serre, C.; Férey, G.; Chang, J.-S., Porous Chromium Terephthalate MIL-101 with Coordinatively Unsaturated Sites: Surface Functionalization, Encapsulation, Sorption and Catalysis. *Adv. Funct. Mater.* **2009,** *19* (10), 1537-1552.

30. Hwang, Y. K.; Hong, D.-Y.; Chang, J.-S.; Jhung, S. H.; Seo, Y.-K.; Kim, J.; Vimont, A.; Daturi, M.; Serre, C.; Férey, G., Amine Grafting on Coordinatively Unsaturated Metal Centers of MOFs: Consequences for Catalysis and Metal Encapsulation. *Angew. Chem.* **2008,** *120* (22), 4212-4216.

31. Liu, Q.; Ning, L.; Zheng, S.; Tao, M.; Shi, Y.; He, Y., Adsorption of Carbon Dioxide by MIL-101(Cr): Regeneration Conditions and Influence of Flue Gas Contaminants. *Sci. Rep.* **2013,** *3*, 2916.

32. Wang, X.; Li, H.; Hou, X.-J., Amine-Functionalized Metal Organic Framework as a Highly Selective Adsorbent for CO_2 over CO. *J. Phys. Chem. C* **2012,** *116* (37), 19814-19821.

33. Anbia, M.; Hoseini, V., Enhancement of CO_2 adsorption on nanoporous chromium terephthalate (MIL-101) by amine modification. *J. Nat. Gas Chem.* **2012,** *21* (3), 339-343.

34. Hu, Y.; Verdegaal, W. M.; Yu, S. H.; Jiang, H. L., Alkylamine-tethered stable metal-organic framework for CO_2 capture from flue gas. *ChemSusChem* **2014,** *7* (3), 734-7.

35. Lin, Y.; Yan, Q.; Kong, C.; Chen, L., Polyethyleneimine incorporated metal-organic frameworks adsorbent for highly selective CO_2 capture. *Sci. Rep.* **2013,** *3*, 1859.

36. Lin, Y.; Lin, H.; Wang, H.; Suo, Y.; Li, B.; Kong, C.; Chen, L., Enhanced selective CO_2 adsorption on polyamine/MIL-101(Cr) composites. *J. Mater. Chem. A* **2014,** *2* (35), 14658-14665.

37. Choi, S.; Watanabe, T.; Bae, T.-H.; Sholl, D. S.; Jones, C. W., Modification of the Mg/DOBDC MOF with Amines to Enhance CO_2 Adsorption from Ultradilute Gases. *J. Phys. Chem. Lett.* **2012,** *3* (9), 1136-1141.

38. Andirova, D.; Lei, Y.; Zhao, X.; Choi, S., Functionalization of Metal-Organic Frameworks for Enhanced Stability under Humid Carbon Dioxide Capture Conditions. *ChemSusChem* **2015**, *8*(20):3405-9.

39. Planas, N.; Dzubak, A. L.; Poloni, R.; Lin, L. C.; McManus, A.; McDonald, T. M.; Neaton, J. B.; Long, J. R.; Smit, B.; Gagliardi, L., The mechanism of carbon dioxide adsorption in an alkylamine-functionalized metal-organic framework. *J. Am. Chem. Soc.* **2013,** *135* (20), 7402-5.

40. McDonald, T. M.; Mason, J. A.; Kong, X.; Bloch, E. D.; Gygi, D.; Dani, A.; Crocella, V.; Giordanino, F.; Odoh, S. O.; Drisdell, W. S.; Vlaisavljevich, B.; Dzubak, A. L.; Poloni, R.; Schnell, S. K.; Planas, N.; Lee, K.; Pascal, T.; Wan, L. F.; Prendergast, D.; Neaton, J. B.; Smit, B.; Kortright, J. B.; Gagliardi, L.; Bordiga, S.; Reimer, J. A.; Long, J. R., Cooperative insertion of CO_2 in diamine-appended metal-organic frameworks. *Nature* **2015,** *519* (7543), 303-8.

41. Drisdell, W. S.; Poloni, R.; McDonald, T. M.; Pascal, T. A.; Wan, L. F.; Pemmaraju, C. D.; Vlaisavljevich, B.; Odoh, S. O.; Neaton, J. B.; Long, J. R.; Prendergast, D.; Kortright, J. B., Probing the mechanism of CO_2 capture in diamine-appended metal-organic frameworks using measured and simulated X-ray spectroscopy. *Phys. Chem. Chem. Phys.* **2015,** *17* (33), 21448-21457.

42. Kizzie, A. C.; Wong-Foy, A. G.; Matzger, A. J., Effect of humidity on the performance of microporous coordination polymers as adsorbents for CO_2 capture. *Langmuir* **2011,** *27* (10), 6368-73.

43. Bromberg, L.; Diao, Y.; Wu, H.; Speakman, S. A.; Hatton, T. A., Chromium(III) Terephthalate Metal Organic Framework (MIL-101): HF-Free Synthesis, Structure, Polyoxometalate Composites, and Catalytic Properties. *Chem. Mater.* **2012,** *24* (9), 1664-1675.

44. Walton, K. S.; Snurr, R. Q., Applicability of the BET Method for Determining Surface Areas of Microporous Metal−Organic Frameworks. *J. Am. Chem. Soc.* **2007,** *129* (27), 8552-8556.

45. Jiang, D.; Burrows, A. D.; Edler, K. J., Size-controlled synthesis of MIL-101(Cr) nanoparticles with enhanced selectivity for CO_2 over N_2. *CrystEngComm* **2011,** *13* (23), 6916-6919.

46. Diring, S.; Furukawa, S.; Takashima, Y.; Tsuruoka, T.; Kitagawa, S., Controlled Multiscale Synthesis of Porous Coordination Polymer in Nano/Micro Regimes. *Chem. Mater.* **2010,** *22* (16), 4531-4538.

47. Kulkarni, A. R.; Sholl, D. S., Analysis of Equilibrium-Based TSA Processes for Direct Capture of CO_2 from Air. *Ind. Eng. Chem. Res.* **2012,** *51* (25), 8631-8645.

48. Satyapal, S.; Filburn, T.; Trela, J.; Strange, J., Performance and Properties of a Solid Amine Sorbent for Carbon Dioxide Removal in Space Life Support Applications. *Energy Fuels* **2001,** *15* (2), 250-255.

49. Belmabkhout, Y.; Serna-Guerrero, R.; Sayari, A., Adsorption of CO_2-Containing Gas Mixtures over Amine-Bearing Pore-Expanded MCM-41 Silica: Application for Gas Purification. *Ind. Eng. Chem. Res.* **2010,** *49* (1), 359-365.

50. Choi, S.; Gray, M. L.; Jones, C. W., Amine-Tethered Solid Adsorbents Coupling High Adsorption Capacity and Regenerability for CO_2 Capture From Ambient Air. *ChemSusChem* **2011,** *4* (5), 628-635.

51. Sanz, R.; Calleja, G.; Arencibia, A.; Sanz-Pérez, E. S., CO_2 adsorption on branched polyethyleneimine-impregnated mesoporous silica SBA-15. *Appl. Surf. Sci.* **2010,** *256* (17), 5323-5328.

52. Xu, X.; Song, C.; Andresen, J. M.; Miller, B. G.; Scaroni, A. W., Novel Polyethylenimine-Modified Mesoporous Molecular Sieve of MCM-41 Type as High-Capacity Adsorbent for CO_2 Capture. *Energy Fuels* **2002,** *16* (6), 1463-1469.

53. Bollini, P.; Brunelli, N. A.; Didas, S. A.; Jones, C. W., Dynamics of CO_2 Adsorption on Amine Adsorbents. 2. Insights Into Adsorbent Design. *Ind. Eng. Chem. Res.* **2012,** *51* (46), 15153-15162.

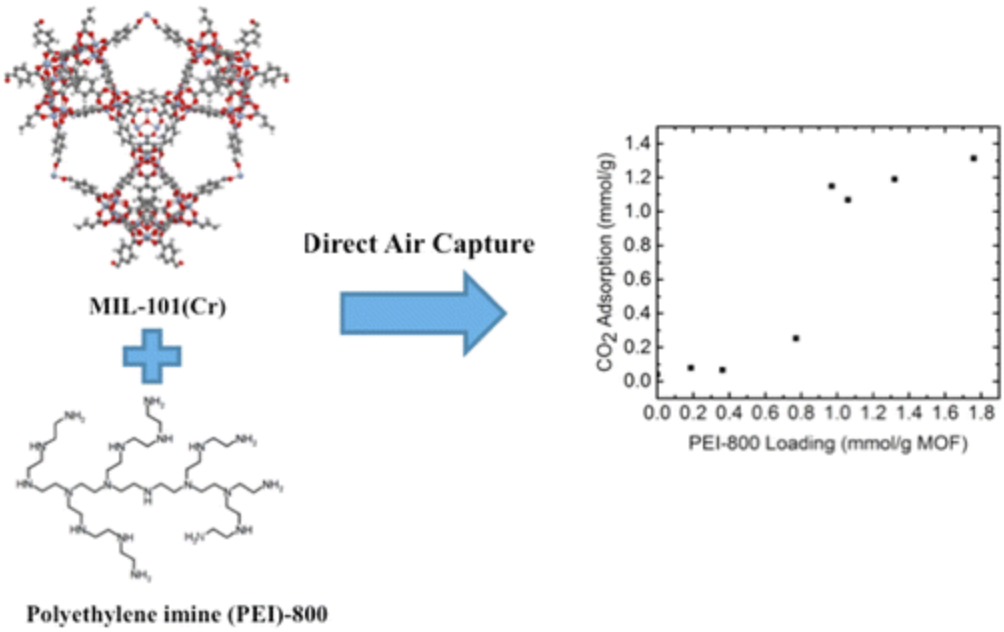
MIL-101(Cr)
Polyethylene imine (PEI)-800
Direct Air Capture
CO_2 Adsorption (mmol/g)
PEI-800 Loading (mmol/g MOF)
0.0 0.2 0.4 0.6 0.8 1.0 1.2 1.4
0.0 0.2 0.4 0.6 0.8 1.0 1.2 1.4 1.6 1.8

3 MONOLITH-SUPPORTED AMINE-FUNCTIONALIZED Mg_2(dobpdc) FOR CO_2 CAPTURE

Parts of this chapter are reproduced from 'Darunte, L. A.**;** Terada, Y. Murdock. C.M.; Walton, K. S.; Sholl, D. S.; Realff M.J.; Jones, C. W., Monolith-Supported Amine-Functionalized Mg_2(dobpdc) Adsorbents for CO_2 Capture. *ACS Applied Materials & Interfaces* **2017**,9 (20), pp 17042–17050' with a permission from American Chemical Society

3.1 Introduction

Carbon capture is gaining importance as a way to mitigate climate change associated with increased emissions of CO_2. One approach is to use solid supported amine materials that have shown excellent performance for CO_2 capture because of the strong acid-base interaction between the amines and CO_2. Various support materials such as silica,[1–3] alumina,[4] carbon,[5,6] and metal organic frameworks (MOFs)[7–9] have been used for functionalization with amines to enhance CO_2 adsorption at low CO_2 partial pressures. Recently MOFs have attracted considerable attention as both adsorbents and supports because of their tunability and excellent CO_2 adsorption characteristics.[10,11] MIL-101(Cr) functionalized with different amines[12–14] and N-N' dimethyl-ethylene diamine (mmen) functionalized M_2(dobpdc) (dobpdc^{4-} = 4,4′-dioxido-3,3′-biphenyldicarboxylate, M = Mg, Mn, Zn, Ni, Co,Fe), reported by McDonald et al.,[8,15] are noted for outstanding CO_2 adsorption for both direct air capture and flue gas capture conditions. Mmen-M_2(dobpdc)

has an attractive performance for CO_2 capture because of its phase change characteristics in its CO_2 adsorption isotherm. Hefti et al.[16] analyzed MOFs in the series of mmen-M_2(dobpdc) containing different metals (M = Mg, Mn, Zn, Ni, Co,Fe) for a temperature swing adsorption cycle for CO_2 capture from flue gas and noted the potential of mmen-Mg_2(dobpdc) and mmen-Mn_2(dobpdc) to achieve a high recovery and purity.

For practical application of CO_2 capture from flue gas[17] or ambient air,[18] it is necessary to process high flow rates of gases during CO_2 adsorption. This can be achieved through a fluidized bed of sorbents,[19,20] or the use of structured supports such as hollow fibers[21,22] or honeycomb monoliths. [23–27] While fluidized bed configurations can provide a high adsorbent loading, they suffer from particle aggregation and loss of the sorbent.[28] Honeycomb monoliths have the advantage of lower pressure drops at a high flow rates along with superior mass and heat transfer compared to fluidized bed or packed bed.[29] Cordierite has been a preferred material for the construction of monoliths because of its low coefficient of thermal expansion, which is important in many high temperature catalytic applications. Such monoliths can be washcoated with high surface area, porous materials to create solids with improved specific surface area (see Figure 3.1). Alumina and other porous metal oxides are promising porous materials for use as coatings.

Eisenberger proposed a monolith based amine functionalized system for CO_2 capture from ambient air.[26] Later, Kulkarni and Sholl[30] analyzed an equilibrium based process for temperature swing adsorption process using an amine-functionalized silica adsorbent, TRI-PE-MCM-41,[2] coated on structured monolithic contactors. They identified the need for high adsorbent capacity to reduce parasitic energy losses associated with the

monolithic contactor. Sinha et al.[31] analyzed the potential of MIL-101(Cr)-PEI-800 and mmen-Mg_2(dobpdc) for a direct air capture process based on adsorbents coated on a cordierite monoliths and identified a variety of factors that are important for a practical, large scale air capture process.

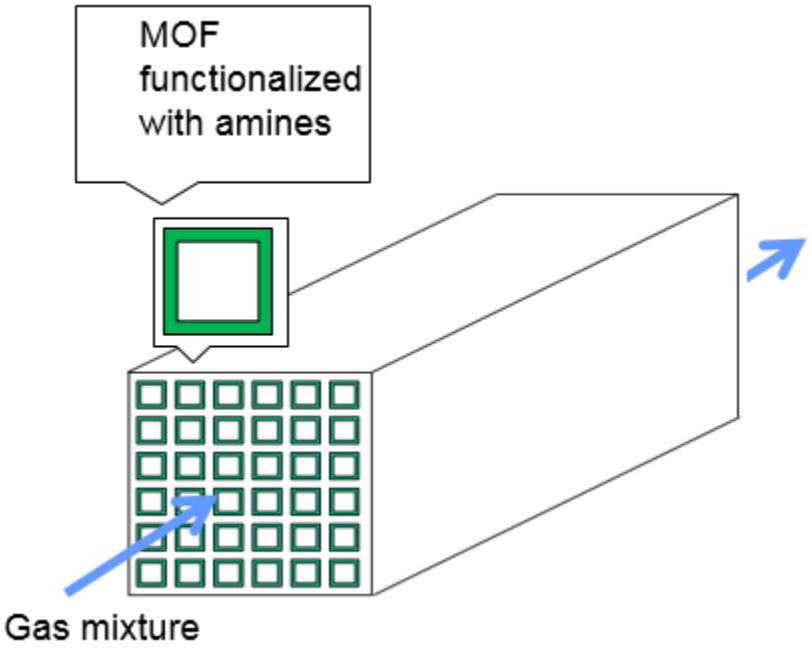

Figure 3.1. Monolith supported MOF system for CO_2 capture applications. Epitaxial MOF films can be grown on the inner walls in the channels of the monolith to capture CO_2 from gas mixtures.

While there are several examples of zeolite adsorbents on monoliths,[32,33] experimental demonstrations of MOF catalysts or sorbents on monoliths are rare. There is a potential to couple the high geometric surface area of monoliths with high CO_2 adsorption capacities of MOFs by creating amine-modified MOF films on porous monolith structures. Detailed reviews by Cohene et. al.[34] and Woll et. al.[35] outline some strategies used to create MOF films on different substrates. Some notable studies are briefly mentioned here.

Fernandez et al.[36] developed the method of dip coating the cordierite monolith with a seed solution of MIL-101(Cr) in ethanol followed by secondary growth to obtain MIL-101(Cr) films of up to 10 μm thickness. They suggested that MOF- α-alumina interactions achieved were mainly of acid-base nature. Hydroxyl (OH^-) groups from α-alumina were suggested to interact with carboxylic acid groups of BDC ligand of MIL-101(Cr) to create a MIL-101(Cr) film on the surface. Burros and coworkers[37] used a mixture of high molecular weight PEI and MIL-101(Cr) crystals to create a 10 μm film on the surface of an anodisc (aluminum oxide in disc form) using a dip coating procedure. In general, the choice of solvent in the reaction and seeding methods have been shown to be important in creating a uniform coating with strong adhesion to the substrate. Wang et al.[38] created a uniform membrane of Mg-MOF-74 by using an MgO seed layer on α-alumina substrates and observed enhanced permeation selectivity of H_2 over CO_2 by functionalizing the MOF membrane with ethylene diamine (ED). This was attributed to preferential adsorption of CO_2 by the MOF membrane. Fischer and coworkers[39] used in-situ growth in a dimethylformamide (DMF) / water / ethanol (EtOH) mixture to create a film of Mg-MOF-74. They observed a thin and weakly bound film when the previously published,[40,41] one-step Mg-MOF-74 procedures were used. They also noted that for the Ni-MOF-74 series, a tetrahydrofuran (THF) / water mixture produced more uniform films instead of the standard solution of DMF / water / EtOH. In each of the above cases, an MOF film of 6-10 μm was grown on the α-alumina substrate. Lee et al.[42] used layer by layer synthesis (LBL) to create a film of Ni-MOF-74 on α–alumina. In that work, the α–alumina was first immersed in the solution of 2, 5-dihydroxyterepthalic acid in a THF / water mixture followed by dipping in

the solution of nickel acetate in THF/DI water mixture. This LBL process followed by secondary growth in a more concentrated solution created a uniform and strongly bound film on the α-alumina surface. This approach was further employed by Rezaei et al.[43] to grow Ni-MOF-74 films on a cordierite monolith. They observed the MOF in the film form was only ~30% effective compared to powders for CO_2 adsorption at 1 bar.

For MOFs with open metal sites (e.g. MOF-74 or M-dobdc series; M-dobpdc series), stability under humid conditions often limits their practical utility. Kizzie et al.[44] studied the effect of humidity on CO_2 adsorption for different MOFs in the MOF-74 series and found a varying level of degradation and loss of CO_2 adsorption. They observed 84% and 40% loss of CO_2 adsorption for flue gas capture for Mg_2(dobdc) and Ni_2(dobdc) after exposure to 70% relative humidity. Andirova et al.[45] and Choi et al.[9] reported improved stability of the Mg_2(dobdc) framework after functionalization with ethylenediamine (ED). Functionalization of MOFs with amines may be a general and promising approach to enhance sorbent stability of MOFs containing open metal sites under humid conditions.

In the present chapter, to develop MOFs toward practical applications, we first analyze Mn_2(dobpdc) and Mg_2(dobpdc) functionalized with N-N' dimethyl-ethylene diamine (mmen) for stability under humid conditions. Then, we report the development of stable and uniform films of Mg_2(dobpdc) functionalized with N-N' dimethyl-ethylene diamine (mmen) on a 100 CPSI (cells per square inch) cordierite monolith washcoated with α -alumina. Creation of MOF films on a monolith surface has several challenges. Uniform coating, strong film adhesion to the monolith surface and favorable orientation of the MOF crystals for effective gas uptake are some of the desirable features of MOF films for

adsorption/desorption separation applications. To this end, these aspects are explored for the synthesized MOF films on monolith substrates, and we demonstrate here that effective, CO_2 adsorbing mmen-Mg_2(dobpdc) films can be prepared on a structured substrate.

3.2 Experimental Section

3.2.1 Material synthesis

Materials: *Substrates*: Cordierite monoliths (Figure B.1 right) washcoated with α-alumina (100 cells per square inch) were obtained from Applied Catalysts Co. USA. Flat nonporous α-alumina plates (Figure B.1 left) (1 inch in diameter) were obtained from Coorstek Co. USA.

Chemicals: MgO (nano powder <50 nm, Sigma Aldrich), $Mg(NO_3)_2$, $6H_2O$ (Fischer, reagent grade), $MnCl_2$, $4H_2O$ (Alfa Aesar, reagent grade) poly(ethylene imine) (PEI) (reagent grade, Mw 25000), N-N' dimethyl ethylene diamine (Fischer, reagent grade) and methanol (BDH Chemicals, ACS grade) were used as received.

Prior to the development of MOF films, monoliths were activated by washing in 1 M NaOH solution followed by washing with de-ionized (DI) water and methanol. Before the development of MOF film, monolith pieces were dried at 100 °C under 10 mtorr vacuum. H_4(dobpdc) was synthesized following the recipe of McDonald et al.[8] mmen-M_2(dobpdc) (M = Mg & Mn) powders were synthesized following the recipe of McDonald et al.[15]

Seeding of monolith surface with MgO: MgO and PEI-25000 were added to 5 mL of methanol to achieve MgO concentration of 10% by weight. The solution was sonicated for

1 h to create a nanoparticle suspension. A small piece of the monolith was soaked in the solution for 1 min. After that, excess methanol solution was removed by an air knife. After that, rapid drying of the monolith is achieved in 70 °C oven. This process was repeated 6 times with soak times of 1 min. and drying times of 4 min. Finally, MgO coated monoliths were dried at 70 °C overnight.

Scale up of Mg_2(dobpdc) synthesis and growth on the monolith surface: MgO seeds on the monolith were converted to Mg_2(dobpdc) using a modified recipe from Maserati et al.[46] At first, scaling up of the Mg_2(dobpdc) synthesis in 2.5-5 mL DMF solution was studied with H_4(dobpdc) concentration of 0.05 M, 0.1 M, and 0.2 M and fixed MgO amount (0.5 mmol). The reaction was carried out at 120 °C for 18 h. For a robust growth MOF growth on a monolith, ligand concentration of 0.05 M was used with the ratio of 0.5:1 for H_4(dobpdc):MgO. Secondary MOF growth and amine functionalization were achieved following the modified recipe of McDonald et al.[15] with a lower concentration of H_4(dobpdc) and $Mg(NO_3)_2$ to reduce homogeneous nucleation in the solution. The monolith supported MOF was activated for 24 h at 250 °C under 10 mtorr vacuum. Amine functionalization was performed in a glovebox in an N_2 rich environment to avoid contact with moisture and oxygen.

MgO and MOF loadings on a monolith were calculated based on the weight increase during each MgO/MOF film development step. Before seeding the monolith with MgO, the weight of the monolith was measured after drying at 100 °C. The monolith coated with MgO was dried at 70 °C overnight. The monolith coated with MOF was dried in flowing helium at 100 °C during an adsorption experiment on the thermogravimetric analyzer

(TGA) to quantify the MOF loading. MOF films were also grown on flat α-alumina plates following similar experimental procedures to facilitate analysis by X-ray diffraction for structural characterization.

3.2.2 Characterization

N_2 physisorption: N_2 adsorption at 77 K on the monolith and MOF powder was measured using a Micromeritics ASAP 2020 (monolith) or 3Flex (mmen-MOF powders) surface area analyzer. In a typical experiment, 50 mg of powder/0.1-0.2 g piece of were used. The microporous surface area was estimated using the BET method following criteria outlined by Walton et al.[47] in the P/P_0 range of 0.005-0.03. Samples were outgassed at 250 °C for 24 h under 10 mtorr vacuum.

Powder X-ray diffraction (PXRD) measurements on MOF powders as well as MOF films grown on flat α-alumina plates were made using a PANalytical X'Pert diffractometer using Cu Kα radiation.

CO_2 adsorption experiments: CO_2 adsorption was measured on a TA instruments Q500 thermogravimetric analyzer (TGA). In typical experiments, the monolith system was dried in flowing helium (90 mL/h) for 4 h at 100 °C followed by adsorption with 10 % CO_2 mixture in helium (90 mL/h) with the adsorption time of 4 h. Adsorption experiments were performed on a small section of monolith (0.1-0.2 g) at 25°C.

H_2O adsorption experiments: A Micromeritics 3Flex surface characterization analyzer was used to measure water vapor adsorption isotherms to ascertain the stability of mmen-

Mg_2(dobpdc) under humid conditions. MOF powders were activated at 100 °C for 4 h and single component H_2O adsorption measurements were measured at 25 °C for 0.05-0.7 relative humidity. Nitrogen physisorption at 77 K was measured before and after the H_2O adsorption without exposing samples to the atmosphere. After H_2O adsorption studies, samples were carefully transferred to TGA for CO_2 adsorption experiments with minimum exposure to ambient conditions. Before each CO_2 adsorption experiment, samples were dried to remove residual solvent following the procedure outlined in the previous section.

Scanning electron microscopy was performed using Hitachi SU 8230 cold field emission microscope as well as a Hitachi Tabletop SEM TM 3030. Measurements were made using an accelerating voltage of 1 kV and 10 µA current. The Hitachi SU 8230 was also used to measure surface composition using energy dispersive X-ray spectroscopy (EDX). Measurements were made with accelerating voltage of 10 kV and 30 µA current. Calibration signal was obtained with titanium signal at the working distance of 15 mm. The N content was used to ascertain the amine loading of the sample.

3.3 Results and Discussion

3.3.1 Stability under humid conditions

Stability under humid conditions is important for practical applications of adsorbents. As a first step, the stability of mmen-Mg_2(dobpdc) and mmen-Mn_2(dobpdc) under humid conditions was investigated using two bulk characterization techniques, N_2 physisorption and powder XRD. CO_2 adsorption using 10% CO_2 in helium was also measured before and after water exposure. Figure 3.2 shows water adsorption isotherms

for mmen-Mg_2(dobpdc) (left) and mmen-Mn_2(dobpdc)(right) at 25 °C for different conditions of relative humidity. Mmen-Mg_2(dobpdc) showed two distinct (high and low) regions of water adsorption. Water adsorption was found to be reversible with a small hysteresis over this material. However, similar reversibility in water adsorption was not observed with mmen-Mn_2(dobpdc). This suggests reduced stability of the Mn-based MOF, as discussed below.

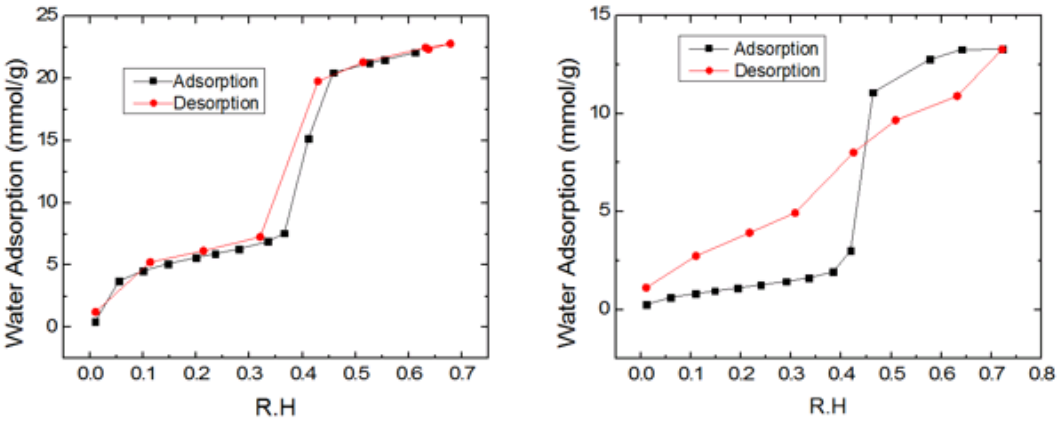

Figure 3.2 Water adsorption isotherms for mmen-Mg_2(dobpdc) (left) and mmen-Mn_2(dobpdc)(right).

Table 3.1 lists the BET surface areas of the MOFs before and after water exposure obtained without further exposing the material to external conditions. A significant loss (~83%) of BET surface area was observed for the mmen-Mn_2(dobpdc), with a 40% loss of dry CO_2 adsorption capacity. In contrast, the BET surface area for the mmen-Mg_2(dobpdc) showed only 25% loss, with only a slight decrease in the dry CO_2 adsorption capacity. Mason et.al.[48] studied multi-component CO_2 adsorption in the presence of water and observed that H_2O has no impact on the carbamate insertion mechanism leading to a negligible change in the CO_2 adsorption capacity in the presence of water.

Powder XRD (Figure B.2) patterns collected before and after water exposure showed that crystallinity was preserved for both the mmen-Mg_2(dobpdc) and mmen-Mn_2(dobpdc) materials. Loss of BET surface area with preservation of crystallinity suggests formation of random defects not observed in PXRD and/or pore blockage by rearrangement of amine groups. Similar observations have been made for Mg_2(dobdc) and HKUST-1 by Schoenecker et. al.[49] and recently for Mg_2(dobpdc) by Vitilo et al.[50] While a more detailed mechanistic investigation is needed to fully understand the stability of these MOFs under humid conditions, these initial data support our successful development of a Mg_2(dobpdc) film on a cordierite monolith washcoated with α-alumina for gas adsorption applications.

Table 3.1. CO_2 Adsorption and BET surface area of mmen-Mg_2(dobpdc) and mmen-Mn_2(dobpdc) before and after exposure to water.

	mmen-Mg_2(dobpdc)		mmen-Mn_2(dobpdc)	
	Before H_2O exposure	After H_2O exposure	Before H_2O exposure	After H_2O exposure
CO_2 adsorption at 10% CO_2 in helium (mmol/g)	3.33 mmol/g	3.27 mmol/g	3 mmol/g	1.8 mmol/g
BET surface area (m^2/g)	894	645	794	134

3.3.2 Scale up of Mg_2(dobpdc) synthesis

It has been shown that rapid MOF synthesis can be achieved by tuning the etching/dissolution of metal precursors using appropriate solvents,[51] the concentration of ligand, or the size of the metal precursors.[46,52] Maserati et al.[46] used MgO nanoparticles

along with a very high concentration of ligand to achieve faster MOF synthesis while reducing the synthesis time from 12 h to 10 min. Their recipe used a relatively high concentration of ligand (0.5 M) in a very small DMF volume (0.2 mL) to achieve an ultra-fast synthesis of Mg_2(dobpdc). In many MOF syntheses, it is often necessary to use a large amount of reactants and solvent volume. Such high concentrations of the ligand can be impractical, leading to underutilization of ligand and a high waste of reagents. Reduced ligand concentration with a higher solvent volume is expected to reduce the MgO etching rate, yielding a subsequent increase in the reaction time. In the present study, the reaction was scaled up to 2.5-5 mL from the previously reported 0.2 mL solution of DMF with H_4(dobpdc) concentrations of 0.05 M, 0.1 M, and 0.2 M while using a fixed amount of commercial MgO nanoparticles (0.5 mmol). As shown in Figure 3.3, complete conversion of MgO to Mg_2(dobpdc) was achieved with the 0.2 M H_4(dobpdc) concentration in 18h. Complete conversion of MgO to Mg_2(dobpdc) was not achieved in 18 h for the lower concentration of H_4(dobpdc) despite an adequate ligand to metal oxide stoichiometry (0.5:1) for the complete conversion. This highlights the importance of the kinetics of the metal oxide etching step for MOF synthesis from solid precursors. Smaller metal oxide particles are expected to reduce the time of the reaction. Maserati et al.[46] also noted that creation of metal oxide nanocrystals leads to enhanced reaction rates, reducing the synthesis time.

3.3.3 Development of MOF coatings on cordierite monolith washcoated α-alumina

Creating an MOF film for practical applications on a structured substrate such as a cordierite monolith has multiple challenges. The choice of MOF precursors, drying

technique, solvents for synthesis, surface pretreatments and MOF synthesis parameters (temperature, time, etc.) all play an important role in creating a uniform and strongly bound film to the substrate.

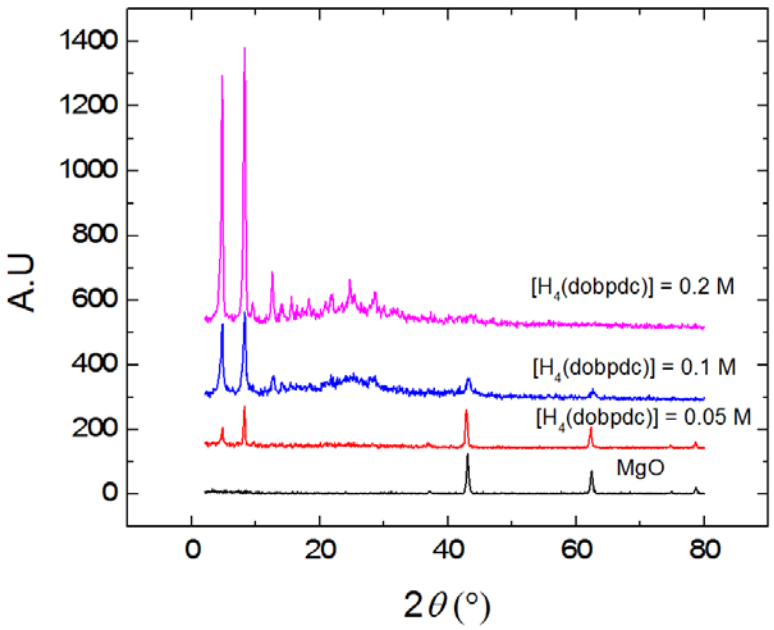

Figure 3.3. XRD characterization of Mg_2(dobpdc) synthesis scale up. As the ligand concentration is increased, the MgO peaks (2θ = 37^0,$44^0$and 63^0) decrease and the MOF peaks (2θ = 4.6^0,8.1^0) increase *in* intensity with a complete conversion for the 0.2 M ligand concentration.

Cordierite wash-coated with α-alumina was chosen for Mg_2(dobpdc) growth. The presence of α-alumina is expected to help anchor Mg_2(dobpdc) on the monolith surface through the interaction of OH^- groups of α--alumina with $COOH^-$ groups of the H_4(dobpdc) ligand in the MOF. Additionally, Perez-Cadenas[53] demonstrated the use α-alumina to eliminate transport limitations by blocking macro-pores present in cordierite monolith walls.

McDonald et al.[8,15] used halide and nitrate salts as MOF precursors in their early work on mmen-Mg_2(dopbpdc) powder syntheses. Following their procedure, in our first study, activated monoliths were dipped in the hydrothermal synthesis solution and deposition on the monolith surface was achieved. As shown in Figure B.3, a thick, non-uniform deposition was observed on the monolith surface. However, the major disadvantages of this method are the primary homogeneous nucleation pathway in solution and the concomitant poor adhesion of the deposited MOF film on the monolith surface. Poor adhesion of the MOF film led to the film flaking off the monolith surface when heating during the activation step required for functionalization of the MOF film with amines.

In addition to the creation of a uniform and strong coating, the orientation of the MOF crystals is also important for MOFs such as Mg_2(dobpdc) (Figure 3.4) with needle shaped crystals and one-dimensional pores. If the one-dimensional pores of the material are not aligned correctly, the MOF crystals will not be as effective for the gas separation due to the potential inaccessibility of the pore mouths.

To achieve uniform growth and suitable orientation of MOF crystals, we explored the use of solid MOF precursors acting as the seed for further MOF synthesis. Use of sparingly soluble solid precursors is a relatively new approach in MOF synthesis, with the advantage that it avoids potentially unstable nitrate and corrosive halide salt precursors.[54] Also, a higher density of metal cations can be achieved on the surface to produce a dense growth of MOF. This is because MgO has a higher percentage of Mg compared to $Mg(NO_3)_2$,$6H_2O$, leading to reduced precursor use per gram of MOF. To this end, we

explored changing MOF precursors from nitrate and halide salts to MgO nanopowders. Here we aimed to create a uniform seed layer of MgO on the monolith surface.

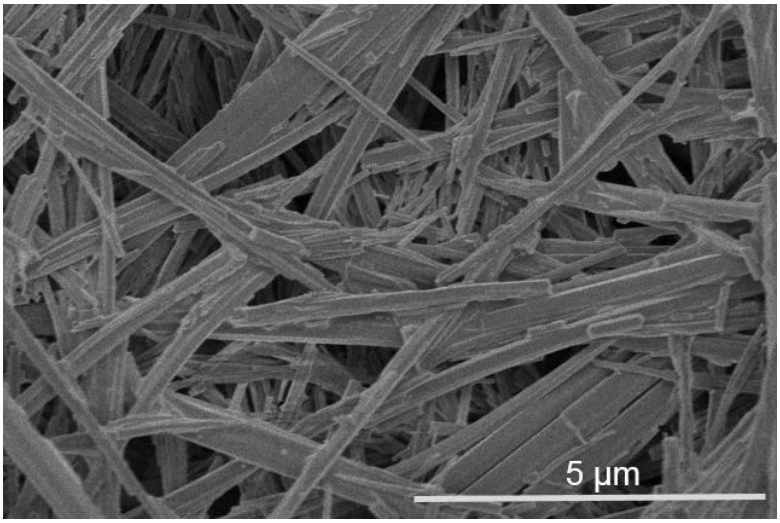

Figure 3.4 Typical SEM of needle shaped crystals of Mg_2(dobpdc).

While there are many ways to control the orientation of MOF crystals, approaches previously described in the zeolite literature have been the most widely used. One approach proposed by Van der Drift called evolutionary selection was used by Bonilla et al.[55] to simulate the growth of oriented MFI zeolite films on an inert substrate. They hypothesized that in a polycrystalline film, crystals with a rapid growth perpendicular to the substrate will survive whereas all other crystals orientations will be buried because of the intergrowth. As shown in Figure 3.5, we extend this approach to Mg_2(dobpdc) film growth with the hypothesis that by using a relatively high concentration of ligand to facilitate rapid growth, the MOF orientation may be suitably controlled.

There are many methods of creating oxide coatings on monoliths.[56] In our initial attempt, following a modified procedure used by Fernandez et al.[36] for the creation of an alumina washcoat on a cordierite monolith, a colloidal dispersion of MgO was made in water and the pH was adjusted to 7.

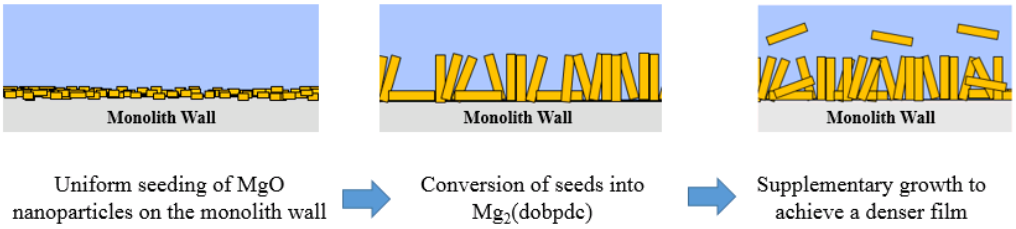

Figure 3.5 Revised approach to create MOF films on the monolith substrate employing MgO seeding, conversion of seeds to MOF crystallites, and supplementary growth to create a dense array of MOF crystals with good exposure of MOF pore mouths.

An activated cordierite monolith washcoated with α-alumina with was then dipped in the slurry a few times before drying in an oven at 100 °C. In this case, a uniform deposition of MgO was not achieved and the MgO (Figure B.4, left) coating mainly settled at the bottom of monolith because of gravity during drying. Vergunst et al.[57] studied different drying techniques for monoliths impregnated with metal precursors and their effects on the distribution of metal precursors in the monolith. They suggested rapid drying techniques such as microwave drying or immobilization techniques such as freeze drying were effective in achieving a uniform distribution of metal precursor on the monolith. In the absence of rapid drying/immobilization, they observed that the metal precursor solution tended to settle because of gravity and a uniform distribution was not achieved. Freeze-drying (Figure B.4, right) of the MgO slurry on the monolith avoided the settling of MgO but poor adhesion to the monolith surface was still observed. Next, a modified procedure[38]

from the Caro group was employed where methanol was used instead of water to achieve rapid drying and PEI-25000 was used to try to improve the adhesion of the MgO nanoparticles to the monolith. This approach proved successful, as described below. Scanning electron microscopy images of materials resulting from different stages of Mg_2(dobpdc) synthesis on the monolith are shown in Figure 3.6. a and Figure 3.6. c show the bare 100 CPSI cordierite surface washcoated with α-alumina. The uniform coating of MgO on the monolith substrate is shown in Figures 3.6b and 3.6d, as obtained following dip coating in an MgO slurry in methanol followed by rapid drying of the methanol from the monolith surface in an oven maintained at 70 °C. Exposed macropores are also blocked by MgO.

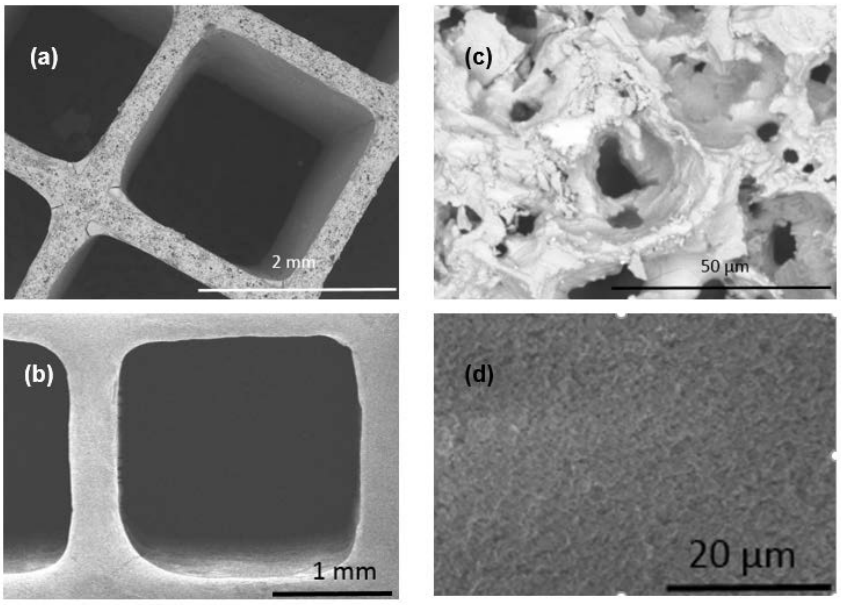

Figure 3.6 Development stages of the MgO film on the monolith substrate; low and high resolution SEM images of the bare monolith (a,c), low and high resolution images of the MgO coating on the monolith surface (b,d).

The MgO seeds were then converted into Mg_2(dobpdc) using a scaled up recipe with 0.2 M and 0.1 M ligand concentration. As shown in Figure 3.7, a dense and vertically oriented growth of Mg_2(dobpdc) was achieved. A crystal length of more than 50 µm was achieved, which is very large for Mg_2 (dobpdc) crystals. With less than 1 µm crystal width, it also indicates a high aspect ratio. Unfortunately, poor adhesion of the MOF film to the surface can be seen, indicating only a partial success for this approach.

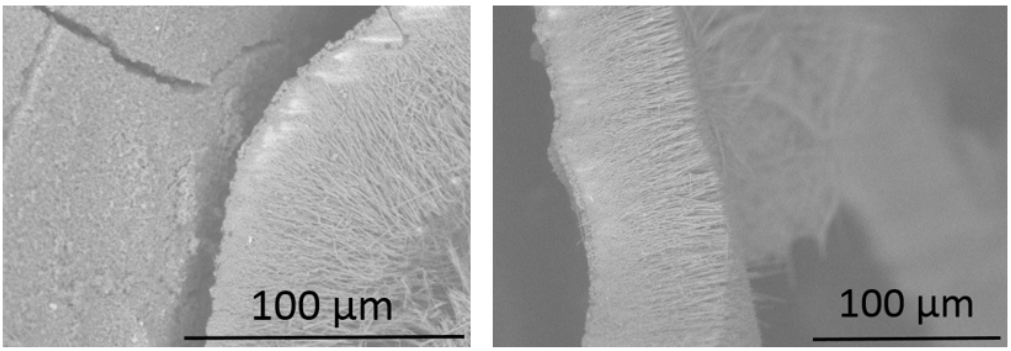

Figure 3.7. SEM images of dense and vertically oriented growth of Mg_2(dobpdc) (right) with areas of film delamination from the substrate (left).

We hypothesize that complete conversion of MgO to Mg_2(dobpdc) actually weakens the adhesion of the film and there is a limit on the maximum possible metal precursor conversion that can be achieved without compromising the mechanical and thermal stability of the film. That is, the presence of at least some MgO appears to be essential to maintain good thermal and mechanical stability in the film. To this end, primary MOF film growth was achieved with 0.05 M ligand concentration. An outward crystal orientation and uniform distribution of the MOF film were observed, as shown in Figure 3.8a and Figure 3.8c. Further Mg_2(dobpdc) growth (Figure 3.8b and Figure 3.8d) without affecting the orientation was achieved through supplementary growth by hydrothermal

synthesis[15] using a lower concentration of H_4(dobpdc) ligand (0.03 M) and $Mg(NO_3)_2$ (0.06 M) to limit additional homogeneous nucleation. This approach results in coatings with uniform coverage of the substrate and good thermal and mechanical stability, as the MOF film is free of cracks and provides stable cyclic CO_2 adsorption, as discussed below.

The MgO and Mg_2(dobpdc) loadings achieved on the monolith were 8-10% and 14-18% by weight. It should be noted that the weight loading is a strong function of the available geometric surface area of the monolith. While the present studies are performed on a 100 CPSI monolith, we expect that difference in dimensions of the monolith channel (~ 100s μm) compared to MgO nanoparticles (~50 nm) can be further utilized to grow the film on 400 or 600 CPSI monoliths, leading to 2-3 times higher weight loading associated with their higher geometric surface area.[29] Further optimization can also be achieved in the soak time, drying time, and number of cycles leading to different MgO loadings on the monolith. However, these cases will also require different reaction conditions for the MgO to Mg_2(dobpdc) transformation because of a different rate of MgO etching.

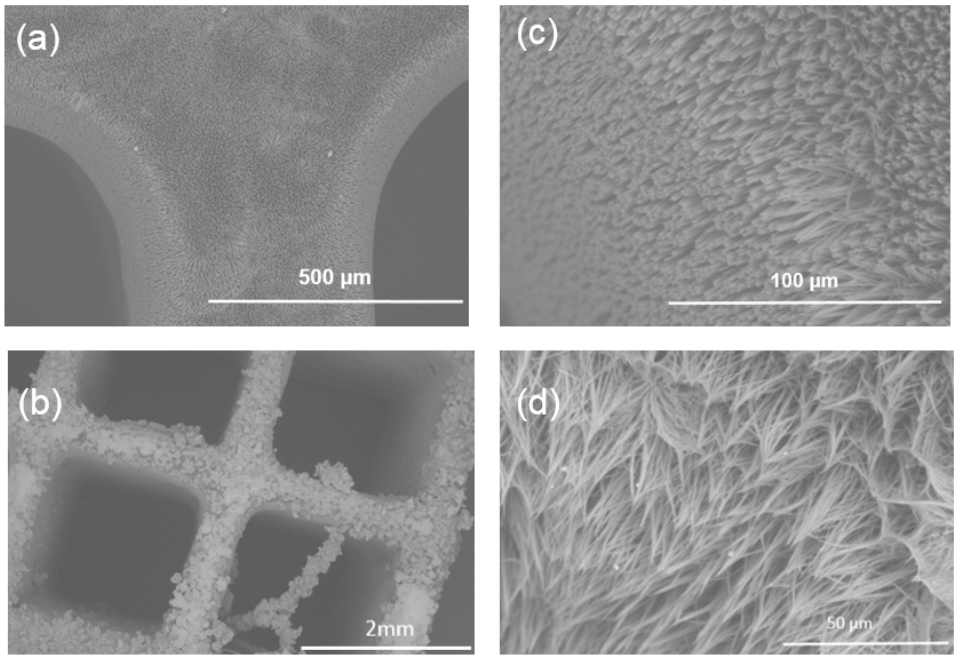

Figure 3.8 Development stages of the MOF film on the monolith substrate; low and high resolution SEM images of the resulting oriented growth of Mg_2(dobpdc) crystals on the monolith surface (a,c), and low and high resolution images of the thicker films resulting from supplementary growth (b,d).

The approach described above was able to effectively grow Mg_2(dobpdc) films on the 100 CPSI cordierite monolith washcoated with α-alumina. Figure 3.9 shows nitrogen physisorption isotherms for the bare monolith (black), and Mg_2(dobpdc) film grown on the monolith (blue). The nitrogen uptakes for the Mg_2(dobpdc) on the monolith and the mmen-Mg_2(dobpdc) powder are reported on per g MOF basis. The bare monolith showed negligible microporosity (BET surface area ~ 10 m^2/g) and significant hysteresis, indicative of macroporosity (black curve). After growth of the MOF film on the monolith, significant microporosity was observed and the N_2 physisorption of the Mg_2(dobpdc) on the monolith (blue curve) showed the type I curve with characteristic shoulder at low P/P_0 for Mg_2(dobpdc). The uptake by N_2 physisorption at $P/P_0 = 0.6$ is 58.5% of Mg_2(dobpdc) in powder form (red curve). Further comparison with Maserati et al.[46] (80.4%), McDonald

et al.[8] (68.4%) and Vitillo et al.[50] (57.9%) highlights the variation in N_2 physisorption uptakes arising from textural differences in the material because of different crystal sizes as well as partial conversion of MgO to Mg_2(dobpdc). Hysteresis associated with macroporosity in the monolith at high pressures was also preserved.

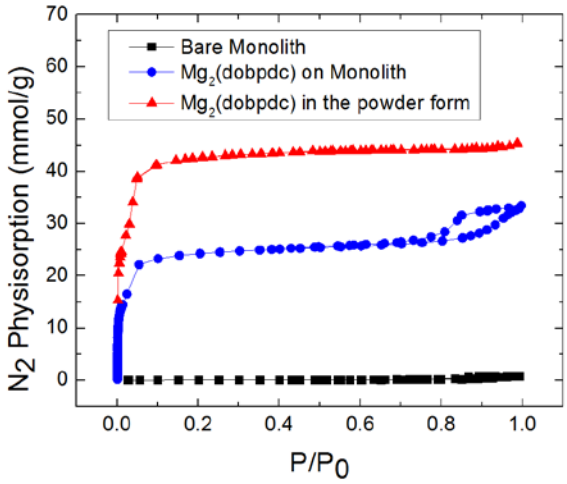

Figure 3.9 N_2 physisorption isotherms for the bare monolith (black) and the Mg_2(dobpdc) MOF on the monolith substrate (blue). The data for the MOF film are reported on a per g Mg_2(dobpdc) basis.

To establish the presence of a crystalline MOF, a film of Mg_2(dobpdc) was also developed on a flat α-alumina plate. In a manner similar to that described above, a layer of MgO was created on the flat surface and MOF was subsequently grown following similar conditions for the film development on the monolith. As shown on Figure 3.10, in the blue curve, distinct (1 0 0) and (1 1 0) MOF peaks can be observed at 2θ values of 4.6° and 8.1° after seeding and supplemental growth. However, no conclusion can be drawn for preferred orientation in the l direction due to the absence of the l index in prominent peaks. The peaks after 2θ ~ 25° are attributed to α-alumina and MgO. The presence of MgO corresponding to 2θ peaks at ~ 37° and 44° is also observed.

EDX measurements were performed to assess the surface composition of the MgO and Mg_2(dobpdc) film after functionalization with MMEN. As shown in Figure 3.11 and Figure B.5, the surface is mainly composed of Mg (59.7 wt%) and O (39.7 wt%), with this surface composition supporting the presence of MgO species on the surface.

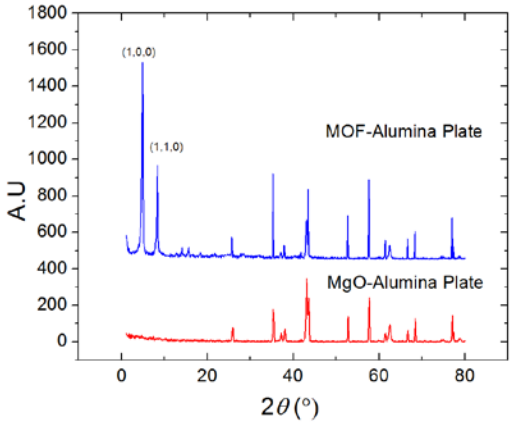

Figure 3.10. X-ray diffraction patterns of MgO and Mg_2(dobpdc) films on an α–alumina plate substrate.

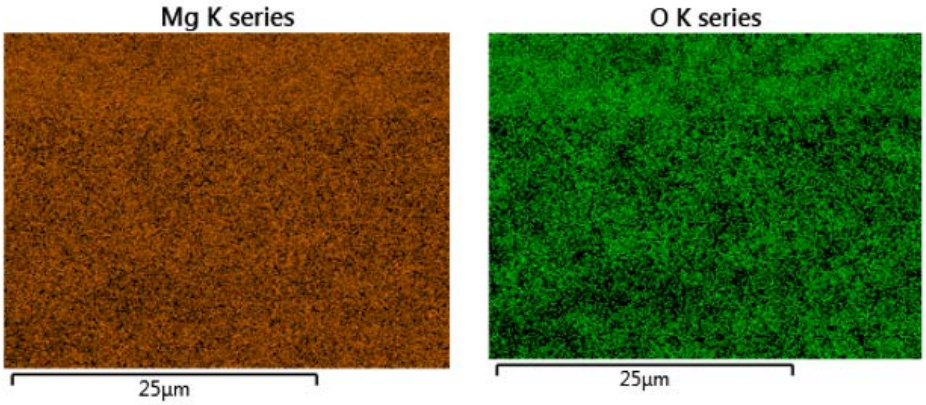

Figure 3.11. Surface composition of the MgO film on the monolith surface. The surface mainly consists of Mg (brown, left) and O (green, right).

After the conversion to Mg_2(dobpdc) and functionalization with mmen, the surface composition (Figure 3.12, Figure B.6) changed to include C (55.9 wt%) and N (10.2 wt %), with percentages in close proximity to the expected values of C (53.37 wt%) and N

(11.32 wt%) from prior work by McDonald et al.[8] Also, it is noteworthy that a uniform distribution of C, Mg, N is observed across the surface.

The CO_2 adsorption behavior of the materials was measured using 10% CO_2 in helium as well as 100% CO_2 on a piece of a monolith using a TGA. Figure 3.13 demonstrates the CO_2 adsorption capacity of the monolith supported mmen-Mg_2(dobpdc) on a per g MOF basis. A CO_2 uptake of 2.37 mmol/g is observed at 10 % CO_2 concentration in helium and 2.88 mmol/g using pure CO_2.

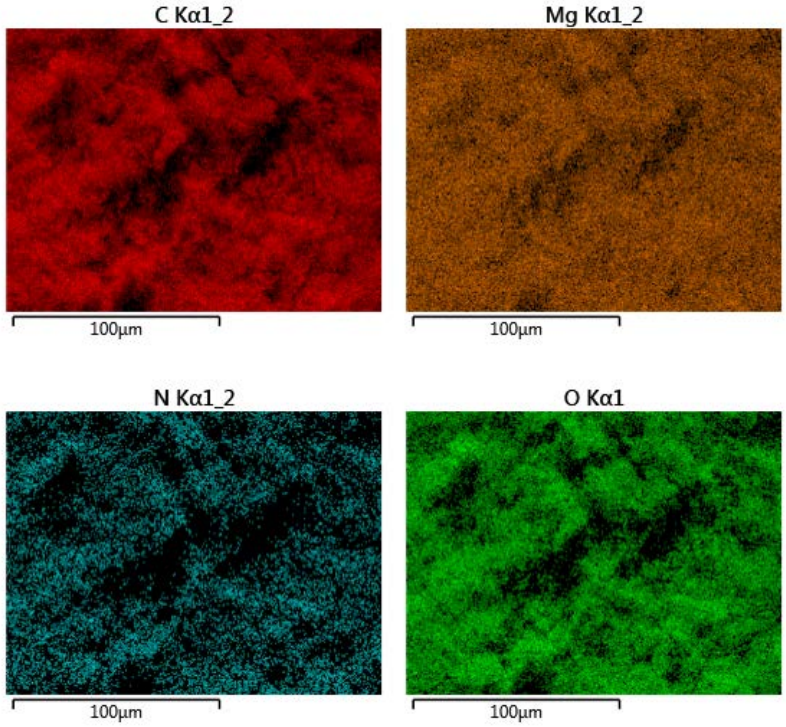

Figure 3.12. Surface composition for mmen-Mg_2(dobpdc) on a cordierite monolith wash coated with α-alumina. The surface mainly consists of C (red), Mg (brown), N (blue) and O (green).

The adsorption at 10% CO_2 concentration by mmen-Mg_2(dobpdc) in the film form is ~70% of adsorption uptakes for mmen-Mg_2(dobpdc) in powder form. A typical adsorption-desorption cycle for a piece of MOF-monolith is shown in Figure B.7. The material also showed excellent cyclic stability for the limited number of cycles employed here. To the best of our knowledge, this is the first evidence of the adsorption of CO_2 from a dilute gas mixture using a monolith-supported amine-functionalized MOF system.

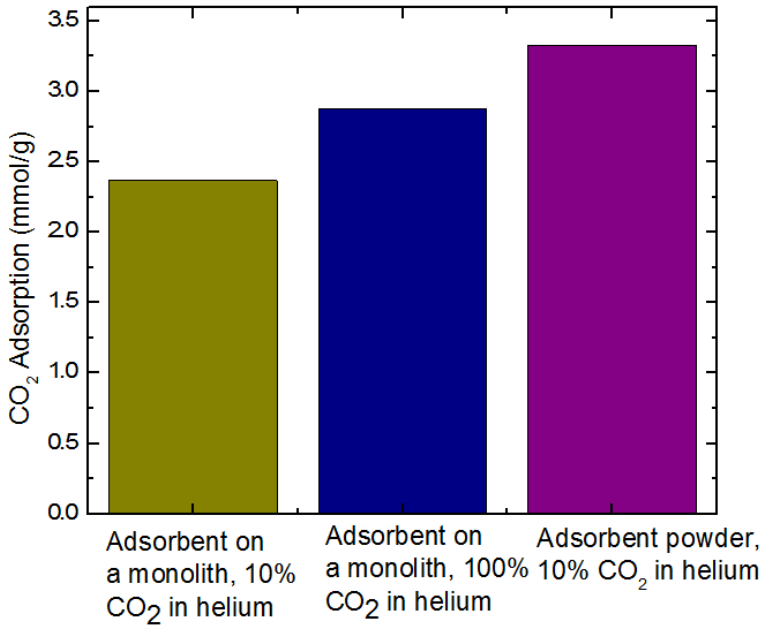

Figure 3.13 CO_2 adsorption studies for mmen-Mg_2(dobpdc) on monolith with 10% CO_2 in helium (green) and 100% CO_2 (dark blue) measured gravimetrically. CO_2 adsorption with 10% CO_2 in helium measured gravimetrically for mmen-Mg_2(dobpdc) in the powder form (purple) is also shown for the comparison.

3.4 Conclusions

Mg_2(dobpdc) and Mn_2(dobpdc) functionalized with N-N' dimethyl ethylene diamine (mmen) have shown significant potential for CO_2 capture from dilute gas mixtures. In this work, the stability of mmen-Mg_2(dobpdc) and mmen-Mn_2(dobpdc) under humid

conditions was analyzed through bulk characterization techniques such as N_2 physisorption and adsorption at 10% CO_2 concentration in helium before and after the humid exposure. Results indicated a superior stability of mmen-Mg_2(dobpdc). Subsequently, the Mg_2(dobpdc) synthesis was further scaled up and a recipe was developed to create a robust Mg_2(dobpdc) film on a 100 CPSI cordierite honeycomb monolith washcoated with α-alumina. An outward orientation of Mg_2(dobpdc) crystals was achieved in the film. CO_2 adsorption over multiple cycles demonstrated high capacities with a stable performance. To our knowledge, this is the first report of amine functionalized Mg_2(dobpdc) on an inorganic substrate such as a honeycomb monolith, making an important step toward the scalable use of Mg_2(dobpdc) in practical gas separation applications.

3.5 References

1. Bollini, P.; Didas, S. A.; Jones, C. W. Amine-Oxide Hybrid Materials for Acid Gas Separations. *J. Mater. Chem.* **2011**, 21, 15100–15120.

2. Belmabkhout, Y.; Serna-Guerrero, R.; Sayari, A. Amine-Bearing Mesoporous Silica for CO_2 Removal from Dry and Humid Air. *Chem. Eng. Sci.* **2010**, 65, 3695–3698.

3. Yue, M. B.; Chun, Y.; Cao, Y.; Dong, X.; Zhu, J. H. CO_2 Capture by As-Prepared SBA-15 with an Occluded Organic Template. *Adv. Funct. Mater.* **2006**, 16, 1717–1722.

4. Chaikittisilp, W.; Kim, H.-J.; Jones, C. W. Mesoporous Alumina-Supported Amines as Potential Steam-Stable Adsorbents for Capturing CO_2 from Simulated Flue Gas and Ambient Air. *Energy & Fuels* **2011**, 25, 5528–5537.

5. Wang, J.; Wang, M.; Zhao, B.; Qiao, W.; Long, D.; Ling, L. Mesoporous Carbon-Supported Solid Amine Sorbents for Low-Temperature Carbon Dioxide Capture. *Ind. Eng. Chem. Res.* **2013**, 52, 5437–5444.

6. Drage, T. C.; Arenillas, A.; Smith, K. M.; Snape, C. E. Thermal Stability of Polyethylenimine Based Carbon Dioxide Adsorbents and Its Influence on Selection of Regeneration Strategies. *Microporous Mesoporous Mater.* **2008**, 116, 504–512.

7. Darunte, L. A.; Walton, K. S.; Sholl, D. S.; Jones, C. W. CO_2 Capture via Adsorption in Amine-Functionalized Sorbents. *Curr. Opin. Chem. Eng.* 2016, 12, 82–90.

8. McDonald, T. M.; Lee, W. R.; Mason, J. A.; Wiers, B. M.; Hong, C. S.; Long, J. R. Capture of Carbon Dioxide from Air and Flue Gas in the Alkylamine-Appended Metal–Organic Framework Mmen-Mg_2(dobpdc). *J. Am. Chem. Soc.* **2012**, 134, 7056–7065.

9. Choi, S.; Watanabe, T.; Bae, T.-H.; Sholl, D. S.; Jones, C. W. Modification of the Mg/DOBDC MOF with Amines to Enhance CO_2 Adsorption from Ultradilute Gases. *J. Phys. Chem. Lett.* **2012**, 3, 1136–1141.

10. Keskin, S.; van Heest, T. M.; Sholl, D. S. Can Metal–Organic Framework Materials Play a Useful Role in Large-Scale Carbon Dioxide Separations? *ChemSusChem* **2010**, 3, 879–891.

11. Sumida, K.; Rogow, D. L.; Mason, J. a; McDonald, T. M.; Bloch, E. D.; Herm, Z. R.; Bae, T.-H.; Long, J. R. Carbon Dioxide Capture in Metal-Organic Frameworks. *Chem. Rev.* **2012**, 112, 724–781.

12. Hu, Y.; Verdegaal, W. M.; Yu, S.-H.; Jiang, H.-L. Alkylamine-Tethered Stable Metal-Organic Framework for CO_2 Capture from Flue Gas. *ChemSusChem* **2014**, 7, 734–737.

13. Lin, Y.; Lin, H.; Wang, H.; Suo, Y.; Li, B.; Kong, C.; Chen, L. Enhanced Selective CO_2 adsorption on polyamine/MIL-101(Cr) Composites. *J. Mater. Chem. A* **2014**, 2, 14658.

14. Darunte, L. A.; Oetomo, A. D.; Walton, K. S.; Sholl, D. S.; Jones, C. W. Direct Air Capture of CO_2 Using Amine Functionalized MIL-101(Cr). *ACS Sustainable Chem. Eng.* **2016**, 4, 5761–5768.

15. Mcdonald, T. M.; Mason, J. A.; Kong, X.; Bloch, E. D.; Gygi, D.; Dani, A.; Crocellà, V.; Giordanino, F.; Odoh, S. O.; Drisdell, W. S.; Vlaisavljevich, B.; Dzubak, A. L.; Poloni, R.; Schnell, S. K.; Planas, N.; Lee, K.; Pascal, T.; Wan, L. F.; Prendergast, D.; Neaton, J. B.; Smit, B.; Kortright, J. B.; Gagliardi, L.; Bordiga, S.; Reimer, J. A.; Long, J. R. Cooperative Insertion of CO_2 in Diamine- Appended Metal-Organic Frameworks. *Nature* **2015,** 519, 303–308

16. Hefti, M.; Joss, L.; Bjelobrk, Z.; Mazzotti, M. On the Potential of Phase-Change Adsorbents for CO_2 Capture by Temperature Swing Adsorption. *Faraday Discuss*. **2016**, 192, 153–179.

17. Choi, S.; Drese, J. H.; Eisenberger, P. M.; Jones, C. W. Application of Amine-Tethered Solid Sorbents for Direct CO_2 Capture from the Ambient Air. *Environ. Sci. Technol.* **2011**, 45, 2420–2427.

18. Sanz-Pérez, E. S.; Murdock, C. R.; Didas, S. A.; Jones, C. W. Direct Capture of CO_2 from Ambient Air. *Chem. Rev.* **2016**, 116, 11840–11876.

19. Zhang, W.; Liu, H.; Sun, C.; Drage, T. C.; Snape, C. E. Capturing CO_2 from Ambient Air Using a Polyethyleneimine–silica Adsorbent in Fluidized Beds. *Chem. Eng. Sci.* **2014**, 116, 306–316.

20. Veneman, R.; Li, Z. S.; Hogendoorn, J. A.; Kersten, S. R. A.; Brilman, D. W. F. Continuous CO_2 Capture in a Circulating Fluidized Bed Using Supported Amine Sorbents. *Chem. Eng. J.* **2012**, 207–208, 18–26.

21. Lively, R. P.; Chance, R. R.; Kelley, B. T.; Deckman, H. W.; Drese, J. H.; Jones, C. W.; Koros, W. J. Hollow Fiber Adsorbents for CO_2 Removal from Flue Gas. *Ind. Eng. Chem. Res.* **2009**, 48, 7314–7324.

22. Vu, D. Q.; Koros, W. J.; Miller, S. J. High Pressure CO_2/CH_4 Separation Using Carbon Molecular Sieve Hollow Fiber Membranes. *Ind. Eng. Chem. Res*. **2002**, 41, 367–380.

23. Ribeiro, R. P.; Sauer, T. P.; Lopes, F. V; Moreira, R. F.; Grande, C. A.; Rodrigues, A. E. Adsorption of CO_2, CH_4, and N_2 in Activated Carbon Honeycomb Monolith. *J. Chem. Eng. Data* **2008**, 53, 2311–2317.

24. Rezaei, F.; Mosca, A.; Webley, P.; Hedlund, J.; Xiao, P. Comparison of Traditional and Structured Adsorbents for CO_2 Separation by Vacuum-Swing Adsorption. *Ind. Eng. Chem. Res.* **2010**, 49, 4832–4841.

25. Rezaei, F.; Webley, P. Optimum Structured Adsorbents for Gas Separation Processes. *Chem. Eng. Sci.* **2009**, 64, 5182–5191.

26. Eisenberger, P. Carbon Dioxide Capture/regeneration Aparatus. US 8696801 B2, 2014.

27. Sakwa-Novak, M. A.; Yoo, C.-J.; Tan, S.; Rashidi, F.; Jones, C. W. Poly(ethylenimine)-Functionalized Monolithic Alumina Honeycomb Adsorbents for CO_2 Capture from Air. *ChemSusChem* **2016**, 9, 1859–1868.

28. Tarka, T. J.; Ciferno, J. P.; Gray, M. L.; Fauth, D. CO_2 capture systems using amine enhanced solid sorbents. Presented at the Fifth Annual Conference on Carbon Capture & Sequestration, Alexandria, VA, USA, May 8-11, **2006**; Paper No. 152, 30 pp. (Available via the Internet at http://www.netl.doe.gov/publications/proceedings/06/carbon-seq/Tech%20Session%20152.pdf.)

29. Heck, R. M.; Gulati, S.; Farrauto, R. J. The Application of Monoliths for Gas Phase Catalytic Reactions. *Chem. Eng. J.* **200**1, 82, 149–156.

30. Kulkarni, A. R.; Sholl, D. S. Analysis of Equilibrium-Based TSA Processes for Direct Capture of CO_2 from Air. *Ind. Eng. Chem. Res.* **2012**, 51, 8631–8645.

31. Sinha, A.; Darunte, L. A.; Jones, C. W.; Realff, M. J.; Kawajiri, Y. Systems Design and Economic Analysis of Direct Air Capture of CO_2 through Temperature Vacuum Swing Adsorption . *Ind. Eng. Chem.*Res. **2017**, 56, pp 750–764.

32. Zamaro, J. M.; Ulla, M. A.; Miró, E. E. Zeolite Washcoating onto Cordierite Honeycomb Reactors for Environmental Applications. *Chem. Eng. J.* **2005**, 106, 25–33.

33. Öhrman, O.; Hedlund, J.; Sterte, J. Synthesis and Evaluation of ZSM-5 Films on Cordierite Monoliths. *Appl. Catal., A.* **2004**, 270, 193–199.

34. Denny Jr, M. S.; Moreton, J. C.; Benz, L.; Cohen, S. M. Metal–organic Frameworks for Membrane-Based Separations. *Nat. Rev. Mater.* **2016**, 1, 16078.

35. Shekhah, O.; Liu, J.; Fischer, R. A.; Woll, C. MOF Thin Films: Existing and Future Applications. *Chem. Soc. Rev.* **2011**, 40, 1081–1106.

36. Ramos-Fernandez, E. V; Garcia-Domingos, M.; Juan-Alcañiz, J.; Gascon, J.; Kapteijn, F. MOFs Meet Monoliths: Hierarchical Structuring Metal Organic Framework Catalysts. *Appl. Catal., A* **2011**, 391, 261–267.

37. Jiang, D.; Burrows, A. D.; Edler, K. J. Size-Controlled Synthesis of MIL-101(Cr) Nanoparticles with Enhanced Selectivity for CO_2 over N_2. *CrystEngComm* **2011**, 13, 6916.

38. Wang, N.; Mundstock, A.; Liu, Y.; Huang, A.; Caro, J. Amine-Modified Mg-MOF-74/CPO-27-Mg Membrane with Enhanced H_2/CO_2 Separation. *Chem. Eng. Sci.* **2015**, 124, 27–36.

39. Betard, A.; Zacher, D.; Fischer, R. A. Dense and Homogeneous Coatings of CPO-27-M Type Metal-Organic Frameworks on Alumina Substrates. *CrystEngComm* **2010**, 12, 3768–3772.

40. Caskey, S. R.; Wong-Foy, A. G.; Matzger, A. J. Dramatic Tuning of Carbon Dioxide Uptake via Metal Substitution in a Coordination Polymer with Cylindrical Pores. *J. Am. Chem. Soc.* **2008**, 130, 10870–10871.

41. Britt, D.; Furukawa, H.; Wang, B.; Glover, T. G.; Yaghi, O. M. Highly Efficient Separation of Carbon Dioxide by a Metal-Organic Framework Replete with Open Metal Sites. *Proc. Natl. Acad. Sci. U. S. A.* **2009**, 106, 20637–20640.

42. Lee, D.-J.; Li, Q.; Kim, H.; Lee, K. Preparation of Ni-MOF-74 Membrane for CO_2 Separation by Layer-by-Layer Seeding Technique. *Microporous Mesoporous Mater.* **2012**, 163, 169–177.

43. Rezaei, F.; Lawson, S.; Hosseini, H.; Thakkar, H.; Hajari, A.; Monjezi, S.; Rownaghi, A. A. MOF-74 and UTSA-16 Film Growth on Monolithic Structures and Their CO_2 Adsorption Performance. *Chem. Eng. J.* **2017**, 313, 1346-1353

44. Kizzie, A. C.; Wong-Foy, A. G.; Matzger, A. J. Effect of Humidity on the Performance of Microporous Coordination Polymers as Adsorbents for CO_2 Capture. *Langmuir* **2011**, 27, 6368–6373.

45. Andirova, D.; Lei, Y.; Zhao, X.; Choi, S. Functionalization of Metal-Organic Frameworks for Enhanced Stability under Humid Carbon Dioxide Capture Conditions. *ChemSusChem* **2015**, 8, 3405–3409.

46. Maserati, L.; Meckler, S. M.; Li, C.; Helms, B. A. Minute-MOFs: Ultrafast Synthesis of M_2(dobpdc) Metal–Organic Frameworks from Divalent Metal Oxide Colloidal Nanocrystals. *Chem. Mater.* **2016**, 28, 1581–1588.

47. Walton, K. S.; Snurr, R. Q. Applicability of the BET Method for Determining Surface Areas of Microporous Metal−Organic Frameworks. *J. Am. Chem. Soc.* **2007**, 129, 8552–8556.

48. Mason, J. A.; McDonald, T. M.; Bae, T. H.; Bachman, J. E.; Sumida, K.; Dutton, J. J.; Kaye, S. S.; Long, J. R. Application of a High-Throughput Analyzer in Evaluating Solid Adsorbents for Post-Combustion Carbon Capture via Multicomponent Adsorption of CO_2, N_2, and H_2O. *J. Am. Chem. Soc.* **2015**, 137, 4787–4803.

49. Schoenecker, P. M.; Carson, C. G.; Jasuja, H.; Flemming, C. J. J.; Walton, K. S. Effect of Water Adsorption on Retention of Structure and Surface Area of Metal–Organic Frameworks. *Ind. Eng. Chem. Res.* ***2012***, 51, 6513–6519.

50. Vitillo, J. G.; Bordiga, S. Increasing the Stability of Mg_2(dobpdc) Metal–organic Framework in Air through Solvent Removal. *Mater. Chem. Front.* ***2017***, 1, 444-448.

51. Meckler, S. M.; Li, C.; Queen, W. L.; Williams, T. E.; Long, J. R.; Buonsanti, R.; Milliron, D. J.; Helms, B. A. Sub-Micron Polymer–Zeolitic Imidazolate Framework Layered Hybrids via Controlled Chemical Transformation of Naked ZnO Nanocrystal Films. *Chem. Mater.* ***2015***, 27, 7673–7679.

52. Guo, Y.; Mao, Y.; Hu, P.; Ying, Y.; Peng, X. Self–confined Synthesis of HKUST-1 Membranes from CuO Nanosheets at Room Temperature. *ChemistrySelect* ***2016***, 1, 108–113.

53. Pérez-Cadenas, A. F.; Kapteijn, F.; Moulijn, J. A. Tuning the Morphology of Monolith Coatings. *Appl. Catal., A* ***2007***, 319, 267–271.

54. Zhan, G.; Zeng, H. C. Alternative Synthetic Approaches for Metal–organic Frameworks: Transformation from Solid Matters. *Chem. Commun.* ***2017***, 53, 72-81 .

55. Bonilla, G.; Vlachos, D. G.; Tsapatsis, M. Simulations and Experiments on the Growth and Microstructure of Zeolite MFI Films and Membranes Made by Secondary Growth. *Microporous Mesoporous Mater.* ***2001***, 42, 191–203.

56. Nijhuis, T. A.; Beers, A. E. W.; Vergunst, T.; Hoek, I.; Kapteijn, F.; Moulijn, J. A. Preparation of Monolithic Catalysts. *Catal. Rev.* ***2001***, 43, 345–380.

57. Vergunst, T.; Kapteijn, F.; Moulijn, J. A. Monolithic Catalysts — Non-Uniform Active Phase Distribution by Impregnation. *Appl. Catal., A gen.****2001***, 213, 179–187.

TOC Graphic

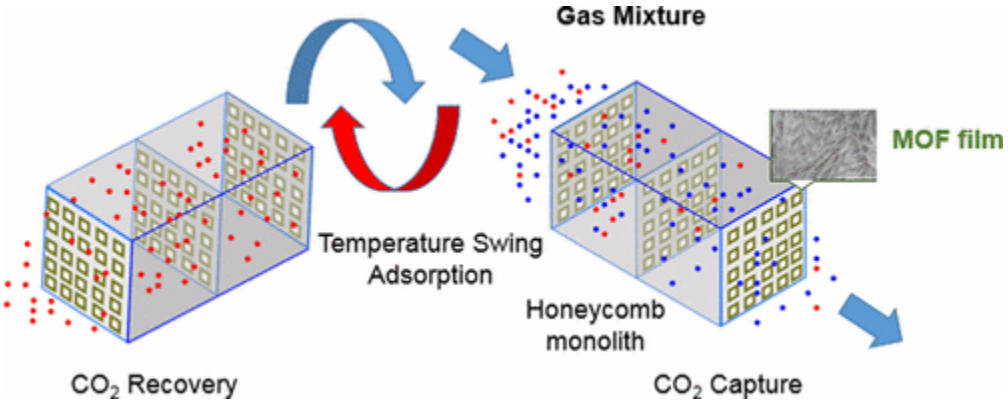
Gas Mixture
MOF film
Temperature Swing
Adsorption
Honeycomb
monolith
CO_2 Recovery
CO_2 Capture

4 SYNTHESIS OF Mg-MOF-74 ON A HONEYCOMB MONOLITH: TOWARDS SCALABLE PROCESSING OF MOFS FOR CO_2 CAPTURE APPLICATION.

4.1 Introduction

With an increase in the CO_2 concentration the atmosphere and its relation to climate change there is considerable interest in developing low cost CO_2 emission reduction technologies.[1,2] Solid adsorbent-based technologies are promising because of their lower heat capacities and potentially higher CO_2 uptakes compared to aqueous amine solutions, which are the benchmark technology.[3,4] To that end, many solid adsorbents[5–7] have been explored that have a high capacity for CO_2 capture. Metal organic frameworks (MOFs) are promising materials with high tenability and their development has led to myriad novel materials explored for CO_2 capture. One of the most prominent examples is Mg-MOF-74, which has shown a very high uptake capacity of 9.4 mmol/g for CO_2 adsorption at 1 bar.[8] The high capacity of Mg-MOF-74 is associated with the presence of highly reactive open Mg metal sites. The high reactivity of these open metal sites also makes Mg-MOF-74 susceptible to degradation in presence of moisture and oxygen.[9,10] Other members of this family of MOFs with different metal centers such as Ni or Co have shown lower CO_2 uptakes and better stability than Mg-MOF-74.[11,12]

After the development of Mg-MOF-74, numerous research groups explored the application of these materials for CO_2 separations. In 2012, Choi et al.[13,14] demonstrated the functionalization of Mg-MOF-74 with ethylene diamine (ED) to improve the stability of the framework towards degradation in the presence of steam. Su et al.[15] recently studied the CO_2 adsorption behavior and water stability in tetraethylpentamine (TEPA) functionalized Mg-MOF-74. Yang at al.[16,17] demonstrated an improved stability of the framework by doping with less reactive metals such as Ni or Co. Building on the interest of this family of MOFs, Long and coworkers have developed structurally related MOFs such as Mg_2(dobpdc) functionalized with diamines,[18,19] which have shown tunable CO_2 adsorption properties as a result of the cooperative insertion of CO_2 in the framework by amines.

While most adsorption studies are done on adsorbent samples in a powder form, there are limited demonstrations of the use of these adsorbents in more scalable contactors to date. MOFs in the form of a film on a monolithic substrate can be used for a wide variety of gas separation applications. This structure allows the tuning of the pressure drop during the gas flow, heat management during adsorption, as well as other parameters, all of which can be adjusted by the choice and channel density of the substrate. Alumina, cordierite and various polymers are commonly used substrates because of their low coefficients of thermal expansion and/or cost. During a temperature swing adsorption (TSA) process, the composite system of the MOF and the substrate is heated to desorb CO_2. Typically, the energy used to heat the substrate is an energy penalty and therefore cost in the process unless it is recovered through heat integration.

There are few examples of the application of MOF-74 and related MOFs in practical, scalable supports. Bae et al.[20] developed mixed matrix membranes where they incorporated nanosized particles of MOF-74 (Mg, Ni, Zn) in glassy polymers and found that a glassy poly(imide) offered the best availability of MOF particles to sorbing CO_2. Wang et al.[21] created a membrane of amine-functionalized Mg-MOF-74 using MgO as the seed layer α-alumina for CO_2 and H_2 separation. Campbell and Tokay[22] studied the size engineering of Mg-MOF-74 towards creating a film for membrane applications. Lee et al.[23] investigated the layer by layer (LBL) approach to create a uniform film of Ni-MOF-74 on an alpha-alumina substrate. Many of these films were primarily developed for membrane-based gas separation applications for which a defect-free membrane is a key requirement. In general, the synthesis procedure involves the creation of a seed layer followed by secondary growth to achieve a defect-free film.

In adsorption based separations, the Rezaei group used a similar LBL method to grow Ni-MOF-74 on honeycomb monolithic supports[24,25] for CO_2 adsorption applications. Our recent study[26] has demonstrated an oriented development of amine-functionalized Mg_2(dobpdc) on a honeycomb monolith for CO_2 capture. Maserati et al.[27] immobilized Mg_2(dobpdc) nanorods in a mixed-matrix membrane to achieve a similar level of CO_2 adsorption as in powders. Thakkar et al.[28] reported 3-D printed Ni-MOF-74 for CO_2 capture applications. For operation with a lower energy penalty, a high loading of MOF relative to the substrate is generally desired in adsorption based gas separation applications.[29,30]

While most of the studies above were done using soluble metal salt precursors, recent reports[31–33] have studied MOF formation from solid precursors. This approach is

particularly advantageous for engineering of MOF films on surfaces or shaped MOF partciles, as many solid precursors are water stable and can be shape-engineered before conversion to MOFs. However, one challenge limiting wider deployment of solid precursors for MOF synthesis is the rate of the conversion of the solid precursor into the final MOF. Maserati et al.[33] observed that conversion from MgO to Mg_2(dobpdc) is controlled by the rate of itching of the precursor by the ligand. Our previous study[26] with Mg_2(dobpdc) synthesis using MgO as a precursor demonstrated the need for extended times for complete conversion from MgO to Mg_2(dobpdc) as the reaction was scaled up. To speed up the conversion of MgO to the MOF, it is hypothesized that the presence of solvents such as water that offer the ability for enhanced dissolution of the MgO will increase the rate of conversion. Here, we report the generality of our approach with the development of Mg-MOF-74 films supported on a monolith substrate using MgO as the precursor. We explore the effect of the presence of water in the solution on the resultant crystalline MOF structure. Following the seeding of honeycomb monoliths with MgO, the primary growth was carried out based on the optimized synthesis of Mg-MOF-74 in the powder form. Then secondary growth was used to increase the MOF loading on the monolith. The resultant structure was characterized by N_2 physisorption at 77 K and CO_2 adsorption at 25 °C for Mg-MOF-74, demonstrating the synthesis of a dense, robust and functional MOF film on the substrate.

4.2 Experimental Section

4.2.1 Material synthesis

Substrate list: Cordierite monoliths wash-coated with α-alumina with a cell density of 400 cells per square inch (CPSI) were obtained from Applied Catalysts Co. USA.

Chemicals list: MgO (nano powder size <50 nm, Sigma-Aldrich), 2,5-dihydroxyterephthalic (TCI Chemicals)), ethylene diamine (Sigma-Aldrich), dimethylformamide (BDH Chemicals, ACS grade), toluene (Sigma Aldrich, anhydrous) & methanol (BDH Chemicals, ACS grade) were used as received.

Mg-MOF-74 powder synthesis: In a 10 mL scintillation vial, 83.4 mg (0.42 mmol) of 2,5-dihydroxyterephthalic acid (H_4(dobdc)) was added to the solution of 4 mL dimethylformamide (DMF) and 1 mL of water. The mixture was sonicated until the ligand was completely dissolved. 31.5 mg (0.78 mmol) MgO was added to the solution. The reaction was carried out at 120 °C for 24 h and a dark yellow MOF-74 powder was obtained at the bottom of the vial. The solution was then allowed to cool to room temperature. The product underwent solvent exchanges at least three times with DMF and MeOH each. Each solvent exchange was carried out at 60 °C for at least 4 h.

Ethylene diamine-Mg-MOF-74 synthesis (ED-MOF-74): Mg-MOF-74 (250 mg) was activated under 10 μBar vacuum at 250 ^{0}C for 12 h. Activated MOF-74 and 3 mL of ED were added to 50 mL of anhydrous toluene in a glovebox under N_2-rich atmosphere and the grafting reaction was carried out under reflux for 12 h. The resultant dark-yellow

powder was washed with toluene and hexane. ED-MOF-74 was activated under 10 μBar vacuum at 100 °C for 4 h before N_2 physisorption and CO_2 adsorption studies.

MgO coating of a monolith: MgO nanoparticle coating on the 400 CPSI monolith was carried out using our previously published recipe.[26]

MOF-74/ED-MOF-74 on a monolith: Primary Mg-MOF-74 growth was carried out using a similar procedure as for powders. For secondary growth, 95 mg of $Mg(NO_3)_2$ and 22.4 mg of H_4(dobdc) were dissolved 10 mL DMF:EtOH:Water (15:1:1) solution. Mg-MOF-74 coated monolith was then immersed in the solution and the reaction was carried out at 120 °C for 21 h. ED-MOF-74 on a monolith was synthesized using a similar procedures as for powders.

4.2.2 Characterization

N_2 physisorption: N_2 adsorption at 77 K was measured on the monolith and MOF powders using a Micromeritics ASAP 2020 (powders) or 3Flex surface area analyzer (monoliths). In a typical experiment, 50 mg of powder or a 0.15-0.25 g piece of monolith piece was used. The surface area was estimated using the BET method in the P/P_0 range of 0.005-0.03. MOF-74 samples were outgassed at 250 °C for 12 h under 10 mtorr vacuum. ED-MOF-74 samples were outgassed at 100 °C for 4 h before adsorption measurements.

Powder X-ray diffraction (PXRD) measurements on MOF powders were made using a PANalytical X'Pert diffractometer using Cu Kα radiation from 2θ of 2° to 80°.

CO_2 adsorption experiments: CO_2 adsorption at 25 °C on the monolith and MOF powders was measured using a Micromeritics ASAP 2020 (powders) or 3Flex surface area analyzer (monoliths). In a typical experiment, 50 mg of powder or a 0.15-0.25 g piece of monolith piece was used. MOF-74 samples were outgassed at 250 °C for 12 h under 10 mtorr vacuum. ED-MOF-74 samples were outgassed at 100 °C for 4 h before the adsorption measurements.

Scanning electron microscopy was performed using a Hitachi Tabletop SEM TM 3030. Measurements were made using an accelerating voltage of 1 kV and 10 µA current.

4.3 Results and Discussion

Conventional Mg-MOF-74 synthesis has typically used soluble metal salts such $Mg(NO_3)_2$. For growth on the surface of a substrate, in the absence of prior seeding on the surface of monolith, most Mg-MOF-74 formation occurs in solution and then may be deposited as a film on the monolith surface. Unfortunately, this does not create a strong adhesion to the surface. So an alternate strategy of creating a MgO seed layer on the surface of the monolith was explored.[26] As a first step, Mg-MOF-74 synthesis from MgO was investigated using a variety of ligand concentrations and solvents. Following previous studies,[26,33] the MgO to Mg-MOF- 74 conversion was carried out in pure DMF at ligand concentrations of 0.1 M and 0.2 M. As shown in Figure 4.1, the magenta and black PXRD patterns show the crystallinity of the syntheses carried out in pure DMF at two different ligand concentrations, 0.1 M and 0.2 M, respectively. Although two key Mg-MOF-74 peaks at 7° and 12° 2θ can be identified, phase impurities in the form of other peaks at 2θ

of 14° and 18° are also observed. Additionally, MgO peaks corresponding at 43° and 62° are also identified. Further experiments were carried out with water-DMF mixtures, where 20% water (v/V) was added to the solution. As shown in the red and blue PXRD patterns in Figure 4.1, it can be seen that no peaks corresponding to phase impurities or MgO are observed in this case. It is hypothesized that the presence of water increased the rate of reaction by formation of $Mg(OH)_2$ as an intermediate species. Achieving the complete conversion of MgO to MOF-74 in a reasonable time with limited usage of ligand will be a key in the potential deployment of MgO based precursors for synthesis of MOFs for gas adsorption applications.

Further studies were carried out varying the amount of water (v/V) in the solution. PXRD patterns for Mg-MOF-74 produced in these studies are shown in Figure 4.2. No presence of the MgO was observed in resultant powder materials, indicating that a small amount of water plays an important role in the complete conversion of MgO to MOF-74. The corresponding N_2 physisorption data at 77 K and BET surface areas are presented in Table 4.1 and Figure 4.3 respectively.

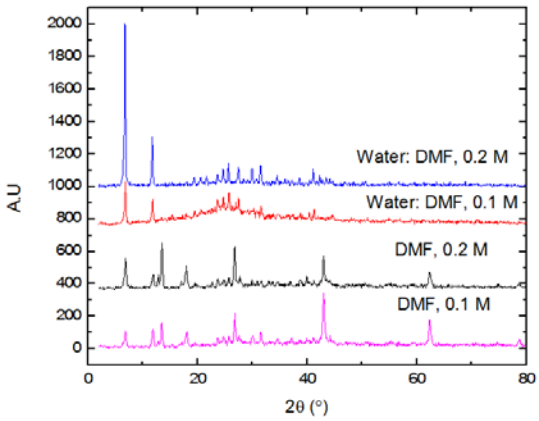

Figure 4.1 PXRD pattern for Mg-MOF-74 synthesized from MgO in DMF (magenta and black) and a DMF: water mixture (red and blue) for different ligand concentrations

Additionally, DMF, water and ethanol mixtures were also explored in the synthesis of Mg-MOF-74 from MgO. N_2 physisorption isotherms for the synthesized materials are presented in in Figure 4.4. The solvent mixture containing 5 % water (v/V), 5% EtOH (v/V) and the balance DMF (Red) showed the maximum physisorption of N_2 at 77 K. Finally, based on the excellent crystallinity and the high N_2 uptake obtained in the binary solvent system, further studies were done with an altered binary solvent composition of 20% water (v/V) in DMF. Addition of more than 20% water (v/V) led to an incomplete dissolution of ligand in the solution. Also, the outgassing time was adjusted to 12 h from 6 h based on previous studies in our group[16] which indicated a better activation of Mg-MOF-74 for gas adsorption studies.

Table 4.1 BET Surface Areas for Mg-MOF-74 samples made with varying DMF to water ratios

DMF water ratio	BET surface area
1:19	1272 m^2/g
1:9	1175 m^2/g
1:4	1207 m^2/g

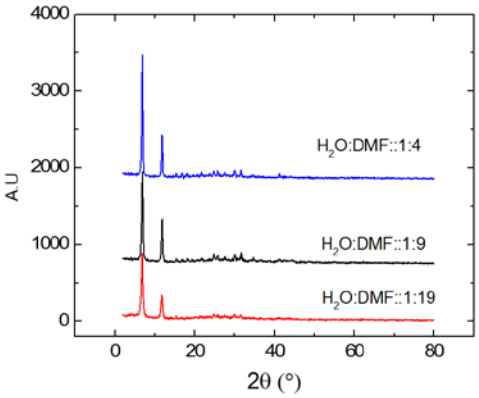

Figure 4.2 PXRD patterns for Mg-MOF-74 synthesized from MgO in a varying volumetric ratio of water to DMF.

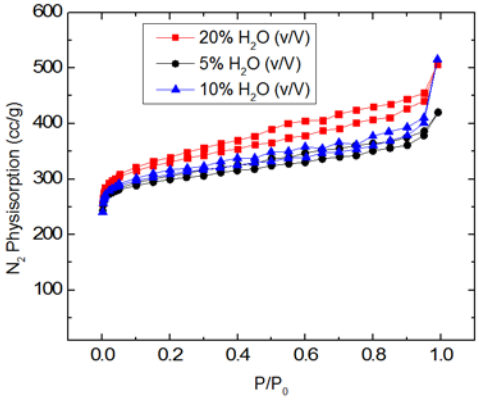

Figure 4.3 N_2 physisorption at 77 K for Mg-MOF-74 synthesized from MgO in a varying volumetric ratio of water to DMF.

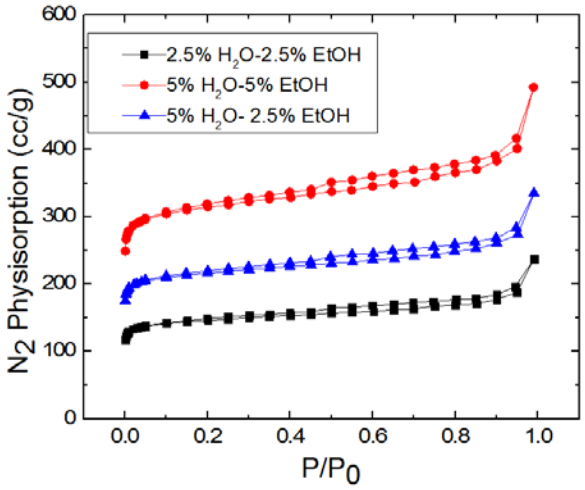

Figure 4.4 N_2 physisorption at 77K of Mg-MOF-74 synthesized from the solution of water, ethanol and DMF for various compositions.

Mg-MOF-74 growth on a monolith: Learning from the Mg-MOF-74 powder synthesis from MgO were applied to grow Mg-MOF-74 on a monolith. Following the recipe used in our previous publication,[26] an MgO seed layer was created on the surface of a 400 CPSI monolith by dip-coating the monolith in a solution of MgO (5% by weight) in MeOH and PEI (1% by wt.). As shown in Table 4.2, an MgO weight loading of 15% was obtained on

the monolith. Further reaction was carried out on the MgO-seeded monolith with 20% water in the DMF solution. An Mg-MOF-74 film constituting an 8% weight loading was obtained on the monolith, which is less than expected based on the synthesis stoichiometry. Some powder formation was also noticed in solution, which can be attributed to the homogeneous formation of Mg-MOF-74. This is not unexpected, as the presence of water, which while increasing the conversion of MgO to Mg-MOF-74, also lead to leaching of Mg into the solution. Therefore, as a next step, a further increase in the Mg-MOF-74 loading was achieved by secondary growth following the recipe of Yang et al.[16] Table 4.2 outlines the typical weight loadings achieved after MgO seeding, primary growth, and secondary growth. Figure 4.5 show SEM images of the monolith after secondary growth.

Table 4.2 Typical weight loadings achieved on a 400 CPSI monolith after MgO seeding, primary MOF growth, and secondary MOF growth

MgO weight loading on the monolith	Mg-MOF-74 loading after the primary growth	Mg-MOF-74 loading after the secondary growth
15%	8%	16%

N_2 physisorption measurements at 77 K and CO_2 adsorption at 25 °C using the Mg-MOF-74 grown on the monolith (blue) are compared with Mg-MOF-74 powder values (red) in Figure 4.6 & Figure 4.7 respectively. CO_2 and N_2 adsorption values on a monolith are normalized with respect to weight increase which has been attributed to MOF growth for the comparison. The CO_2 and N_2 uptakes on the monolith are normalized with respect to the weight increase which attributed to MOF growth on the surface to produce a fair comparison. A significant difference can be seen between the Mg-MOF-74 in the powder form and on the monolith. This difference is possibly because of the inaccessibility of some

adsorption sites as well as the presence of MgO on the MOF surface. Crystal intergrowth may lead to unavailability of some sites to the gas adsorption. BET surface areas for the Mg-MOF-74 powder and the Mg-MOF-74 grown on the monolith were found to be 1280 m^2/g and 635 m^2/g, respectively. The CO_2 uptake at 1.1 bar CO_2 was found to be 2.8 mmol/g for the Mg-MOF-74 on monolith. CO_2 uptake at 1.1 bar for Mg-MOF-74 on a monolith is 30% of the powder value at 1.1 bar which also scales similarly to N_2 physisorption values at 77 K from powder to monolith. CO_2 uptake values are comparable to the ones obtained by other researchers working on immobilizing MOFs on practical substrates.[20,24] Although Mg-MOF-74 shows very high CO_2 adsorption capacities under many conditions, they are not likely to be used under conditions containing significant moisture, as it has a degrading effect on the material.[9] Materials with more robust adsorption properties owing to better overall stability in the presence of moisture can be achieved by amine-functionalization of the open metal sites. Future work can explore these aspects on structured gas/solid contactors like MOFs.

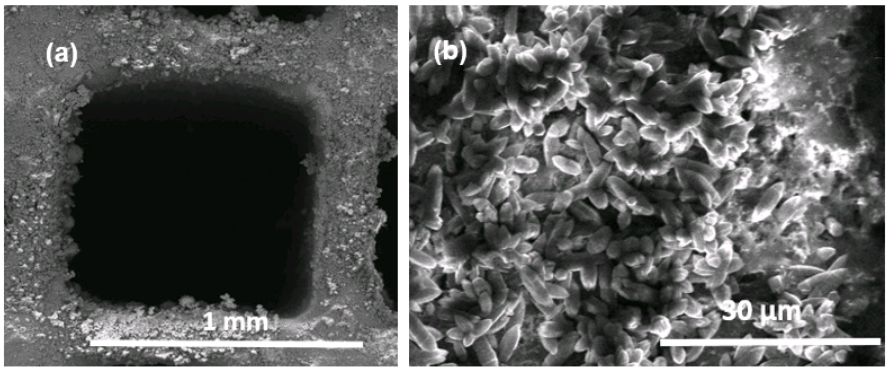

Figure 4.5 Mg--MOF-74 growth on a monolith surface obtained after both primary and secondary growth.

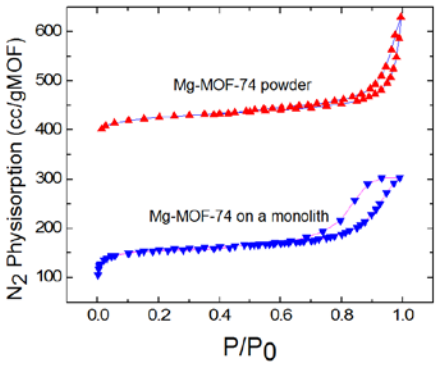

Figure 4.6 Comparison of N_2 physisorption at 77 K between Mg-MOF-74 powder (Red) and Mg-MOF-74 on a monolith (Blue). The data for MOF on the monolith is normalized with respect to MOF weight on the monolith surface

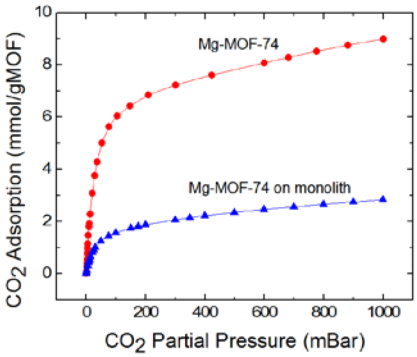

Figure 4.7 Comparison of CO_2 adsorption at 25 °C between Mg-MOF-74 powder (Red) and Mg-MOF-74 on a monolith (Blue). The data for MOF on the monolith is normalized with respect to MOF weight on the monolith surface

4.4 Conclusions

The scalable processing of MOFs for gas separations applications is critical to enable the practical use of such materials. In this work, we have demonstrated the generality of use of solid MOF precursors, such as MgO, to develop supported Mg-MOF-74 films for possible application in CO_2 capture. While this field is in a nascent stage, a more detailed understanding of MOF formation mechanisms and pathways on solid surfaces can lead to synthesis conditions that will allow scale-up of MOFs with a reasonable reaction time and resource use. Here we have identified one set of conditions where addition of water to a DMF solution created a faster MOF synthesis along with a phase-pure material in powder form. This method was further applied to grow Mg-MOF-74 films on a honeycomb monolith, giving a CO_2 uptake of 2.8 mmol/g at a CO_2 pressure of 1.1 Bar.

4.5 References

1. EPA. Inventory of U.S. Greenhouse Gas Emissions and Sinks: 1990–2011. US Environ. Prot. Agency **2013**, ES1-ES26.

2. Kirtman, B.; Power, S. B.; Adedoyin, J. A.; Boer, G. J.; Bojariu, R.; Camilloni, I.; Doblas-Reyes, F. J.; Fiore, A. M.; Kimoto, M.; Meehl, G. A.; et al. Chapter 11: Near-Term Climate Change: Projections and Predictability. Clim. Chang. 2013 Phys. Sci. Basis. Contrib. Work. Gr. I to Fifth Assess. Rep. Intergov. Panel Clim. Chang. **2013**, No. June, 953–1028.

3. Sumida, K.; Rogow, D. L.; Mason, J. a; McDonald, T. M.; Bloch, E. D.; Herm, Z. R.; Bae, T.-H.; Long, J. R. Carbon Dioxide Capture in Metal-Organic Frameworks. *Chem. Rev.* **2012**, 112 (2), 724–781.

4. Sanz-Pérez, E. S.; Murdock, C. R.; Didas, S. A.; Jones, C. W. Direct Capture of CO_2 from Ambient Air. *Chem. Rev.* **2016**, 116 (19), 11840–11876.

5. Belmabkhout, Y.; Serna-Guerrero, R.; Sayari, A. Amine-Bearing Mesoporous Silica for CO_2 Removal from Dry and Humid Air. *Chem. Eng. Sci.* **2010**, 65 (11), 3695–3698.

6. Qi, G.; Fu, L.; Giannelis, E. P. Sponges with Covalently Tethered Amines for High-Efficiency Carbon Capture. *Nat Commun* **2014**, 5.

7. Xu, X.; Song, C.; Andrésen, J. M.; Miller, B. G.; Scaroni, A. W. Preparation and Characterization of Novel CO_2 "molecular Basket" Adsorbents Based on Polymer-Modified Mesoporous Molecular Sieve MCM-41. *Microporous Mesoporous Mater.* **2003**, 62 (1–2), 29–45.

8. Grant Glover, T.; Peterson, G. W.; Schindler, B. J.; Britt, D.; Yaghi, O. MOF-74 Building Unit Has a Direct Impact on Toxic Gas Adsorption. *Chem. Eng. Sci.* **2011**, 66 (2), 163–170.

9. Kizzie, A. C.; Wong-Foy, A. G.; Matzger, A. J. Effect of Humidity on the Performance of Microporous Coordination Polymers as Adsorbents for CO_2 Capture. *Langmuir* **2011**, 27 (10), 6368–6373.

10. DeCoste, J. B.; Peterson, G. W.; Schindler, B. J.; Killops, K. L.; Browe, M. A.; Mahle, J. J. The Effect of Water Adsorption on the Structure of the Carboxylate Containing Metal–organic Frameworks Cu-BTC, Mg-MOF-74, and UiO-66. J. *Mater. Chem. A* **2013**, 1 (38), 11922.

11. Liu, J.; Benin, A. I.; Furtado, A. M. B.; Jakubczak, P.; Willis, R. R.; LeVan, M. D. Stability Effects on CO_2 Adsorption for the DOBDC Series of Metal–Organic Frameworks. *Langmuir* **2011**, 27 (18), 11451–11456.

12. Cho, H.-Y.; Yang, D.-A.; Kim, J.; Jeong, S.-Y.; Ahn, W.-S. CO_2 Adsorption and Catalytic Application of Co-MOF-74 Synthesized by Microwave Heating. *Catal. Today* **2012**, 185 (1), 35–40.

13. Choi, S.; Watanabe, T.; Bae, T.-H.; Sholl, D. S.; Jones, C. W. Modification of the Mg/DOBDC MOF with Amines to Enhance CO_2 Adsorption from Ultradilute Gases. *J. Phys. Chem. Lett.* **2012**, 3 (9), 1136–1141.

14. Andirova, D.; Lei, Y.; Zhao, X.; Choi, S. Functionalization of Metal-Organic Frameworks for Enhanced Stability under Humid Carbon Dioxide Capture Conditions. *ChemSusChem* **2015**, 8 (20), 3405–3409.

15. Bromberg, L.; Hatton, T. A. Aldehyde-Alcohol Reactions Catalyzed under Mild Conditions by Chromium(III) Terephthalate Metal Organic Framework (MIL-101) and Phosphotungstic Acid Composites. *ACS Appl. Mater. Interfaces* **2011**, 3 (12), 4756–4764.

16. Jiao, Y.; Morelock, C. R.; Burtch, N. C.; Mounfield, W. P.; Hungerford, J. T.; Walton, K. S. Tuning the Kinetic Water Stability and Adsorption Interactions of Mg-MOF-74 by Partial Substitution with Co or Ni. *Ind. Eng. Chem. Res*. **2015**, 54 (49), 12408–12414.

17. Howe, J. D.; Morelock, C. R.; Jiao, Y.; Chapman, K. W.; Walton, K. S.; Sholl, D. S. Understanding Structure, Metal Distribution, and Water Adsorption in Mixed-Metal MOF-74. *J. Phys. Chem. C* **2017**, 121 (1), 627–635.

18. Siegelman, R. L.; McDonald, T. M.; Gonzalez, M. I.; Martell, J. D.; Milner, P. J.; Mason, J. A.; Berger, A. H.; Bhown, A. S.; Long, J. R. Controlling Cooperative CO_2 Adsorption in Diamine-Appended Mg2(dobpdc) Metal–Organic Frameworks. *J. Am. Chem. Soc.* **2017**, 139 (30), 10526–10538.

19. Mcdonald, T. M.; Mason, J. A.; Kong, X.; Bloch, E. D.; Gygi, D.; Dani, A.; Crocellà, V.; Giordanino, F.; Odoh, S. O.; Drisdell, W. S.; et al. Cooperative Insertion of CO_2 in Diamine- Appended Metal-Organic Frameworks. *Nature* **2015,** 519, 303–308

20. Bae, T.-H.; Long, J. R. CO_2/N_2 Separations with Mixed-Matrix Membranes Containing Mg2(dobdc) Nanocrystals. *Energy Environ. Sci*. **2013**, 6 (12), 3565.

21. Wang, N.; Mundstock, A.; Liu, Y.; Huang, A.; Caro, J. Amine-Modified Mg-MOF-74/CPO-27-Mg Membrane with Enhanced H_2/CO_2 Separation. *Chem. Eng. Sci.* **2015**, 124, 27–36.

22. Campbell, J.; Tokay, B. Controlling the Size and Shape of Mg-MOF-74 Crystals to Optimise Film Synthesis on Alumina Substrates. *Microporous Mesoporous Mater.* **2017**, 251, 190–199.

23. Lee, D.-J.; Li, Q.; Kim, H.; Lee, K. Preparation of Ni-MOF-74 Membrane for CO_2 Separation by Layer-by-Layer Seeding Technique. *Microporous Mesoporous Mater*. **2012**, 163, 169–177.

24. Rezaei, F.; Lawson, S.; Hosseini, H.; Thakkar, H.; Hajari, A.; Monjezi, S.; Rownaghi, A. A. MOF-74 and UTSA-16 Film Growth on Monolithic Structures and Their CO_2 Adsorption Performance. *Chem. Eng. J.* **2016**, 3, http://dx.doi.org/10.1016/j.cej.2016.11.058.

25. Lawson, S.; Hajari, A.; Rownaghi, A. A.; Rezaei, F. MOF Immobilization on the Surface of Polymer-Cordierite Composite Monoliths through in-Situ Crystal Growth. *Sep. Purif. Technol.* **2017**, 183, 173–180.

26. Darunte, L. A.; Terada, Y.; Murdock, C. R.; Walton, K. S.; Sholl, D. S.; Jones, C. W. Monolith-Supported Amine-Functionalized Mg_2(dobpdc) Adsorbents for CO_2 Capture. *ACS Appl. Mater. Interfaces* **2017**, 9 (20), 17042–17050.

27. Maserati, L.; Meckler, S. M.; Bachman, J. E.; Long, J. R.; Helms, B. A. Diamine-Appended Mg_2(dobpdc) Nanorods as Phase-Change Fillers in Mixed-Matrix Membranes for Efficient CO_2/N_2 Separations. *Nano Lett.* **2017**, 17 (11), 6828–6832.

28. Thakkar, H.; Eastman, S.; Al-Naddaf, Q.; Rownaghi, A. A.; Rezaei, F. 3D-Printed Metal-Organic Framework Monoliths for Gas Adsorption Processes. *ACS Appl. Mater. Interfaces* **2017**, 9 (41), 35908–35916.

29. Kulkarni, A. R.; Sholl, D. S. Analysis of Equilibrium-Based TSA Processes for Direct Capture of CO_2 from Air. *Ind. Eng. Chem. Res.* **2012**, *51* (25), 8631–8645.

30. Sinha, A.; Darunte, L. A.; Jones, C. W.; Realff, M. J.; Kawajiri, Y. Systems Design and Economic Analysis of Direct Air Capture of CO_2 through Temperature Vacuum Swing Adsorption . *Ind. Eng. Chem.Res.* **2016**.

31. Pimentel, B. R.; Fultz, A. W.; Presnell, K. V; Lively, R. P. Synthesis of Water-Sensitive Metal–Organic Frameworks within Fiber Sorbent Modules. *Ind. Eng. Chem. Res*. **2017**, 56 (17), 5070–5077.

32. Zhan, G.; Zeng, H. C. Alternative Synthetic Approaches for Metal-Organic Frameworks: Transformation from Solid Matters. *Chem. Commun.* **2017**, 53 (1), 72–81.

33. Maserati, L.; Meckler, S. M.; Li, C.; Helms, B. A. Minute-MOFs: Ultrafast Synthesis of M_2(dobpdc) Metal–Organic Frameworks from Divalent Metal Oxide Colloidal Nanocrystals. *Chem. Mater*. **2016**, 28 (5), 1581–1588.

5 ANALYSIS OF AMINE-FUNCTIONALIZED Mg_2(dobpdc) SYSTEM FOR CO_2 CAPTURE FROM DILUTE FEEDS

(Acknowledgment: Simulation results for the breakthrough profiles in this chapter have been contributed by Trisha Sen)

5.1 Introduction

CO_2 capture from ultra-dilute feeds is gaining attention as a part of carbon management programs. [1–3] Some examples are direct capture of CO_2 from air (CO_2 concentration ~ 400 PPM), also known as direct air capture (DAC) and enclosed air capture (CO_2 concentration ~ 5000 PPM). DAC is one of the few carbon emissions mitigation technologies that is considered carbon negative. Amine-functionalized adsorbents such as mesoporous silica,[3–5] carbon,[6] metal organic frameworks (MOFs)[7,8] have attracted a considerable attention because of their high CO_2 capacities even at ultra-dilute partial pressures of CO_2. Most of the research in the CO_2 capture field has focused on the development of materials with superior equilibrium adsorption capacities. High equilibrium capacities are desirable to achieve economically attractive operation of CO_2 capture by keeping the system size reasonable for a desired throughput.

Metal organic frameworks (MOFs) are a class of hybrid organic-inorganic materials that have shown a lot promise towards CO_2 capture. Their high tunability allows a systematic tuning of many MOF structures[9–11] resulting in a high CO_2 adsorption at ultra-

dilute CO_2 concentrations. One such example is the amine-functionalized Mg_2(dobpdc) system reported by the Long group.[12–14] The Mg_2(dobpdc) framework, when functionalized with N,N'-dimethyl ethylene diamine (MMEN) and ethylene diamine (ED), showed 3 mmol/g[14] and 2.83 mmol/g,[15] respectively, under the ultra-dilute conditions (0.4 mbar) corresponding to direct air capture (DAC) conditions. Cooperative insertion of CO_2 in the diamine-functionalized Mg_2(dobpdc) has led to "all or nothing" CO_2 adsorption over a narrow change in the CO_2 partial pressure. This resulted in materials with sigmoidal isotherms where the step can be tuned at different temperatures with a combination of amines and metals. The tunability of the sigmoidal isotherm with temperature has the potential to achieve a high working capacity with a lower temperature swing for a temperature swing adsorption process, attracting significant interest.

Additional considerations such as the material's long-term stability under humid and oxidatizing conditions, suitable adsorption/desorption kinetics, and straightforward regeneration are also required to develop adsorbents for a practical process.[8] Quite often, the kinetics of CO_2 adsorption puts limitations on the number of cycles and/or the amount of adsorbent material needed to achieve the desired throughput of the system. Specifically, in purification processes, the adsorption process is stopped when breakthrough of CO_2 is achieved. The kinetics of CO_2 adsorption can also limit the efficient utilization of the bed, as slow adsorbing systems can have long mass transfer zones (MTZ), leaving some fraction of the bed unused. This has led to the use the dynamic capacity at the breakthrough as a more useful metric than the equilibrium capacity, which is most often reported in the literature. Direct air capture processes are often run as extraction processes, where the

emphasis is on rate of CO_2 capture and throughput of the system and operations are typically designed at a lower extraction fraction from the feed than a typical purification process.

Practical applications require the adsorbent be deployed in a fixed-bed, immobilized on a practical substrate support such as honeycomb monolith,[16] or hollow fibers,[17,18] or deployed in a fluidized bed. Such materials can also be used in more concentrated feeds in mixed-matrix membranes.[19] However, use in ultra-dilute systems requires special attention be paid to the resistance to gas-solid contacting, necessitating designs that offer low pressure drops, such as fiber and monolith contactors. Understanding the mass transfer in these systems can be challenging with many competing heat and mass transfer effects. Typical mass and heat transfer regimes in a packed bed or film system are film, macropore, or micropore resistances and adsorption/desorption/reaction. Film and macropore resistances are relatively well understood through a variety of correlations such as the Sherwood, Stephane-Maxwell, and Chapman-Enskog correlations that account for a variety of factors such as flow conditions, gas composition, and the porosity of the bed. Non-trivial components of system design include the estimation of micropore diffusion, surface resistance, and the reaction (or adsorption/desorption) kinetics. Usually, one or more of these are controlling resistances and the determination of this needs a careful experimental design. Pulse-field gradient NMR (PFG-NMR),[20] quasielastic neutron scattering,[21] and infrared microscopy[22] are some of the state-of-the-art microscopic techniques used for the precise measurement of CO_2 diffusion coefficients inside the crystal of a microporous material. These techniques have

also highlighted the importance of a surface barrier for microporous materials, as hindered access to the micropores often limits the gas uptake, leading to under-prediction of the diffusion coefficient.[23,24] One of the challenges associated with microscopic techniques is the requirement of use of large, single crystals, the availability of which can be a limiting factor in elucidating the controlling resistance. Zero length column (ZLC)[25] or frequency response (FR)[26] methods are some of the commonly used macroscopic methods that have shown great potential to measure diffusion coefficients with a wider applicability.

Although the kinetics of adsorption of gases and liquids in many microporous materials are well documented,[27] limited studies exist for transport of CO_2 in supported amine materials. Identifying the controlling resistance of mass transfer is the most challenging task, requiring precise control over material and experimental design. With macroscopic techniques, gravimetric uptake or pressure decay are commonly used to measure the diffusion of CO_2 or the kinetics of the adsorption reaction. Many research groups modeled CO_2 adsorption as reaction limited and Several different CO_2 adsorption kinetic models have also been proposed for thermogravimetric gas (TGA) uptake analysis for amine-functionalized adsorbents. Pseudo-first order, pseudo-second order,[28] Avarami's fractional-order, and other fractional-order[29] kinetic models are some of the commonly employed models. Serna-Guerro[30] et al. studied TRI-PE-SBA-15 (a aminosilane-grafted mesoporous silica material) on a TGA using first order, pseudo-second order, and Avrami models and suggested the Avrami model fit the data best for the adsorption of CO_2 at 5% concentration in N_2 at high temperatures. The Avarami model, which is traditionally used for phase transition and crystal growth,[31] has been increasingly applied to CO_2 adsorption

in amine-functionalized materials partly because of its ability to model an empirically observed change in uptake rate during the adsorption. Some examples where this model has been applied include amine-functionalized multi-walled carbon nanotubes,[32] TEPA-functionalized mesoporous silica,[33,34] and poly(ethyleneimine) (PEI) modified phenolic resin.[35] One common problem with the Avrami model is the lack of an underlying physical mechanism, and the rate constant becoming very large at a large time scales.

In other studies, the Ritter group has studied CO_2 adsorption in PEI functionalized silica at different concentrations (1-100 %) and temperatures (40-100 °C) using semi-empirical models.[36] They modeled the CO_2 capture process as a combination of physisorption and chemisorption processes. Later Abdollahi-Govar et al.[37] analyzed the system using multiple semi-empirical models that took into considerations different reaction sites, and reaction pathways. They observed that the model with three reactions in parallel attributed to different amine sites in PEI had the best fit for a wide set of temperature and concentration conditions. Other examples of similar approaches include a generalized dry and humid CO_2 adsorption model using amine-functionalized silica by Suh and Sun[38] and a study of silica functionalized with amine epoxybutane-modified PEI by Jung et al.[39]

While an TGA uptake experiment is useful to characterize the gas adsorption macroscopically, understanding mass transfer in packed beds or other supported adsorbent systems for practical application needs consideration of additional factors such as axial dispersion, the adsorption isotherm shape, and heat effects. In such cases, the linear driving force (LDF) model is one of the most commonly used methods to analyze such systems.

Bollini et al.[40] analyzed CO_2 adsorption on 3-aminopropyl silane (APS) functionalized mesoporous SBA-15 silica using both a TGA and packed bed adsorber. They modeled the breakthrough adsorption of CO_2 for different concentrations and different amine loadings using a linear driving force (LDF) model and found that the single parameter LDF model is not sufficient to predict the long tail observed in the CO_2 breakthrough of packed bed of the material at high loadings of amines. They also observed that heat effects played a negligible role when the breakthrough adsorption experiment was carried at low flow rates for dilute feeds. As a next step, they analyzed CO_2 adsorption in the APS-functionalized SBA-15 as a combination of two transport processes, where the diffusion of CO_2 in the mesopores was envisioned as fast diffusion in mesopores followed by a slower diffusion through the amine layer to buried adsorption sites. The resultant LDF model had two different parameters that accounted for two different transport mechanisms.

The linear driving model (LDF) model uses a lumped coefficient (k_{ads}) to model the mass transfer of the adsorbate into the particle. It involves significant averaging and approximations on the population of particles, but the overall system can be analyzed consistently for practical application. Following the Glueckauf approximation,[41] k_{ads} can be correlated to film, macropore and micropore resistances. This can also be used as a first set of approximations of the diffusion coefficient in the materials, and suitable experiments like zero length column measurements or PFG-NMR experiments can be designed to measure diffusion in microporous materials more precisely.

A well-designed experiment with a smaller bed is attractive as it will also allow an accurate prediction of larger beds if it can capture the dynamics of CO_2 adsorption

satisfactorily. Some of the parameters of interest are the CO_2 concentration profile at the exit of the bed, fractional bed usage, overall CO_2 capture fraction breakthrough time, and adsorption rate constant, k_{ads}. As a first step, the development of the CO_2 concentration profile in a packed bed when the concentration of one component has a step change can be analyzed with a simple equilibrium wave theory that takes into account different isotherm shapes.[42–45] Equilibrium wave analysis only approximates the actual behavior of a fixed bed system, as it does not take into the account heat and mass transfer effects. Nevertheless, many of important features of a packed bed can be qualitatively analyzed using this theory. As there is a step change in the concentration of one component, an adsorption wave develops in the bed. Mass transfer in the bed can be modeled by equation 1.

$$\frac{\partial C_g}{\partial t} = D_{ax}\frac{\partial^2 C_g}{\partial z^2} - \frac{u_{g0}}{\varepsilon}\frac{\partial C_g}{\partial z} - \frac{(1-\varepsilon)\rho_p}{\varepsilon}\frac{dq}{dt} \quad (1)$$

In the absence of any dispersive effects because of diffusion of gas molecules, the actual velocity (w) of a particular concentration front can be related to the superficial velocity (u_g) by equation 2.

$$w = \frac{u_g/\varepsilon}{1+(\frac{1-\varepsilon}{\varepsilon})\rho_p\frac{dq}{dc}} \quad (2)$$

where w is the actual velocity of concentration front c, and $\frac{dq}{dc}$ is the slope of the isotherm. In the case of a linear isotherm (q = Kc) the slope of the isotherm, K, is constant, so the concentration front moves at the same velocity. In case of Type III (Figure 5.1a top), the slope of the isotherm will increase with the concentration so high concentration fronts will

move at a slower speed than low concentration fronts (Figure 5.1a middle). This leads to a dispersive wave leading to underutilization of the bed (Figure 5.1a bottom). In the case of type I isotherms characterized by Langmuir, Freundlich, and Toth isotherms, a peculiar case is created where the high concentration front will move faster than the low concentration front because of progressive decrease in the slope of the isotherm (Figure 5.1b top). This leads to a self-sharpening concentration front (Figure 5.1b middle) and produces a sharp breakthrough curve which is also called as shock breakthrough curve (Figure 5.1b bottom). These types of isotherms are thus referred to as "favorable isotherms" and lead to better utilization of the adsorbent bed. In this case, the development of the concentration front in the bed can be qualitatively analyzed using the slope of the cord that connects the initial state and the feed concentration on the isotherm. This rule is also known as the Golden's string rule[46] and velocity of concentration in the bed is approximated by equation 3.

$$w = \frac{u_g/\varepsilon}{1+(\frac{1-\varepsilon}{\varepsilon})\rho_p\frac{\Delta q}{\Delta c}} \quad (3)$$

Most amine-functionalized sorbents have shown a favorable Langmuir or Toth isotherms for CO_2 adsorption and correspondingly a shock breakthrough curve. In contrast, Mmen-Mg_2(dobpdc) and other materials[13,47] in this family have shown sigmoidal isotherms that are otherwise rare in CO_2 adsorption in amine-functionalized adsorbents. Sigmoidal isotherms, however, are commonly observed in single component alcohol,[48] and water[16,49] adsorption in MOFs and silica.

Cousin-Saint-Remi and Denayer[50] recently applied the Golden's string method for the analysis of ethanol adsorption in ZIF-8. In this method, an operating line is drawn from the initial point (I) to the feed or the final point (F) on the isotherm without crossing the isotherm. In the case of an unfavorable type III isotherm, the operating line will lie to the left of the isotherm (Figure 5.1 top). In the case of a favorable type I isotherm, the operating line will lie to the right of the isotherm (Figure 5.1b top). In case of the sigmoidal isotherm (Figure 5.1c top), the isotherm will be divided into a series of zones and the operating line will be drawn in for each zone without intersecting the isotherm in each zone. This is achieved by drawing tangents to the equilibrium curve from both the feed and initial conditions. Velocity of the concentration front in each zone can be approximated by equation 3 and the discontinuity in the isotherm leads to a dispersive wave in between the two tangents as two different concentration fronts move at different velocities (Figure 5.1c middle). This type of breakthrough curve is also called as "dual shock breakthrough" or "shock-wave-shock" breakthrough curve (Figure 5.1c bottom).

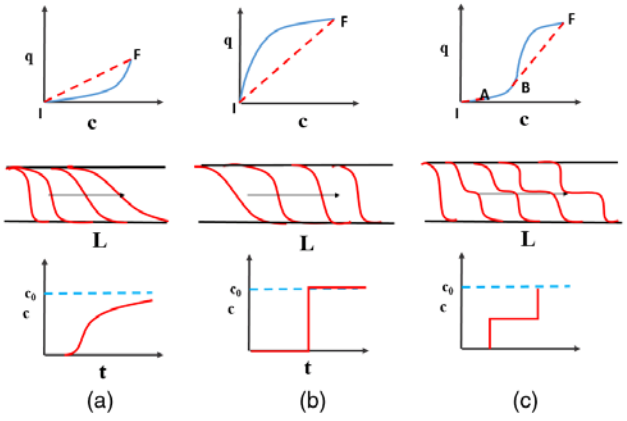

Figure 5.1 Shapes of various types of isotherms (top), corresponding concentration fronts inside the bed (middle) and corresponding breakthrough curves (top). A direct string is drawn between the initial state of the bed (I) and the feed point (F) and the velocity of the concentration front inside the bed can be qualitatively analyzed.

In this work, we have studied CO_2 adsorption in mmen-Mg_2(dobpdc) for ultra-dilute conditions using a packed bed system. Applying the equilibrium wave theory, we have analyzed the system at four different concentrations that represent different regimes for the resulting breakthrough profile, as predicted by the wave theory. Subsequently, we analyzed the predicted breakthrough profile with experimental data. Breakthrough adsorption experiments were performed at different flowrates and temperatures and the corresponding breakthrough profiles were analyzed using a simple linear driving force model that accounts for different mechanisms of mass transfer in the system. Our results indicate that two mass transfer coefficients are necessary to adequately model the experimental breakthrough profile. Our results also indicate that velocity in the bed has a significant impact on the shock-wave-shock breakthrough profile at 400 PPM and leads to poor utilization of the bed. Given a better utilization of the bed beyond 1% concentration, it is recommended that mmen-Mg_2(dobpdc) should be used for feeds with CO_2 concentrations beyond 1% CO_2 concentration. This work also develops a general framework that can be used to analyze other materials in the diamine-Mg_2(dobpdc) system.

5.2 Experimental Section

5.2.1 Chemicals

$Mg(NO_3)_2$-6-H_2O (Fischer, reagent grade), N-N' dimethyl ethylene diamine (Fischer, reagent grade), dimethylformamide (Fischer, ACS grade), N-hexane (Fischer, anhydrous,) and methanol (BDH Chemicals, ACS grade) were used as received. N-hexane and MMEN were stored in an N_2 containing glovebox to keep them relatively moisture free.

5.2.2 Material synthesis

H_4(dobpdc) was synthesized following recipes of McDonald et al.[10] Mg_2(dobpdc) with crystal lengths in the range 5-8 μm was then synthesized following the recipe of McDonald et al.[14] More specifically, the synthesis was performed in a convection oven at 120 °C to achieve a narrow distribution of crystal sizes.

5.2.3 Characterization

N_2 Physisorption & **Powder X-ray diffraction** (PXRD) measurement details can be found in our previous publication.[51]

CO_2 adsorption isotherms were obtained using a Micromeretics ASAP 2020 at various temperatures. MOF samples (~70 mg) were activated using conditions similar to N_2 physisorption.

Gravimetric CO_2 uptake experiments: CO_2 adsorption was measured on a TA instruments Q500 thermogravimetric analyzer (TGA). In typical experiments, 10 mg of MOF powder was activated in flowing helium (90 mL/h) for 4 h at 100 °C followed by adsorption with CO_2 mixture in helium (90 mL/h) with the adsorption time of 30 h. Adsorption experiments were performed with CO_2 concentrations of 400 PPM and 1000 PPM concentration at 25°C and 35 °C.

Breakthrough adsorption experiments: A custom built setup, as shown in Figure 5.2, was used to perform breakthrough adsorption measurements. Helium was used as the carrier gas. Premixed mixtures of 100 & 400 PPM were obtained from Matheson Trigas

Ltd. Premixed mixtures of 1000, and 10010 PPM CO_2 were obtained from Airgas Inc. The system consists of mass flow controllers (MFC, 0-200 SCCM/min N_2) to control the flowrate of helium and premixed mixtures of CO_2 in He. A LI-COR 840 analyzer was used to continuously measure the effluent gas concentration. The LI-COR 840 is an absolute non-dispersive infrared (IR) based analyzer with the measurement range of 0-20000 PPM. The dead time of the system was obtained by flowing 400 PPM He, 400 PPM CO_2 in N_2 over the same bed saturated with N_2. He breakthrough time was used to estimate the deadtime of the system. Typical deadtime in the system was less than a minute which significantly less than both breakthrough as well as saturation times. The temperature in the bed was recorded with an inline type K thermocouple. MOF powders were sieved to obtain particles in the size range of 53-153 µm. The packed bed system was well insulated and the temperature was controlled using an Omega benchtop CSi32 PID based controller. The bed was regenerated at 110 °C for 4 h until the exit concentration was below 5 ppm between cycles. Other properties of the bed are listed in Table 5.1.

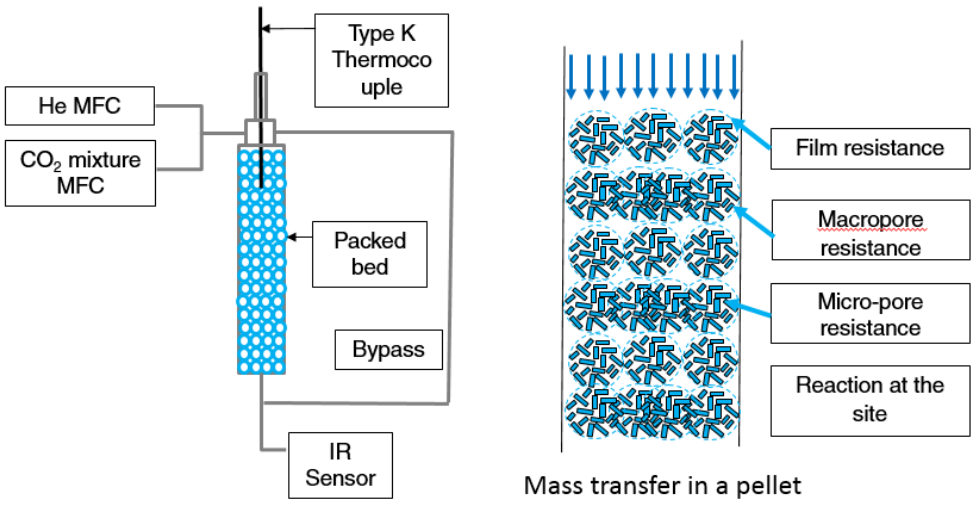

Figure 5.2. Packed bed adsorption system (left) and different modes of mass transfer inside a particle (right)

Table 5.1 Parameters of the packed bed adsorber and operating conditions.

Packed bed experiments parameters	**Value**
Length of the bed	5 cm
Internal radius	0.4 cm
Desorption Temperature	110 °C
Adsorption Temperature	23 °C, 49 °C, 70 °C
Particle size (d_p)	53 – 153 µm
MOF crystal length	4 µm
MOF crystal density	860 kg/m^3
Particle porosity	0.5
Bed porosity (ε)	0.7
Feed	
Pressure	1.1 Bar
Flow rate	17.2 mL/min, 28 mL/min, 48 mL/min, & 100 mL/min
Concentration of CO_2 in the feed	400 PPM, 1000 PPM, 5336 PPM, & 10010 PPM

5.2.4 Adsorption isotherm fitting

The sigmoidal CO_2 isotherm of mmen-Mg_2(dobpdc) is modeled using the method outlined by Hefti et al.[52] Adsorption (q_L) of CO_2 below the step partial pressure, P_{step} is represented by the Langmuir isotherm. Adsorption of CO_2 (q_U) beyond the step partial pressure is modeled by a dual site Langmuir-linear isotherm. The total adsorption of CO_2 is a weighted function of q_L and q_U.

$$q_L = \frac{q_L^{\infty} b_L p}{1 + b_L p} \tag{4}$$

$$q_U = \frac{q_U^{\infty} b_U p}{1 + b_U p} + b_H p \tag{5}$$

$$q(p,T) = q_L(p,T)\big(1 - w(p,T)\big) + q_U(p,T)w(p,T) \tag{6}$$

The transition pressure, p_{step} follows the temperature dependence by equation 7. A reference state was assumed at 313 K for the p_{step} of 0.78 mbar. Other parameters in the

isotherm model are listed in Table C1. Temperature dependence of various parameters was obtained based on the data by McDonald et al.[14]

$$p_{step}(T) = p_{step,0}\exp\left(\frac{-H_{step}}{R}\left(\frac{1}{T_0} - \frac{1}{T}\right)\right) \quad (7)$$

5.2.5 Linear driving force model for packed bed adsorption

A simplified packed bed model for CO_2 adsorption was developed to simulate the temperature swing adsorption process. In a typical packed bed experiment, adsorbents were sieved to obtain adsorbent particles between 53-153 μm. This typically results in macropores and micropores inside each particle. A typical mass balance equation in the packed bed is modeled by equation 1. Equation 1 accounts for mass transport by diffusion, convection and adsorption inside the particle:

$$\frac{\partial C_g}{\partial t} = D_{ax}\frac{\partial^2 C_g}{\partial z^2} - \frac{u_{g0}}{\varepsilon}\frac{\partial C_g}{\partial z} - \frac{(1-\varepsilon)\rho_p}{\varepsilon}\frac{dq}{dt} \quad (1)$$

and

$$\frac{\partial q}{\partial t} = k_{LDF}(q_{eq} - q) \; for\, p < p_{step} \quad (8)$$

$$\frac{\partial q_2}{\partial t} = k_{fwd}(q_2^* - q_2)(C_g)^n \qquad p_{step} < p \quad (9)$$

with initial and boundary conditions that account for zero loading and zero concentration of CO_2 in the bed:

$$c\,(x,0) = 0,\ q\,(x,0) = 0 \tag{10}$$

$$x = 0,\ C = C_0 \tag{11}$$

$$X = L,\ \frac{\partial c}{\partial x} = 0 \tag{12}$$

where D_L, u_{g0}, ε, and $k_{LDF,}$ c, and q are the axial dispersion coefficient, superficial velocity, porosity of the bed, linear driving force constant, gas phase concentration, and averaged adsorbed concentration respectively. D_L has been calculated using the Wakao & Funazkri empirical correlations[53] (Equations C13-C15).

Additional assumptions in the model are

1. No radial gradient in concentration, velocity, and temperature
2. Gas phase in the bed is described by the ideal gas equation
3. Entry effects on heat transfer and mass transfer have been neglected

5.3 Results and Discussion

5.3.1 Isotherm fit and temperature dependence of P_{step}

As a first step, the CO_2 adsorption isotherm is modeled by a dual site Langmuir-linear isotherm model. The obtained isotherm parameters are listed in the Table C1. A good fit between experimental data (red) and calculated data (black) is obtained in Figure 5.3, which can be then be used to further extrapolate the data at different temperatures using the temperature dependence of various parameters listen in Table C1. The data is only presented upto 10 mBar of CO_2 partial pressure which is the area of interest for this study. Figure 5.4 outlines the expected change in P_{step} as a function of temperature. P_{step} is the

pressure beyond which cooperative insertion of CO_2 in the mmen-Mg_2(dobpdc) framework leads to the saturation of amine sites and thereby a high CO_2 adsorption. For the design of a practical system design, P_{step} is important because the adsorption bed will have a high CO_2 loading for partial pressures greater than the P_{step}. A gas mixture having a CO_2 partial pressure lower than P_{step} will slip through the bed because of the low adsorption in the bed under those conditions. P_{step} can be tuned to higher or lower values based on a change in the diamine structure and temperature. Experiments in this work were carried out at mean temperatures of 23 °C, 49 °C and 70 °C and simulated isotherms were obtained for those cases.

5.3.2 Application of the wave theory and identification of breakthrough profile zones

As the concentration front enters the packed bed of the adsorbent, different concentrations will move at different velocities following equation 2. This leads to the creation of a self-sharpening (shock) or dispersive wave (wave) depending on the initial state of the bed and the feed concentration (Figure 5.1 a,b,c middle). The development of concentration profile in the bed can be analyzed by Golden's string rule. Saint-Cousin and Denayer[50] have analyzed a similar system for ethanol adsorption in ZIF-8. In Golden's string analysis, as shown in the Figure 5.5, the initial state of the bed denoted by I and the feed concentration are denoted by F are identified and a string is drawn between the two points. In the case of an isotherm that is on the left of the operating line, the slope of the operating line will be used to estimate the velocity of the self-sharpening front. In the case where the operating line intersects the isotherm, as shown in the Figure 5.5a, tangents are

drawn from both I and F to the isotherm and the velocity is estimated for each zone, as shown in Figure 5.5b and Figure 5.5c.

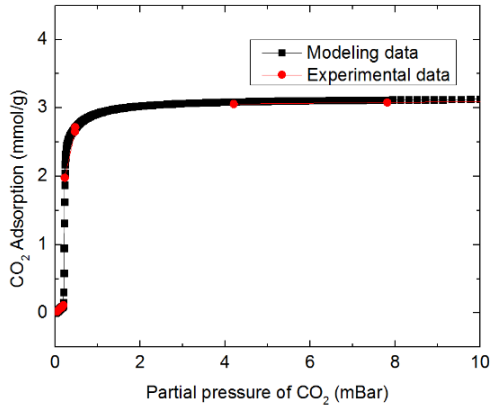

Figure 5.3. Experimental data (red) at 25 °C and modeling fit (black) at 25 °C based on fitted parameters in Table C1

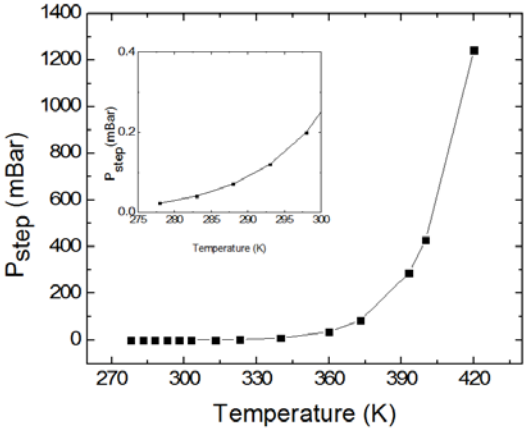

Figure 5.4. Predicted change in P_{step} based on the temperature of the material during adsorption.

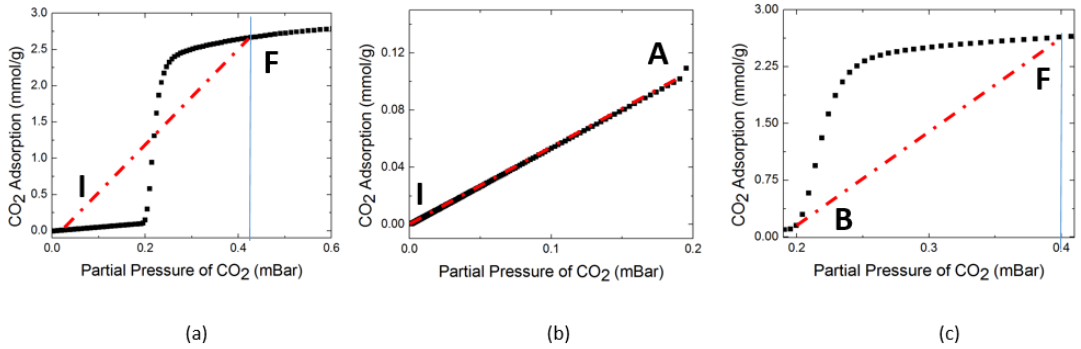

Figure 5.5. Generalized method to analyze the breakthrough curve resulting for the isotherm (a) of mmen-Mg_2(dobpdc). Three distinct zones are noted, before, after and at the step change. An operating line is drawn between the initial state of the bed (I) and the feed concentration (F) for a particular experiment. In cases where the line intersects the isotherm (a) tangents from I and F to the isotherm are used as the operating lines, as shown in (b) and (c).

5.3.3 Application of wave theory to identify velocities of the concentration fronts

The effect of different feed concentrations on the development of velocity profiles, leading to different adsorption characteristics for the Mg(dobpdc)-mmen system is explored here. Examples of CO_2 adsorption and the corresponding velocities of concentration fronts are depicted in Figure 5.6 (left) and Figure 5.6 (right) for feeds with CO_2 partial pressures of 0.4 mBar and 1 mBar, respectively. The bed was regenerated at 110 °C in helium prior to the adsorption so the initial point (I) was assumed to be at zero CO_2 loading in the bed. A CO_2 mixture in helium was flowed over the bed at a flow rate of 28.2 mL/min. As a direct string between the initial point and the final point crosses the isotherm, two separate zones (A and B) are identified based on tangents to the isotherm from I and F. The zone A operating line has a lower slope than zone B, hence, a correspondingly higher velocity. This leads to an early shock wave followed by a dispersive wave. As the partial pressure of CO_2 in the bed increases from 0.4 mBar to 1 mBar, the slope of the operating line decreases so the velocity of the concentration front increases, leading to a smaller dispersive wave between the two shocks waves for a feed partial pressure of 1 mBar.

As the partial pressure of CO_2 in the feed increases to 5.4 mBar, the difference between the velocities of the concentration front in zone A and B (Figure 5.7 left) become small, and hence, a small dispersive wave will be generated between the two shocks. For CO_2 partial pressures above 9.7 mBar a direct cord can be drawn between I and F (Figure 5.7 right) and a single shock is expected to move at the same velocity.

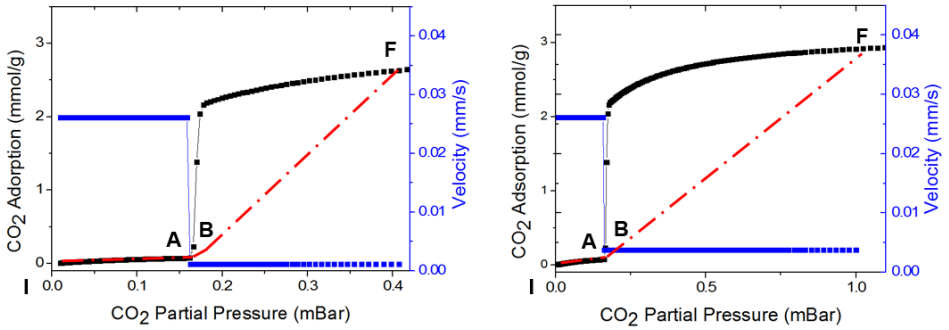

Figure 5.6 Velocities of concentration fronts (blue) and operating lines (red) for the feed (F) with CO_2 partial pressures of 0.4 mBar (left) and 1mBar (right). The bed was completely regenerated indicating zero CO_2 loading at the start of adsorption (I). The velocities were calculated for the adsorption experiment at 23 °C at the gas flowrate of 28.2 mL/min.

It should also be noted that equation 2 is strictly applicable to the feed with trace quantities of CO_2. As the partial pressure of CO_2 in the bed increases for conditions of the flue gas capture, the velocity of the front becomes a function of mole fraction of CO_2 and the concentration front is expected to move faster as the CO_2 is depleted from the feed. However, since the maximum partial pressure we have considered in this study is 1 mBar, equation 2 is used to analyze the CO_2 breakthrough curve.

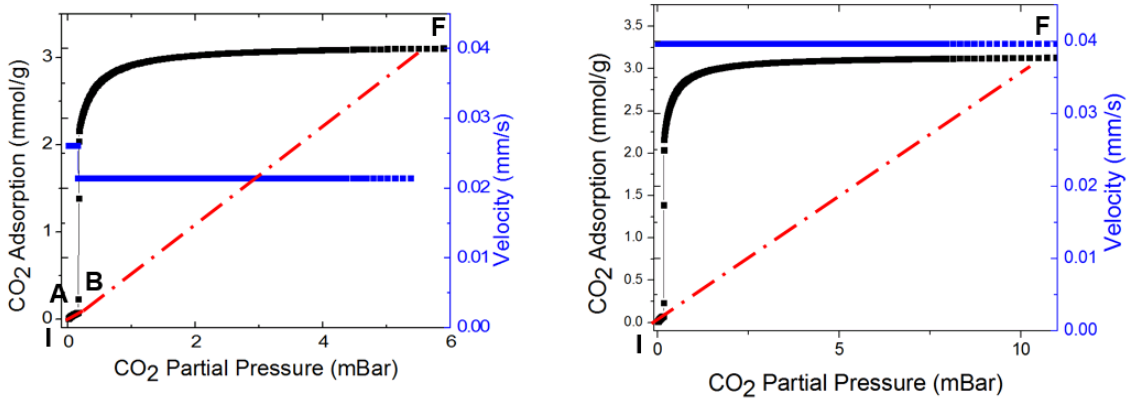

Figure 5.7 Velocities of concentration fronts (blue) and operating lines (red) for the feed (F) with CO_2 partial pressures of 5.4 mBar (left) and 10 mBar (right). The bed was completely regenerated indicating zero CO_2 loading at the start of adsorption (I).The velocities were calculated for the adsorption experiment at 23 °C at the gas flowrate of 28.2 mL/min.

This analysis can further be extended to identify different breakthrough profiles resulting from the location of initial point and feed concentration on the isotherm. In the present analysis, the bed is assumed free of CO_2 at the start of the adsorption. Depending on the feed concentration, different zones can be identified as outlined in Table 5.2 for possible breakthrough curves. For less than 0.163 mBar of CO_2 partial pressure in the feed, a single shock wave is expected. For partial pressures between 0.163 mBar and 0.165 mBar, a discontinuity in the isotherm leads to increase in the slope as shown in Figure 5.8 and hence a decrease in the velocity of the concentration front leading to a dispersive wave. For partial pressures between 0.165 mBar and 9.7 mBar, a shock-wave-shock breakthrough adsorption curve is expected (Figure 5.6 and Figure 5.7 left), as the discontinuity in the isotherm leads to a wave between the two self-sharpening fronts. A single cord drawn from I to the point of discontinuity when extended further meets the isotherm at partial pressure of 9.7 mBar, indicating a development of a single shock front occurs for feeds with partial pressures of more than 9.7 mBar (Figure 5.7 right).

Table 5.2 Identification of mass transfer zones.

Partial Pressure of CO_2	**Breakthrough profiles**
P< 0.163 mBar	Shock
0.163 mBar < P < 0.165 mBar	Shock-wave
0.165 mBar < P < 9.7 mBar	Shock-wave-shock
9.7 mBar < P	Shock

Resultant breakthrough profile was simulated in gProms and simulation results are presented in Figure 5.8 (right) where normalized CO_2 concentration at the exit of the bed was plotted against time (h). The shock-wave-shock breakthrough profile can be seen for feeds with CO_2 concentration of 0.4 mBar, 1 mBar and 5 mBar. Corresponding times for

the first and second shocks and the breakthrough profiles are shown in the Table 5.3 and a good match was obtained between simulated breakthrough profile and wave theory prediction.

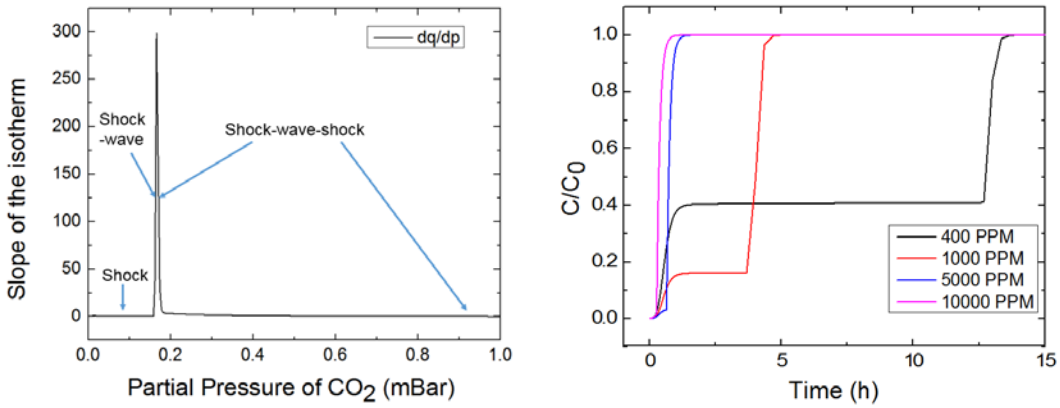

Figure 5.8 (left) Slope of the isotherm for mmen-Mg_2(dobpdc) at 23 °C as a function partial pressure of CO_2. Normalized CO_2 concentration at the exit of the bed vs time (h)(right) predicted by the model for CO_2 concentration of 400 PPM, 1000 PPM, 5000 PPM and 10000 PPM. Simulations were carried out at the flow rate of 28.2 mL/min at 23°C.

Table 5.3 Expected shock-1 and shock-2 times based on the wave theory analysis for the feed flowrate of 28.2 mL/min.

Concentration	Shock 1	Shock 2
400 PPM	29 min	728 min
1000 PPM	29 min	236 min
5334 PPM	29 min	40 min
1000 PPM	21 min	21 min

5.3.4 Breakthrough adsorption experiments for feeds with different concentrations of CO_2

Breakthrough adsorption experiments for a packed bed with the parameters outlined in Table 5.1 were performed at various concentrations, flowrates, and temperatures. Figure 5.9 presents the normalized breakthrough adsorption data at the feed flowrate of 28.2 mL/min and various CO_2 concentrations. It can be seen that a first breakthrough is achieved in a relatively short time, followed by a wave for feeds with CO_2 partial pressures of 0.4 mBar, 1 mBar and 5334 mBar. Second shocks for feeds with 0.4 mBar and 1 mBar were observed to spread out over a longer time period, in contrast to the predictions of the wave theory. Interestingly, the wave plateau concentrations were observed to be higher than from predictions based on equilibrium considerations. This suggests kinetic limitations, which have been further investigated and discussed in the sections below. Almost no wave was observed for the breakthrough profile of the feed with a CO_2 partial pressure of 1 mBar. These results are consistent with the type of the breakthrough expected from predictions of the wave theory.

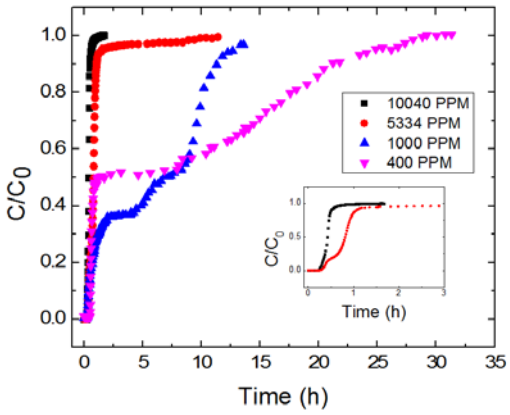

Figure 5.9. Normalized breakthrough concentration profile at a feed flowrate of 28.2 mL/min and various CO_2 concentrations.

A sharp breakthrough curve is expected to improve the utilization of the bed. CO_2 capture from point sources such as coal or gas-fired power plants is typically operated as a purification process, where the operation of the bed is stopped when the effluent concentration of CO_2 is more than a fraction, for example perhaps 5%, of the feed concentration. The length of unused bed (LUB) or the fraction of the bed used (FBU) at the breakthrough are some of the parameters that are used to compare the efficiency of different adsorbent systems. A high FBU or low LUB results from a narrow mass transfer zone. On the other hand, direct air capture of CO_2 is expected to be performed as an extraction operation,[54] with the actual fraction of CO_2 extracted from the feed stream decided based on the corresponding process economics rather than regulatory constraints. Quite often, the goal of operation is to reduce otherwise long cycle times by saturating and desorbing the CO_2 relatively quickly, even at the cost of a decrease in the fraction of CO_2 captured from the feed. To understand the bed utilization and fraction of CO_2 captured the fraction of bed utilized (FBU) can be calculated based on the dynamic capacity at the first shock as a fraction of the total capacity of the bed at the saturation. This parameter is indicative of how efficiently the bed is utilized for each flowrate and concentration. The other metric that has been considered is the overall fraction of CO_2 captured when the CO_2 concentration at the exit of the bed is 95% of the feed concentration. For an equilibrium process, an adsorbent particle is in perfect equilibrium with the nearby gas and hence the fraction of CO_2 captured will be in agreement with predictions from the model. When kinetic limitations are present, additional parameters such mass transfer rates will limit the overall CO_2 capture fraction. Table 5.4 lists the fraction of bed used (FBU values) at the

breakthrough along with the overall CO_2 capture fraction when 95% of CO_2 concentration is detected in the effluent. A short first shock followed by a long wave leads to a poor utilization of the bed for feeds with a CO_2 partial pressure of 0.4 mBar or 1 mBar. As the breakthrough curve sharpens for higher concentrations of CO_2, the FUB and CO_2 capture fractions increases. It should also be noted that the experimental CO_2 capture fraction is lower than the theoretical values suggesting kinetic limitations.

Breakthrough adsorption experiments were conducted at a CO_2 partial pressure of 0.4 mBar and different flowrates. The resultant breakthrough profiles are shown in Figure 5.10. A typical shock-wave-shock breakthrough profile has three important features, (i) the time of the first shock, (ii) the plateau concentration for the wave, and (iii) the profile spread for the second shock. As expected, the breakthrough time for the first shock decreased as the flowrate of the gas mixture in the bed increased. Unexpectedly, the plateau concentration for the wave also increased, indicating non-equilibrium behavior. In case of fast adsorption of CO_2, the plateau concentration is expected to be equilibrium-limited and hence at the effluent concentration corresponding to P_{step} for that particular temperature. For a concentration front entering the bed at 0.4 mBar, the concentration decreases as the bed adsorbs CO_2 and because of the step in the isotherm, a gas mixture with a partial pressure of less than P_{step} will slip through the bed without any adsorption.

Table 5.4 Fraction of bed used (FBU) at the breakthrough and overall CO_2 capture fraction for the feed flow rate of 28.2 mL/min and various concentrations.

Concentration/partial pressure of CO_2	FBU	CO_2 Capture Fraction	Theoretical CO_2 Capture Fraction
400 PPM/0.4 mBar	6.11%	33 %	59%
1000 PPM/ 1 mBar	7.3%	46 %	65%
5334 PPM/ 5.3 mBar	22 %	58 %	97%
10040 PPM/ 1.04 mBar	37 %	64 %	98%

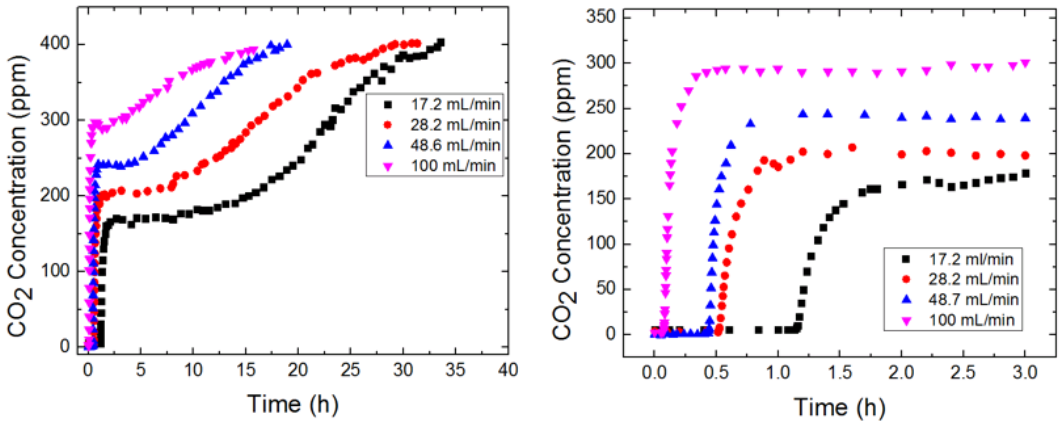

Figure 5.10. Breakthrough adsorption experiments performed at 23 °C with the feed containing CO_2 at the partial pressure of 0.4 mBar and different flowrates of 17.2 mL/min, 28.2 mL/min, 48.6 mL/min, and 100 mL/min. Figure on the left shows full breakthrough profile while the figure on the right shows breakthrough profiles for first 3 hours.

The expected shock-wave-shock breakthrough behavior is most prominent at lower flowrates and subsequently, the breakthrough profile broadens for higher flowrates. This has important implications for process design applications. Table 5.5 lists the FBU and CO_2 capture fraction for different flowrates at 400 PPM and 23 °C. As the flowrates are increased from 17.2 mL/min to 100 mL/min, the CO_2 capture fraction decreased from 43% to 18%, while time needed to saturate the adsorbent also decreased. Again, experimental CO_2 capture fraction was less than theoretical CO_2 capture fraction. The dynamic

adsorption capacities achieved for each flowrate were similar, all being ~2.8 mmol/g. The CO_2 adsorption profiles at temperatures of 23 °C, 49 °C, and 70 °C are presented in Figure 5.11 for the flowrate of 28.2 mL/min and 0.4 mBar partial pressure. As the P_{step} is expected to be beyond 0.4 mBar for both 49 °C and 70 °C, a shock-wave-shock breakthrough profile was not observed. The breakthrough profile at 23 °C is shown only in the initial range to highlight the differences between the profiles at different temperatures.

Table 5.5 FBU and CO_2 Capture Fraction for the bed at different flowrates

Flowrate	FBU	Experimental CO_2 Capture Fraction	Dynamic Breakthrough Capacities	Theoretical CO_2 Capture Fraction
17.2 mL/min	7.79%	43 %	2.77 mmol/g	59%
28.2 mL/min	6.11%	33 %	2.90 mmol/g	59%
48.6 mL/min	8.4%	28 %	2.78 mmol/g	59%
100 mL/min	2.5%	18 %	2.85 mmol/g	59%

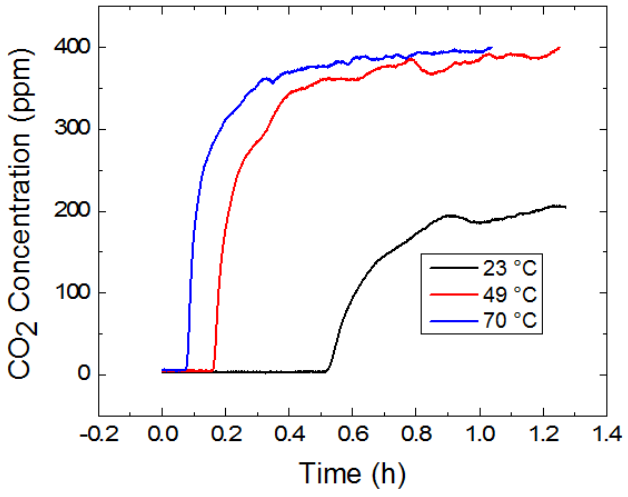

Figure 5.11. CO_2 Breakthrough profile at 23 °C, 49 °C and 70 °C for the feed partial pressure of 0.4 mBar and a flowrate of 28.2 mL/min.

5.3.5 Development of a kinetic model of CO_2 adsorption in mmen-Mg_2(dobpdc)

A kinetic model accounting for diffusive transport, convective transport and accumulation of CO_2 inside the bed was subsequently developed. Accumulation of CO_2 inside a particle is modeled using a linear driving force model. As shown in Figure 5.12, the breakthrough adsorption profiles for different flowrates were simulated at the feed partial pressure of 0.4 mBar and 23 °C using a single linear driving force model. For all flowrates, the same plateau concentration and sharp shocks were predicted by the model. As one can see, a single linear driving force parameter model fails to explain a few key features of the experimentally obtained breakthrough profiles namely, the plateau concentration and the second shock. Further understanding of the system can be developed by understanding the cooperativity that leads to a sharp sigmoidal isotherm. Such cooperative transitions have been observed in a few biological systems. One such example is oxygen uptake by hemoglobin.[55,56] In positive cooperative uptake, the binding of second molecule to a multisite substrate is much faster than the binding of the first molecule, leading to an increase in uptake over a narrow concentration range. Substrates or materials having multiple binding sites demonstrate a very sharp sigmoidal isotherm. The nature of the cooperativity can be analyzed based on a Hill plot.[56] In such a plot, a slope of greater than one at the origin indicates cooperative behavior. Based on the experimental adsorption isotherm in Figure 5.5, a Hill plot was drawn and is depicted in Figure C.2. The slope of the isotherm at the origin is 23, indicating a strong cooperative binding.

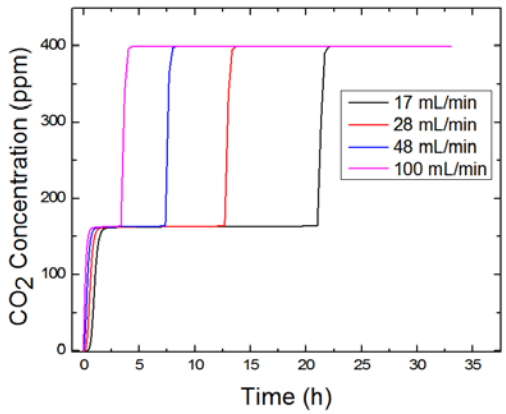

Figure 5.12 Simulated breakthrough profiles for adsorption at 23 °C with the feed containing CO_2 at the partial pressure of 0.4 mBar and different flowrates of 17.2 mL/min, 28.2 mL/min, 48.6 mL/min, and 100 mL/min.

At low partial pressures below the step, a small uptake in CO_2 adsorption in mmen-Mg_2(dobpdc) follows ammonium carbamate formation, which has 2:1 amine-CO_2 stoichiometry.[57] At higher pressures beyond the P_{step}, cooperative insertion of CO_2 leads to the saturation of amine sites over a small change in the CO_2 partial pressure. Cooperative insertion of CO_2 follows 1:1 amine-CO_2 stoichiometry.[13,14,57] These two processes are modeled as follows:

Reaction 1 for ammonium carbamate pathway at partial pressure below the step pressure:

$$\frac{\partial q_1}{\partial t} = k_{ldf_1}\left(q_1^{eq} - q_1\right) \tag{8}$$

Reaction 2 for the cooperative CO_2 insertion pathway occurring at higher partial pressures after the step pressure.

$$\frac{\partial q_2}{\partial t} = k_{forward}\left(q_2^{eq} - q_2\right) * C_{CO_2}^{n} \tag{9}$$

where q_1^{eq} and q_2^{eq} are the saturation capacities, q_L^{∞} & q_U^{∞} , used in the isotherm model, respectively, k_{ldf1} is the rate constant of ammonium carbamate formation and $k_{forward}$ is the rate at which cooperative insertion of CO_2 occurs.

Simulated breakthrough profiles were obtained as shown Figure C3 and 5.13 for different cases. As shown in the Figure 5.13 and Figure C.3, hybrid model has a better fit for the data and explains many characteristics of the breakthrough curve. More specifically, it has a better prediction for the first shock and the dispersive wave concentration. Linear driving force model accounting for the ammonium carbamate pathway with a low equilibrium loading directly affects the first breakthrough. Second part of the hybrid model accounting for the insertion reaction affects the wave concentration as well as second shock. It is found that the LDF model with zero and first order rate dependence with respect CO_2 predicted the change in the wave concentration (Figure C.3) as a function of the flowrate but a deviation from the experimental data was still observed for the breakthrough profile after the first shock. Figure 5.13 presents the data for the LDF model with a second order rate dependence with respect CO_2. As seen from the Figure 5.13, the model is consistent with the experimental data for the first breakthrough and the wave concentration (Figure 5.13 right) and a better prediction is obtained for the breakthrough profile after the first shock than models with zero and first order rate dependence on CO_2. An LDF model with order 3 (Figure C.4) predicts both wave concentration and

breakthrough profile after the first shock with a better consistency but it does not have an appropriate physical justification.

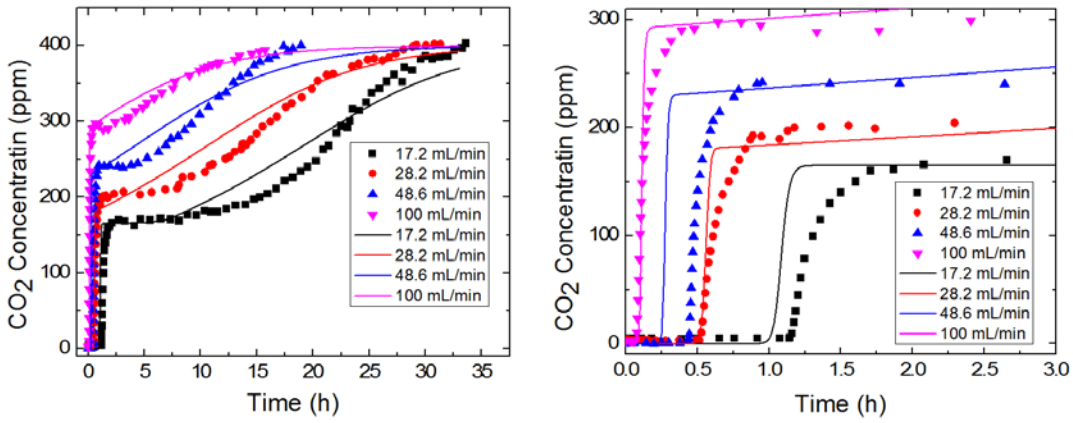

Figure 5.13 Experimental (scatter) and simulated breakthrough profiles (solid lines) for CO_2 adsorption with the CO_2 partial pressure of 0.4 mBar in the feed. Simulated profiles were obtained at the flowrate of 17.2 mL/min, 28.2 mL/min, 48.6 mL/min and 100 mL/min at 23 °C. Linear driving force model with a second order rate dependence to CO_2 concentration was used in this analysis to account the cooperative CO_2 binding.

Corresponding rate constants for two reactions in our hybrid model are presented in Table 5.6. It can be seen that rate constant for LDF model that accounts for the cooperative insertion of CO_2 is almost 1000 times smaller for zero order model. This highlights a difference in the relative rates of two reactions in the hybrid model and their effects on the resultant breakthrough curve. However, a complete characterization of the breakthrough profile is not possible with just one LDF or two LDF models and the rate equation for the CO_2 uptake was further explored through TGA uptake studies. It offered further insights about the kinetics of CO_2 adsorption. A typical TGA uptake for mmen-

Mg_2(dobpdc) is shown in Figure 5.14 where adsorption proceeds with relatively fast but a small initial uptake followed by a slow uptake leading to the saturation.

Table 5.6 Rate constants used to simulate adsorption of CO_2 using LDF in the hybrid model.

Rate constant in LDF for ammonium carbamate mechanism before CO_2 insertion.	Rate law order with respect to CO_2 in LDF for cooperative CO_2 insertion.	Rate constant in LDF for the cooperative CO_2 insertion.
$2.45 * 10^{-2}$ sec^{-1}	0	$2.38*10^{-5}$ sec^{-1}
$2.45 * 10^{-2}$ sec^{-1}	1	$2.14*10^{-3}$ $m^3/mol/sec^{-1}$
$2.45 * 10^{-2}$ sec^{-1}	2	$1.88*10^{-1}$ $(m^3/mol)^2/sec^{-1}$
$2.45 * 10^{-2}$ sec^{-1}	3	1.86 $(m^3/mol)^3/ sec^{-1}$

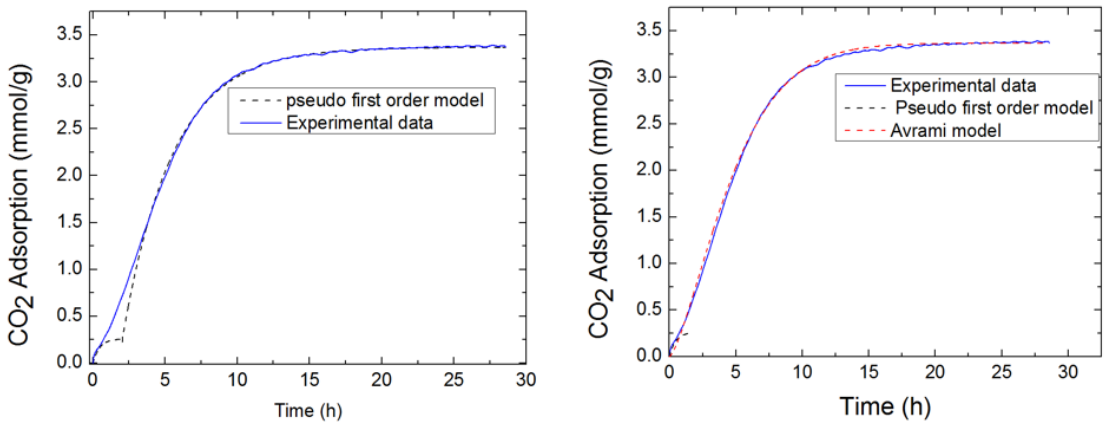

Figure 5.14 CO_2 uptake (blue solid line) on TGA for a typical sample of mmen-Mg_2(dobpdc). As shown in the figure on the left, one single pseudo first order LDF uptake model (black) is not sufficient to model the entire uptake. As shown in the figure on the right, a hybrid model with pseudo first order model (black) for the initial uptake and avrami model (red) for the subsequent uptake fits the data well.

Figure 5.14 left demonstrates the experimental data (solid blue line) and predictions from a hybrid model that consists of two pseudo first order models (dotted black line). Initial part of the uptake was fitted with an LDF model corresponding to a low equilibrium capacity and later part was fitted with an LDF model corresponding to a high equilibrium capacity. As it can be seen, a hybrid model with two LDFs is not sufficient to model CO_2 uptake on a TGA. This can be further explained by the mechanism of CO_2 capture in mmen-Mg_2(dobpdc) (equations C16-C27). Although the mechanism of CO_2 insertion (equations C28) suggests a single rate process CO_2 for insertion, the actual uptake can be visualized as a combination of different processes happening simultaneously. A single CO_2 molecule can be inserted in the framework on a single site to start the chain reaction or as a part of the chain that has already formed and both of these uptakes are expected to run at different rates. Net CO_2 adsorption is a combination of these two processes whereby initial uptake is dominated by CO_2 insertion onto single sites. This particular type of CO_2 adsorption can be modeled by Avrami's fractional order rate equation.

$$\frac{\partial q_2}{\partial t} = k_A^{n_A} t^{n_A - 1}(q_2^* - q_2) \qquad (10)$$

Where k_A, t, $\boldsymbol{q_2^*}$, n_A are rate constant, time, saturation capacity, and Avrami fractional constant respectively. Predictions from the hybrid model that consists of pseudo first order and Avrami model are shown in the Figure 15.4 right. Values obtained for k_A and n_A are $5.42*10^{-5}$ s^{-1} and 1.5 respectively indicating a slow and mixed mode of adsorption. The model used here has an approximate physical justification but it captures many features of this complex system and points out to certain important features that need

to be studied in more details. Further in-situ experimental results at ultra-dilute concentrations supplemented with modeling will enable an improved understanding of the system.

5.4 Conclusions

Mmen-Mg_2(dobpdc) has shown an unprecedented high adsorption capacities and high amine-efficiencies at ultra-low partial pressures of CO_2. The system shows a stepped isotherm that is tunable based on the temperature. CO_2 adsorption in mmen-Mg_2(dobpdc) is studied for ultra-dilute conditions using a breakthrough adsorption setup as a proxy for practical flow systems. Dynamic CO_2 adsorption experiments were carried out at various flow rates, temperature and concentrations. The development of the breakthrough profile was analyzed using the equilibrium wave theory. Equilibrium wave theory suggested different types of breakthrough profiles based on the feed concentration. This was confirmed through experiments where a shock-wave-shock breakthrough was observed in experiments for feed concentration corresponding to DAC. A shock breakthrough was observed for CO_2 concentrations above 1%. A significant deviation was observed in adsorption experiments at higher flowrates with the feed concentration of 400 PPM corresponding to DAC. The breakthrough adsorption was further understood through a kinetic model that accounted for two different reaction mechanisms in the system namely, ammonium carbamate formation and cooperative CO_2 insertion. It was found that the hybrid rate law that consists of pseudo first order and avrami model has a better prediction for the CO_2 TGA uptake. The system performance was further characterized through the fractional bed usage (FBU) and the fraction of CO_2 captured at the saturation. It is found

that kinetic factors severely reduce CO_2 capture fraction at low concentrations reducing the viability of mmen-Mg_2(dobpdc) for practical DAC applications. Improved FBU and fraction of CO_2 captures makes it more suitable for adsorption applications where CO_2 concentration in the feed is more than 1%.

5.5 References

1. Jones, C. W. CO_2 Capture from Dilute Gases as a Component of Modern Global Carbon Management. *Annu. Rev. Chem. Biomol. Eng.* **2011**, 2, 31–52.

2. Lackner, K. S.; Brennan, S.; Matter, J. M.; Park, A. H.; Wright, A.; van der Zwaan, B. The Urgency of the Development of CO_2 Capture from Ambient Air. *Proc Natl Acad Sci U S A* **2012**, 109 (33), 13156–13162.

3. Sanz-Pérez, E. S.; Murdock, C. R.; Didas, S. A.; Jones, C. W. Direct Capture of CO_2 from Ambient Air. *Chem. Rev.* **2016**, 116 (19), 11840–11876.

4. Belmabkhout, Y.; Serna-Guerrero, R.; Sayari, A. Amine-Bearing Mesoporous Silica for CO_2 Removal from Dry and Humid Air. *Chem. Eng. Sci.* **2010**, 65 (11), 3695–3698.

5. Choi, S.; Drese, J. H.; Eisenberger, P. M.; Jones, C. W. Application of Amine-Tethered Solid Sorbents for Direct CO_2 Capture from the Ambient Air. *Environ. Sci. Technol.* **2011**, 45 (6), 2420–2427.

6. Wang, J.; Wang, M.; Zhao, B.; Qiao, W.; Long, D.; Ling, L. Mesoporous Carbon-Supported Solid Amine Sorbents for Low-Temperature Carbon Dioxide Capture. *Ind. Eng. Chem. Res.* **2013**, 52 (15), 5437–5444.

7. Sumida, K.; Rogow, D. L.; Mason, J. a; McDonald, T. M.; Bloch, E. D.; Herm, Z. R.; Bae, T.-H.; Long, J. R. Carbon Dioxide Capture in Metal-Organic Frameworks. *Chem. Rev.* **2012**, 112 (2), 724–781.

8. Darunte, L. A.; Walton, K. S.; Sholl, D. S.; Jones, C. W. CO_2 Capture via Adsorption in Amine-Functionalized Sorbents. *Curr. Opin. Chem. Eng.* **2016**, 12.

9. Darunte, L. A.; Oetomo, A. D.; Walton, K. S.; Sholl, D. S.; Jones, C. W. Direct Air Capture of CO_2 Using Amine Functionalized MIL-101(Cr). *ACS Sustain. Chem. Eng.* **2016**, 4 (10), 5761–5768.

10. McDonald, T. M.; Lee, W. R.; Mason, J. A.; Wiers, B. M.; Hong, C. S.; Long, J. R. Capture of Carbon Dioxide from Air and Flue Gas in the Alkylamine-Appended Metal-Organic Framework Mmen-Mg_2(dobpdc). *J. Am. Chem. Soc.* **2012**, 134 (16), 7056–7065.

11. Choi, S.; Watanabe, T.; Bae, T.-H.; Sholl, D. S.; Jones, C. W. Modification of the Mg/DOBDC MOF with Amines to Enhance CO_2 Adsorption from Ultradilute Gases. *J. Phys. Chem. Lett.* **2012**, 3 (9), 1136–1141.

12. McDonald, T. M.; Lee, W. R.; Mason, J. A.; Wiers, B. M.; Hong, C. S.; Long, J. R. Capture of Carbon Dioxide from Air and Flue Gas in the Alkylamine-Appended Metal–Organic Framework Mmen-Mg_2(dobpdc). *J. Am. Chem. Soc*. **2012**, 134 (16), 7056–7065.

13. Siegelman, R. L.; McDonald, T. M.; Gonzalez, M. I.; Martell, J. D.; Milner, P. J.; Mason, J. A.; Berger, A. H.; Bhown, A. S.; Long, J. R. Controlling Cooperative CO_2 Adsorption in Diamine-Appended Mg_2(dobpdc) Metal–Organic Frameworks. *J. Am. Chem. Soc.* **2017**, 139 (30), 10526–10538.

14. Mcdonald, T. M.; Mason, J. A.; Kong, X.; Bloch, E. D.; Gygi, D.; Dani, A.; Crocellà, V.; Giordanino, F.; Odoh, S. O.; Drisdell, W. S.; et al. Cooperative Insertion of CO_2 in Diamine- Appended Metal-Organic Frameworks. *Nature* **2015,** 519, 303–308

15. Lee, W. R.; Hwang, S. Y.; Ryu, D. W.; Lim, K. S.; Han, S. S.; Moon, D.; Choi, J.; Hong, C. S. Diamine-Functionalized Metal–organic Framework: Exceptionally High CO_2 Capacities from Ambient Air and Flue Gas, Ultrafast CO_2 Uptake Rate, and Adsorption Mechanism. *Energy Environ. Sci.* **2014**.

16. Darunte, L. A.; Terada, Y.; Murdock, C. R.; Walton, K. S.; Sholl, D. S.; Jones, C. W. Monolith-Supported Amine-Functionalized Mg_2(dobpdc) Adsorbents for CO_2 Capture. *ACS Appl. Mater. Interfaces* **2017**.

17. Labreche, Y.; Lively, R. P.; Rezaei, F.; Chen, G.; Jones, C. W.; Koros, W. J. Post-Spinning Infusion of Poly(ethyleneimine) into Polymer/silica Hollow Fiber Sorbents for Carbon Dioxide Capture. *Chem. Eng. J.* **2013**, 221, 166–175.

18. Lively, R. P.; Chance, R. R.; Kelley, B. T.; Deckman, H. W.; Drese, J. H.; Jones, C. W.; Koros, W. J. Hollow Fiber Adsorbents for CO_2 Removal from Flue Gas. *Ind. Eng. Chem. Res.* **2009**, 48 (15), 7314–7324.

19. Maserati, L.; Meckler, S. M.; Bachman, J. E.; Long, J. R.; Helms, B. A. Diamine-Appended Mg_2(dobpdc) Nanorods as Phase-Change Fillers in Mixed-Matrix Membranes for Efficient CO_2/N_2 Separations. *Nano Lett.* **2017**, 17 (11), 6828–6832.

20. Mueller, R.; Kanungo, R.; Kiyono-Shimobe, M.; Koros, W. J.; Vasenkov, S. Diffusion of Methane and Carbon Dioxide in Carbon Molecular Sieve Membranes by Multinuclear Pulsed Field Gradient NMR. *Langmuir* **2012**, 28 (27), 10296–10303.

21. Déroche, I.; Maurin, G.; Borah, B. J.; Yashonath, S.; Jobic, H. Diffusion of Pure CH4 and Its Binary Mixture with CO_2 in Faujasite NaY: A Combination of Neutron Scattering Experiments and Molecular Dynamics Simulations. *J. Phys. Chem. C* **2010**, 114 (11), 5027–5034.

22. Kärger, J.; Ruthven, D. M.; Theodorou, D. N. Imaging of Transient Concentration Profiles. In Diffusion in Nanoporous Materials; Wiley-VCH Verlag GmbH & Co. KGaA, **2012**; pp 395–426.

23. Chmelik, C.; Heinke, L.; Kortunov, P.; Li, J.; Olson, D.; Tzoulaki, D.; Weitkamp, J.; Kärger, J. Ensemble Measurement of Diffusion: Novel Beauty and Evidence. *ChemPhysChem* **2009**, 10 (15), 2623–2627.

24. Tanaka, S.; Fujita, K.; Miyake, Y.; Miyamoto, M.; Hasegawa, Y.; Makino, T.; Van der Perre, S.; Cousin Saint Remi, J.; Van Assche, T.; Baron, G. V; et al. Adsorption and Diffusion Phenomena in Crystal Size Engineered ZIF-8 MOF. *J. Phys. Chem. C* ***2015***, 119 (51), 28430–28439.

25. Brandani, F.; Ruthven, D.; Coe, C. G. Measurement of Adsorption Equilibrium by the Zero Length Column (ZLC) Technique Part 1: Single-Component Systems. Ind. *Eng. Chem. Res.* **2003**, 42 (7), 1451–1461.

26. Tovar, T. M.; Zhao, J.; Nunn, W. T.; Barton, H. F.; Peterson, G. W.; Parsons, G. N.; LeVan, M. D. Diffusion of CO_2 in Large Crystals of Cu-BTC MOF. *J. Am. Chem. Soc*. **2016**, 138 (36), 11449–11452.

27. Kärger, J.; Ruthven, D. M.; Theodorou, D. N. Measurement of Elementary Diffusion Processes. In Diffusion in Nanoporous Materials; Wiley-VCH Verlag GmbH & Co. KGaA, **2012**; pp 303–345.

28. Ho, Y.-S. Review of Second-Order Models for Adsorption Systems. J. *Hazard. Mater.* **2006**, 136 (3), 681–689.

29. Heydari-Gorji, A.; Sayari, A. CO_2 Capture on Polyethylenimine-Impregnated Hydrophobic Mesoporous Silica: Experimental and Kinetic Modeling. *Chem. Eng. J.* **2011**, 173 (1), 72–79.

30. Serna-Guerrero, R.; Sayari, A. Modeling Adsorption of CO_2 on Amine-Functionalized Mesoporous Silica. 2: Kinetics and Breakthrough Curves. *Chem. Eng. J.* **2010**, 161 (1), 182–190.

31. Avrami, M. Kinetics of Phase Change. I General Theory. J. Chem. Phys. **1939**, 7 (12), 1103–1112.

32. Liu, Q.; Shi, J.; Zheng, S.; Tao, M.; He, Y.; Shi, Y. Kinetics Studies of CO_2 Adsorption/Desorption on Amine-Functionalized Multiwalled Carbon Nanotubes. *Ind. Eng. Chem. Res.* **2014**, 53 (29), 11677–11683.

33. Wang, X.; Guo, Q.; Kong, T. Tetraethylenepentamine-Modified MCM-41/silica Gel with Hierarchical Mesoporous Structure for CO_2 Capture. *Chem. Eng. J.* **2015**, 273, 472–480.

34. Zhao, A.; Samanta, A.; Sarkar, P.; Gupta, R. Carbon Dioxide Adsorption on Amine-Impregnated Mesoporous SBA-15 Sorbents: Experimental and Kinetics Study. *Ind. Eng. Chem. Res.* **2013**, 52 (19), 6480–6491.

35. Liu, F.; Chen, S.; Gao, Y.; Xie, Y. CO_2 Adsorption Behavior and Kinetics on Polyethylenimine Modified Porous Phenolic Resin. *J. Porous Mater.* **2017**, 24 (5), 1335–1342.

36. Ebner, A. D.; Gray, M. L.; Chisholm, N. G.; Black, Q. T.; Mumford, D. D.; Nicholson, M. A.; Ritter, J. A. Suitability of a Solid Amine Sorbent for CO_2

Capture by Pressure Swing Adsorption. Ind. Eng. Chem. Res. **2011**, 50 (9), 5634–5641.

37. Abdollahi-Govar, A.; Ebner, A. D.; Ritter, J. A. New Kinetic Model That Describes the Reversible Adsorption and Desorption Behavior of CO_2 in a Solid Amine Sorbent. *Energy & Fuels* **2015**, 29 (7), 4492–4502.

38. Suh, D.-M.; Sun, X. Particle-Scale CO_2 Adsorption Kinetics Modeling Considering Three Reaction Mechanisms. *Int. J. Greenh. Gas Control* **2013**, 17, 388–396.

39. Jung, W.; Park, J.; Lee, K. S. Kinetic Modeling of CO_2 Adsorption on an Amine-Functionalized Solid Sorbent. *Chem. Eng. Sci.* **2018**, 177, 122–131.

40. Bollini, P.; Brunelli, N. A.; Didas, S. A.; Jones, C. W. Dynamics of CO_2Adsorption on Amine Adsorbents. 2. Insights Into Adsorbent Design. *Ind. Eng. Chem. Res.* **2012**, 51 (46), 15153–15162.

41. Glueckauf, E. Theory of Chromatography: VII. The General Theory of Two Solutes Following Non-Linear Isotherms. Discuss. *Faraday Soc.* **1949**, 7, 12–25.

42. Yang, R. T. CHAPTER 5 - Adsorber Dynamics: Bed Profiles and Breakthrough Curves BT - Gas Separation by Adsorption Processes; *Butterworth-Heinemann*, **1987**; pp 141–200.

43. Mazzotti, M.; Rajendran, A. Equilibrium Theory–Based Analysis of Nonlinear Waves in Separation Processes. *Annu. Rev. Chem. Biomol. Eng.* **2013**, 4 (1), 119–141.

44. Yun, J.-H. Unusual Adsorber Dynamics due to S-Shaped Equilibrium Isotherm. Korean *J. Chem. Eng.* **2000**, 17 (5), 613–617.

45. Inglezakis, V. J.; Fyrillas, M. M. Adsorption Fixed Beds Modeling Revisited: Generalized Solutions for S-Shaped Isotherms. *Chem. Eng. Commun*. **2017**, 204 (11), 1299–1317.

46. Schweich, D.; Sardin, M. Adsorption, Partition, Ion Exchange and Chemical Reaction in Batch Reactors or in Columns — *A Review. J. Hydrol.* **1981**, 50, 1–33.

47. Milner, P. J.; Siegelman, R. L.; Forse, A. C.; Gonzalez, M. I.; Runčevski, T.; Martell, J. D.; Reimer, J. A.; Long, J. R. A Diaminopropane-Appended Metal–Organic Framework Enabling Efficient CO_2 Capture from Coal Flue Gas via a Mixed Adsorption Mechanism. *J. Am. Chem. Soc*. **2017**, 139 (38), 13541–13553.

48. Bozbiyik, B.; Van Assche, T.; Lannoeye, J.; De Vos, D. E.; Baron, G. V; Denayer, J. F. M. Stepped Water Isotherm and Breakthrough Curves on Aluminium Fumarate Metal–organic Framework: Experimental and Modelling Study. *Adsorption* **2017**, 23 (1), 185–192.

49. Schoenecker, P. M.; Carson, C. G.; Jasuja, H.; Flemming, C. J. J.; Walton, K. S. Effect of Water Adsorption on Retention of Structure and Surface Area of Metal–Organic Frameworks. *Ind. Eng. Chem. Res.* **2012**, 51 (18), 6513–6519.

50. Cousin-Saint-Remi, J.; Denayer, J. F. M. Applying the Wave Theory to Fixed-Bed Dynamics of Metal-Organic Frameworks Exhibiting Stepped Adsorption Isotherms: Water/ethanol Separation on ZIF-8. *Chem. Eng. J.* **2017**, 324, 313–323.

51. Darunte, L. A.; Terada, Y.; Murdock, C. R.; Walton, K. S.; Sholl, D. S.; Jones, C. W. Monolith-Supported Amine-Functionalized Mg_2(dobpdc) Adsorbents for CO_2 Capture. *ACS Appl. Mater. Interfaces 2017*, 9 (20), 17042–17050.

52. Hefti, M.; Joss, L.; Bjelobrk, Z.; Mazzotti, M. On the Potential of Phase-Change Adsorbents for CO_2 Capture by Temperature Swing Adsorption. *Faraday Discuss.* **2016**, 192 (0), 153–179.

53. Wakao, N.; Kaguei, S.; Funazkri, T. Effect of Fluid Dispersion Coefficients on Particle-to-Fluid Heat Transfer Coefficients in Packed Beds: Correlation of Nusselt Numbers. *Chem. Eng. Sci.* **1979**, 34 (3), 325–336.

54. Sinha, A.; Darunte, L. A.; Jones, C. W.; Realff, M. J.; Kawajiri, Y. Systems Design and Economic Analysis of Direct Air Capture of CO_2 through Temperature Vacuum Swing Adsorption . *Ind. Eng. Chem.Res.* **2016**.

55. Eaton, W. A.; Henry, E. R.; Hofrichter, J.; Mozzarelli, A. Is Cooperative Oxygen Binding by Hemoglobin Really Understood? *Nat. Struct. Biol.* **1999**, 6, 351.

56. Hunter, C. A.; Anderson, H. L. What Is Cooperativity? *Angew. Chemie Int. Ed.* **2009**, 48 (41), 7488–7499.

57. Wu, D.; McDonald, T. M.; Quan, Z.; Ushakov, S. V; Zhang, P.; Long, J. R.; Navrotsky, A. Thermodynamic Complexity of Carbon Capture in Alkylamine-Functionalized Metal–organic Frameworks. *J. Mater. Chem.* A **2015**, 3 (8), 4248–4254.

6 CONCLUSION AND FUTURE WORK IDEAS

6.1 Conclusions

The following is summary of the dissertation along with main conclusions from each chapter:

6.1.1 Chapter 1

CO_2 adsorption in amine-functionalized sorbents is discussed with a focus on MOF materials. The discussion focused on the mechanism of CO_2 adsorption, different ways to functionalize MOFs with amines, mmen-Mg_2(dobpdc)[1] as a recent system with a promising performance for CO_2 capture and system design. Critical research needs are also identified for engineering demonstrations of adsorbents in the form of low-pressure drop configuration as well as the kinetics of CO_2 adsorption.

6.1.2 Chapter 2

MIL-101(Cr) was chosen for amine-functionalization based on its superior conditions under a variety of conditions[2] and CO_2 adsorption from the simulated air in the resultant amine-functionalized framework was studied. Tris(2-aminoethyl)amine (TREN) and poly(ethyleneimine) (PEI, MW-800) were chosen to functionalize MIL-101(Cr) with amines.

- MIL-101(Cr) functionalized with TREN showed modest CO_2 adsorption from the simulated air with 4% amine efficiency. Similar results obtained by Hu et al.[3] on MIL-101(Cr) functionalized with small amines suggest this approach is not very effective to create a high capacity adsorbent at DAC conditions. Physical impregnation of MIL-101(Cr) with TREN resulted in capacity losses in cyclic temperature swing adsorption on a thermogravimetric analyzer because of leaching of amines.
- MIL-101(Cr) impregnated with PEI showed a better stability in a cyclic temperature swing adsorption process. Both amine efficiency and CO_2 adsorption from the simulated air were found to be a function of PEI loading in MIL-101(Cr). Kinetic limitations are observed at high loadings of PEI.

6.1.3 Chapter 3

Mmen-Mg_2(dobpdc) was chosen for its superior CO_2 adsorption at ultra-dilute conditions. Stability of mmen-Mg_2(dobpdc) after exposure to pure water vapor and liquid water was also investigated. Honeycomb monolithic structure was chosen because of its low pressure drop.

- An oriented growth of Mg_2(dobpdc) was observed following the seeding of a monolith with MgO nanoparticles. It also resulted in long crystallites that can be further explored for the kinetics studies.

- Primary growth with MgO as the precursor and secondary growth in a dilute solution of $Mg(NO_3)_2$ resulted in MOF films which once functionalized with mmen showed ~70% effectiveness compared to mmen-Mg_2(dobpdc) powders.
- Sinha et al.[4] analyzed adsorbents in chapter 2 & 3 for further system design and economic analysis.

6.1.4 Chapter 4

Methods developed in chapter 3 are extended further to grow Mg-MOF-74 for CO_2 adsorption.

- Presence of water was found to create phase-pure Mg-MOF-74 with a faster conversion from MgO to Mg-MOF-74.
- Primary growth with MgO as a precursor and secondary growth in the solution of $Mg(NO_3)_2$ resulted in MOF films showed ~30% effectiveness compared to Mg-MOF-74 powders.

6.1.5 Chapter 5

A packed bed system was constructed to conduct dynamic breakthrough CO_2 adsorption experiments under both humid and dry conditions. Dynamic CO_2 adsorption experiments were conducted at various concentrations and flow rates of CO_2 mixtures corresponding to ultra-dilute conditions.

- Equilibrium wave theory was used to identify different breakthrough profiles resulting from the stepped isotherm of mmen-Mg_2(dobpdc). Stepped isotherm

leads to shock-wave-shock breakthrough for CO_2 capture corresponding to direct air capture conditions.

- Reaction scheme for the cooperative adsorption of CO_2 was developed accounting for two different mass transfer regimes based on the CO_2 concentrations.
- In a collaborative work, dynamic CO_2 adsorption in a packed bed was simulated with results indicating long saturation times and a decrease in the fraction of CO_2 captured by the system at high flowrates because of kinetic limitations.

6.2 Future work

Overall this dissertation has contributed to enhancing the understanding of the community for a practical CO_2 adsorption. It also highlights the need for simultaneous material and process design. Some future work is listed below which is a culmination of many ideas over last few years while working on this thesis.

6.2.1 Shape engineering of MOFs for gas separation and catalysis applications with the use of solid precursors

6.2.1.1 Gas separation applications

Recently Sinha et al.[4] analyzed monolith-supported MOFs for direct air capture. In the analysis, energy penalty associated with the monolith during the desorption step and adsorbents cost turned out to be significant cost components of the system. Both costs can be reduced by paying a close attention to system design. Shape engineering of MOFs is

one area of recent interest where MOFs (or adsorbents in general) are cast in the form of practical substrates such as honeycomb monolith or hollow fibers. This approach is promising because it can lead to high loading of sorbents in the system and hence minimize the deadweight of the system. Adsorbent cost can be reduced further by minimizing the wastage of adsorbent during the shape-engineering, use of metal-rich precursors such as MgO instead of $Mg(NO_3)_2$ and replacing expensive and toxic organic solvents such as DMF, DMSO with relatively benign and cheap solvents such as water and ethanol.

During the shape engineering, solvents used to form the dope or the actual extrusion process can be detrimental to many MOFs that are air or water sensitive in their non-functionalized forms. This problem can be overcome by casting solid precursors such as the MgO in the required shape before conversion to MOFs. I and others[5] have demonstrated that solid MgO to Mg_2(dobpdc) conversion can be tuned to obtain crystals of different lengths for different applications. This approach can also be used to increase weight loading of MOFs in the structure. Additionally, MgO has more Mg content than traditionally used $Mg(NO_3)_2$ which can further reduce the amount of metal precursor needed. Schematic of this approach is outlined in Figure 1 where the expected structure will have thin walls of MgO and MOF needles formed out of those thin walls. The MgO will form the structural backbone imparting mechanical stability to the structure. It can be 3-D printed following recent recipes[6,7] used by Rezaei and Denayer groups.

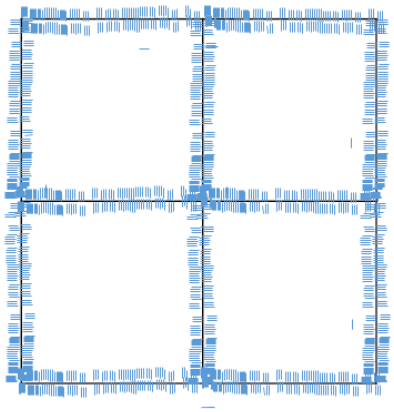

Figure 6.1 Schematic of MgO monolith with an oriented Mg_2(dobpdc) growth on the surface

6.2.1.2 Catalysis applications

There is a widespread interest in MOFs derived carbons for catalysis application as it can offer an optimal dispersion of metal sites. For a practical application, MOFs immobilized on monoliths can also be used as a template for MOF derived carbons in the monolithic form. Additional advantage of this system is many of the MOFs on the monolith can be potentially ion exchanged to create a mixed metal system.[8]

6.2.2 Mechanistic understanding of MOF film growth from solid precursors

6.2.2.1 Rate law of reaction of CO_2 at the amine-site

Chapter 5 described CO_2 adsorption in a fixed be system using both experimental and modeling results. Mcdonald et al.[1] have identified a cooperative mechanism to explain the stepped isotherm. Modeling results suggest that there are two different mass transfer regimes in play in the system. The first regime has fast mass transfer because of ammonium carbamate formation that results in a very small adsorption before the step. Our data suggest that cooperative adsorption that results in high CO_2 adsorption happens at much

slower scale leading to kinetic effects at higher flow rates. Our linear driving force model also suggested that second order dependence on CO_2 concentration has a better fit with the experimental data. However, identification of rate limiting step and determination of appropriate rate law will enhance the understanding of the kinetics of CO_2 adsorption. This further study should involve the identification of key intermediates such as ammonium carbamate in the free as well inserted form via infrared microscopy and their evolution as a function of CO_2 concentration and time. Simultaneously, appropriate models should be development that accounts for different elementary steps. Finally, the data fitting should enable a deeper understanding of the rate law involved during the reaction.

6.2.3 Understanding the effect of various factors on the shape of the isotherm

Diamine-functionalized Mg_2(dobpdc) shows a stepped CO_2 adsorption isotherm that has been attributed to cooperative insertion of CO_2.[1,10] The observed stepped change happens over a very small change in the CO_2 partial pressure. Cooperative adsorption can be analyzed by the Hill equation[11] which takes into account a cooperative binding. In chapter 5, the nature of the cooperativity was analyzed by the slope of the hill plot at the origin indicating a large number of sites involves in the cooperative binding. Our work and others[5] have also observed subtle changes in the slope of the isotherm which may result in widely different breakthrough profile for ultra-dilute concentrations of CO_2. It hypothesized that defects in the structure impacts number of sites involved in the structure. More importantly, different methods of material preparation and processing such pelletization can also have an impact on the number of sites involved in the cooperative

binding. This can be systematically studied by generating CO_2 adsorption isotherms after exposing the material to a variety of conditions as follows.

- Air exposure for a week, a month and 6 months.
- Pelletization at different pressures.
- Material synthesis using a variety of precursors.

6.3 References

(1) Mcdonald, T. M.; Mason, J. A.; Kong, X.; Bloch, E. D.; Gygi, D.; Dani, A.; Crocellà, V.; Giordanino, F.; Odoh, S. O.; Drisdell, W. S.; et al. Cooperative Insertion of CO_2 in Diamine- Appended Metal-Organic Frameworks.

(2) Hong, D.-Y.; Hwang, Y. K.; Serre, C.; Férey, G.; Chang, J.-S. Porous Chromium Terephthalate MIL-101 with Coordinatively Unsaturated Sites: Surface Functionalization, Encapsulation, Sorption and Catalysis. *Adv. Funct. Mater.* **2009**, *19* (10), 1537–1552.

(3) Hu, Y.; Verdegaal, W. M.; Yu, S.-H.; Jiang, H.-L. Alkylamine-Tethered Stable Metal-Organic Framework for CO_2 Capture from Flue Gas. *ChemSusChem* **2014**, *7* (3), 734–737.

(4) Sinha, A.; Darunte, L. A.; Jones, C. W.; Realff, M. J.; Kawajiri, Y. Systems Design and Economic Analysis of Direct Air Capture of CO_2 through Temperature Vacuum Swing Adsorption . *Ind. Eng. Chem.* **2016**.

(5) Maserati, L.; Meckler, S. M.; Bachman, J. E.; Long, J. R.; Helms, B. A. Diamine-Appended Mg_2(dobpdc) Nanorods as Phase-Change Fillers in Mixed-Matrix Membranes for Efficient CO_2/N_2 Separations. *Nano Lett.* **2017**, *17* (11), 6828–6832.

(6) Thakkar, H.; Eastman, S.; Al-Naddaf, Q.; Rownaghi, A. A.; Rezaei, F. 3D-Printed Metal-Organic Framework Monoliths for Gas Adsorption Processes. *ACS Appl. Mater. Interfaces* **2017**, *9* (41), 35908–35916.

(7) Couck, S.; Cousin-Saint-Remi, J.; Van der Perre, S.; Baron, G. V; Minas, C.; Ruch, P.; Denayer, J. F. M. 3D-Printed SAPO-34 Monoliths for Gas Separation. *Microporous Mesoporous Mater.* **2018**, *255*, 185–191.

(8) Wang, L. J.; Deng, H.; Furukawa, H.; Gandara, F.; Cordova, K. E.; Peri, D.; Yaghi, O. M. Synthesis and Characterization of Metal-Organic Framework-74 Containing 2, 4, 6, 8, and 10 Different Metals. *Inorg Chem* **2014**, *53* (12), 5881–5883.

(9) Bonilla, G.; Vlachos, D. G.; Tsapatsis, M. Simulations and Experiments on the Growth and Microstructure of Zeolite MFI Films and Membranes Made by Secondary Growth. *Microporous Mesoporous Mater.* **2001**, *42* (2–3), 191–203.

(10) Siegelman, R. L.; McDonald, T. M.; Gonzalez, M. I.; Martell, J. D.; Milner, P. J.; Mason, J. A.; Berger, A. H.; Bhown, A. S.; Long, J. R. Controlling Cooperative CO_2 Adsorption in Diamine-Appended Mg_2(dobpdc) Metal–Organic Frameworks. *J. Am. Chem. Soc.* **2017**, *139* (30), 10526–10538.

(11) Hunter, C. A.; Anderson, H. L. What Is Cooperativity? *Angew. Chemie Int. Ed.* **2009**, *48* (41), 7488–7499.

APPENDIX A SUPPLEMENTARY INFORMATION TO CHAPTER 2

A.1 Scanning Electron Microscopy

Acetic acid/BDC ratio: 4 Bipyramidal MIL-101(Cr) crystals with crystal size ~ 150-200 nm. A small crystal size for MIL-101(Cr) is expected to aid in the insertion of PEI in the crystals.

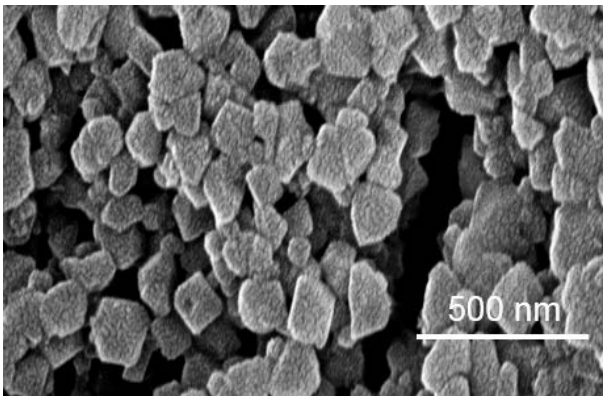

Figure A.1 MIL-101(Cr) crystal size for acetic acid/BDC ratio 4

Acetic acid/BDC ratio: 12.5, Bipyramidal MIL-101(Cr) crystals with crystal size ~ 600-800 nm.

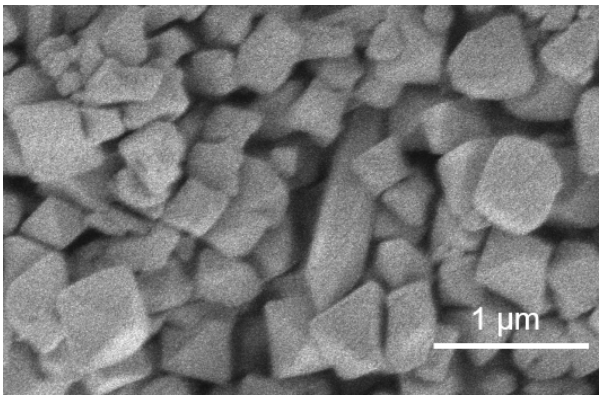

Figure A.2 MIL-101(Cr) crystal size for acetic Acid/BDC ratio 12.5

A.2. Stability of MIL-101-TREN samples for different loadings of TREN

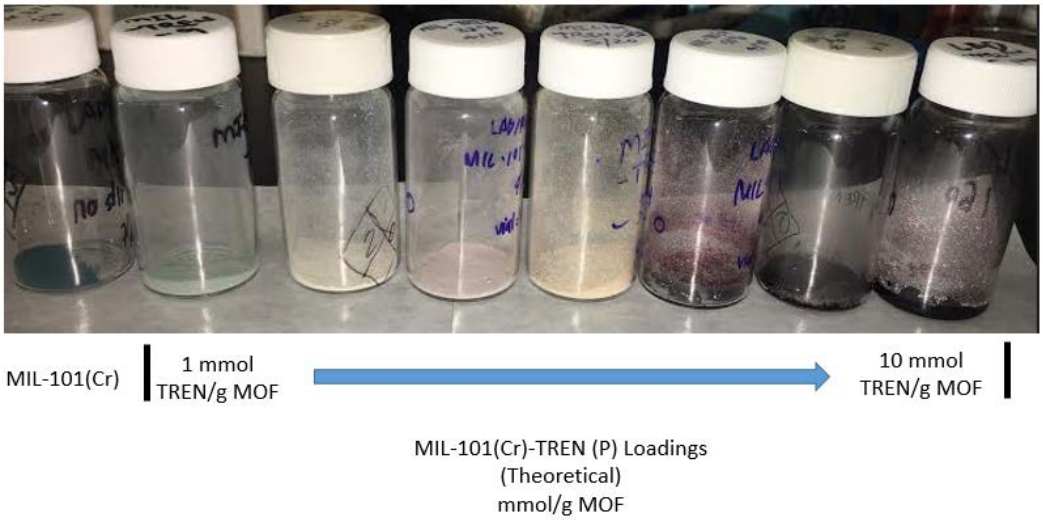

Figure A.3 Degradation of MIL-101(Cr)-TREN samples

MIL-101(Cr)-TREN physically supported samples were observed to degrade after 1 months. As the TREN loading was increased from 1mmol/g MOF to 10 mmol/g MOF, increased instability of the samples was observed. This is hypothesized to be due to a relatively high volatility of TREN. Elemental analysis and N_2 physisorption results for aged

or degassed samples are thus not considered to be reliable because of the high volatility of TREN. Further studies therefore focused on MIL-101(Cr)-PEI-800 materials. No such visual degradation was observed for MIL-101(Cr)-PEI-800 samples for a period of three months.

A.3. XRD of MIL-101 (Cr) and Amine functionalized samples:

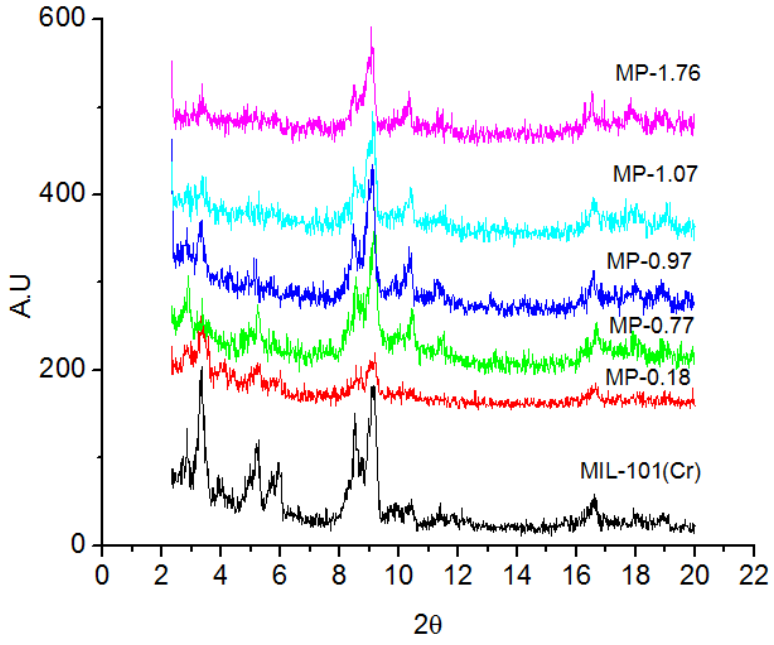

Figure A.4 Powder XRD patterns for MIL-101(Cr) and MIL-101(Cr)-PEI-800. Samples are labelled as MP-XX, M= MIL-101(Cr), P= PEI and XX is amine loading in mmol/g MOF

A.4. N_2 physisorption of MIL-101 (Cr) and PEI-800 functionalized samples

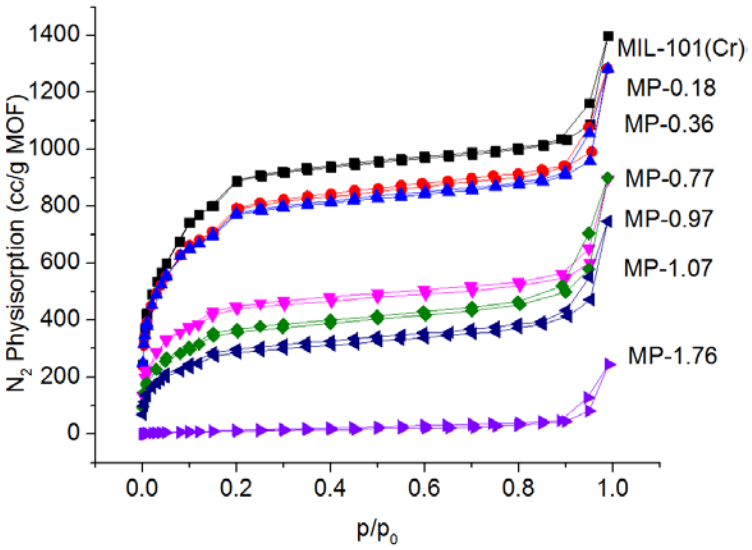

Figure A.5 N_2 physisorption isotherms for MIL-101(Cr) and MIL-101(Cr)-PEI-800. Samples are labelled as MP-XX, M= MIL-101(Cr), P= PEI and XX is amine loading in mmol/g MOF

A.5. Elemental Analysis

Percentage of C, H, and N in MIL-101(Cr) and MIL-101(Cr) functionalized with tris-2-amino ethyl amine and poly(ethylene imine) (PEI)-800

Table A. 1 Elemental Analysis for MIL-101(Cr) functionalized with TREN and PEI-800

Material	Amine Loadings (mmol/g MOF)	C %	H %	N % (Amines)
MIL-101(Cr)	N/A	35.05	3.07	2.51 (DMF)
MIL-101(Cr)-TREN-grafted	2.63	41.89	5.19	10.63
MIL-101(Cr)-TREN-impregnated	5.6 (theoretical)	---	-----	-----

Table A.1. continued from Page 148				
MIL-101(Cr)-PEI	0.18	40.54	4.52	4.22
	0.36	42.3	5.22	7.49
	0.77	43.34	6.19	12.76
	0.97	43.80	6.68	14.60
	1.06	44.80	6.62	15.36
	1.32	41.94	7.60	17.22
	1.76	46.74	7.5	19.59

Note: Because a strong leaching of amines, the C, H, N values for MIL-101(Cr)-TREN-impregnated high loading materials were not accurate and hence are not reported here. The observed nitrogen in MIL-101 is attributed to the presence of DMF in the MOF material. This was taken into account while calculating the amine loadings for the amine functionalized materials.

A.6. BET Surface area after functionalization with amines.

Table A. 2 BET Surface areas for MIL-101(Cr)-PEI-800 samples as a function of PEI loading. Samples are labelled as MP-XX; M= MIL-101(Cr), P= PEI and XX is amine loading in mmol/g MOF

Sample Name	BET Surface Area (m^2/g material)
MIL-101(Cr)	3340
MP-0.18	2480
MP-0.36	2140
MP-0.77	1055
MP-0.97	727
MP-1.07	560
MP-1.76	31

N_2 physisorption and BET surface area decreased progressively as amine loadings are increased.

Figure A6 denotes the change the in the weight of MIL-101(Cr)-TREN-impregnated as a function of time on TGA. Continuous decrease in the baseline indicates the leaching of TREN in the structure.

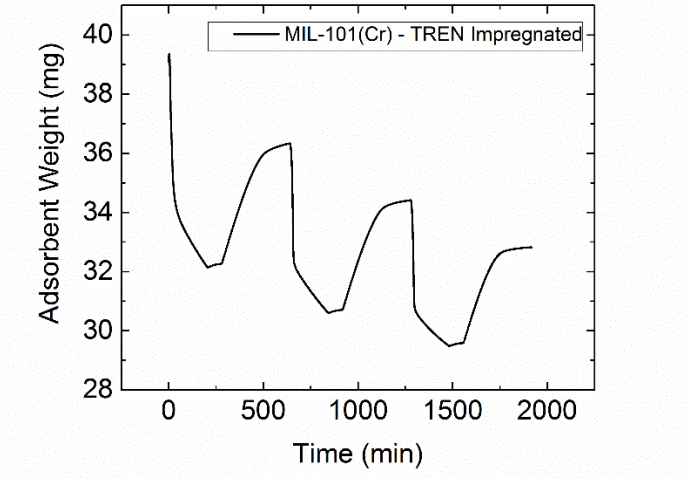

Figure A.6 Weight of adsorbent (mg) vs Time (min). Loss in the baseline indicates leaching of amine in the adsorbent

APPENDIX B SUPPLEMENTARY INFORMATION TO CHAPTER 3

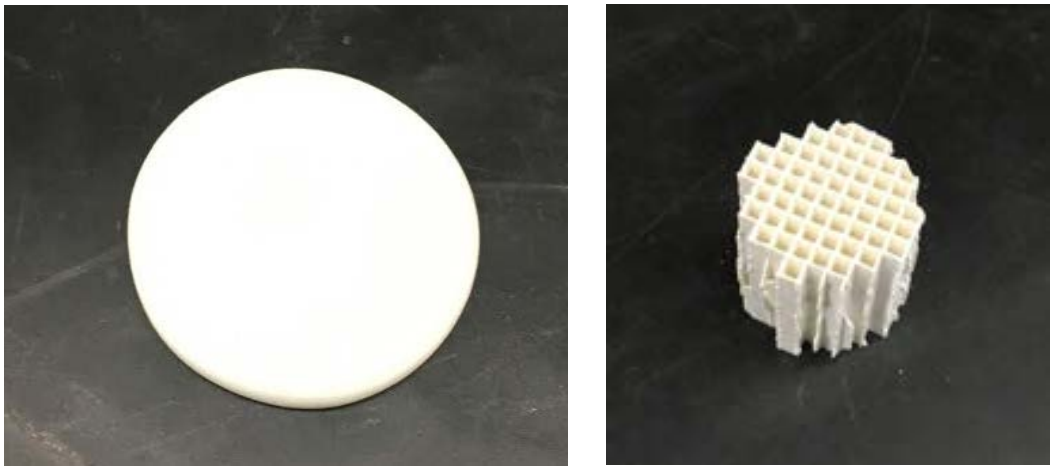

Figure B.1 Flat α-alumina support (left) in plate form used for X-ray diffraction analysis of the Mg_2(dobopdc) and the 100 CPSI cordierite monolith wash-coated with α-alumina (right) used to grow Mg_2(dobpdc) functionalized with mmen.

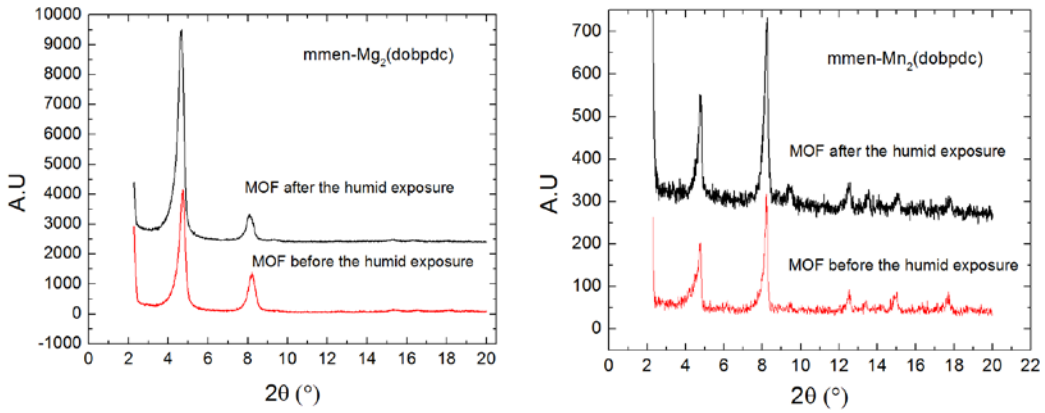

Figure B.2 PXRD patterns for mmen-Mg_2(dobpdc) powder (left) and mmen-Mn_2(dobpdc) (right) before and after exposure to humidity.

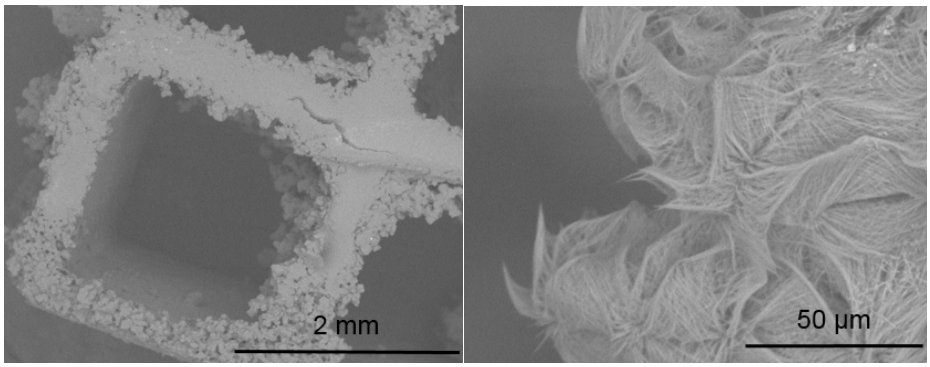

Figure B.3 Mg_2(dobpdc) film grown on the monolith via hydrothermal synthesis.

Conventional hydrothermal synthesis produced a non-uniform film on the monolith surface with poor adhesion to the substrate.

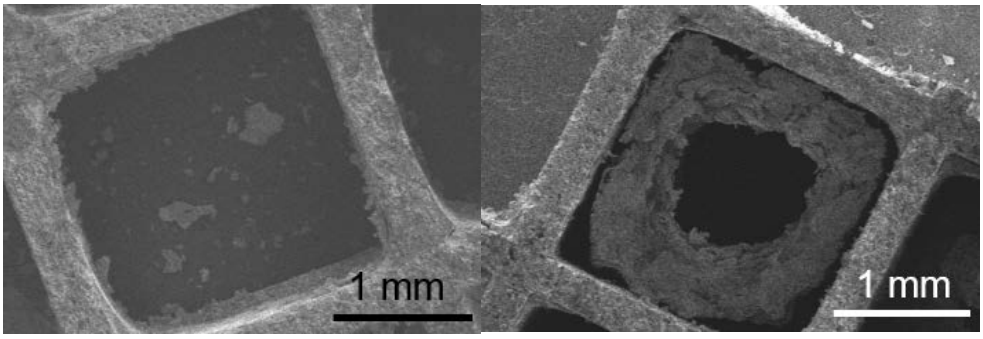

Figure B.4 MgO nanoparticles were deposited from a slurry in water followed by different drying techniques: Oven drying at 100 °C (left), freeze drying (right). The former resulted in a poor film, and the latter in excessive deposition with adhesion.

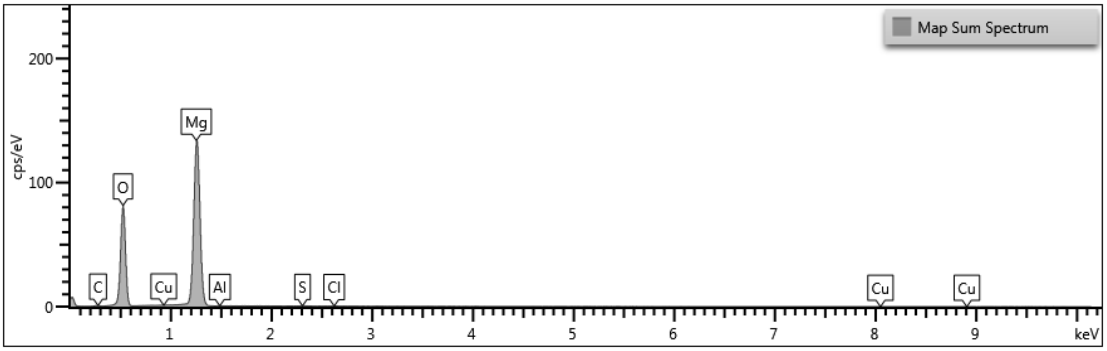

Figure B.5 Surface composition through EDX measurement for the MgO seed layer on the monolith prepared from the solution of MgO in methanol and PEI. The surface mainly consists of Mg and O.

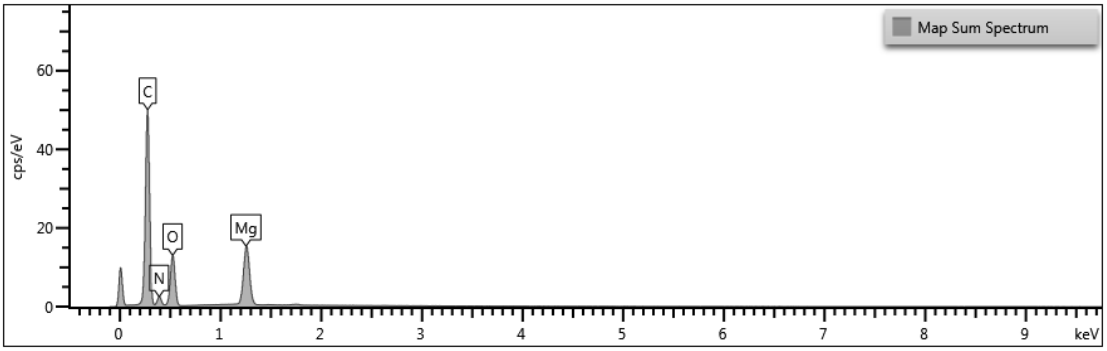

Figure B.6 Surface composition through EDX measurement for mmen-Mg_2(dobpdc)prepared from the MgO seed layer on the monolith using a solution of MgO in methanol and PEI. The surface mainly consists of C, Mg, O and N.

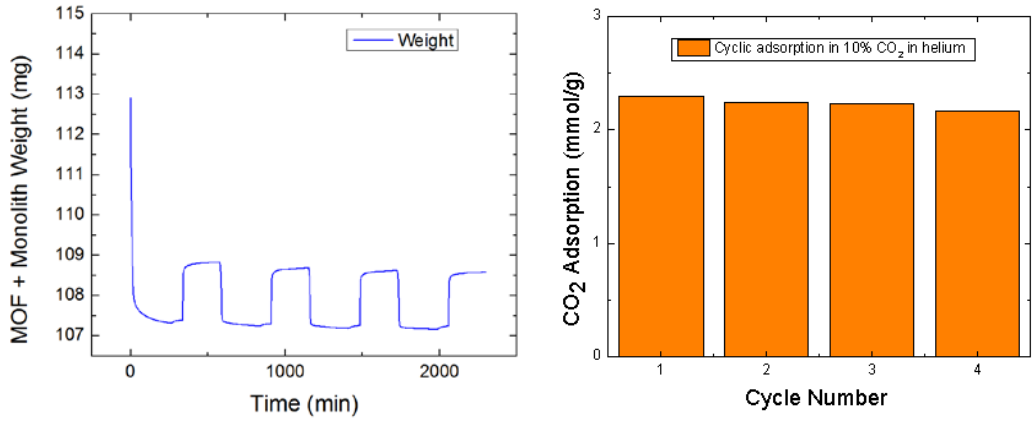

Figure B.7 Adsorption-desorption cycles (left) and cyclic CO_2 adsorption capacities (right) for mmen-Mg_2(dobpdc) film grown on a monolith on the thermogravimetric analyzer (TGA) in 10% CO_2 in helium.

APPENDIX C SUPPLEMENTARY INFORMATION FOR CHAPTER 5

C.1. Detailed isotherm model

The detailed isotherm model is presented in equations S1-S10. Transition pressure is given by equation S1.

$$p_{step} = p_0 \exp\left(-\frac{\Delta H_{step}}{R}\left(\frac{1}{T_0} - \frac{1}{T_g}\right)\right) \quad \text{(S1)}$$

Total adsorption is a weighted sum of adsorption of two adsorption mechanisms where adsorption before and after the transition step is represented by Langmuir isotherms.

$$q_1^* = q_{Low}(1 - w) + q_{sat} w \quad \text{(C2)}$$

$$q_2^* = q_{High} w \quad \text{(C3)}$$

$$q_{Low} = \frac{q_L b_L p}{1 + b_L p} \quad \text{(C4)}$$

$$q_{High} = \frac{q_H b_H p}{1 + b_H p} + q_U p \quad \text{(C5)}$$

$$\sigma = \lambda_1 \exp\left(\lambda_2 \left(\frac{1}{T_0} - \frac{1}{T_g}\right)\right) \quad \text{(C6)}$$

$$q_{sat} = \frac{q_L b_L p_{step}}{1 + b_L p_{step}} \quad \text{(C8)}$$

Weighted function given by equation C9 is used to find net adsorption of CO_2 at a given partial pressure.

$$w = \left(\frac{\exp\left(\frac{\log(p) - \log(p_{step})}{\sigma}\right)}{1 + \exp\left(\frac{\log(p) - \log(p_{step})}{\sigma}\right)} \right)^{\gamma} \quad \text{(C9)}$$

$$b_L = b_{L0} \exp\left(\frac{\Delta H_L}{RT_g}\right) \quad \text{(C10)}$$

$$b_H = b_{H0} \exp\left(\frac{\Delta H_H}{RT_g}\right) \quad \text{(C11)}$$

$$q_U = q_{U0} \exp\left(\frac{\Delta H_u}{RT_g}\right) \quad \text{(C12)}$$

Table C.1. Parameters used to for the experimental isotherm along with the temperature dependence of them.

Parameter	Values used in the simulation
T_0	313.5 K
p_0	0.78 mbar
q_L	0.26 mol/kg
b_{L0}	6.36×10^{-8} mbar^{-1}
q_H	3.14 mol/kg
b_{H0}	2.94×10^{-9} mbar^{-1}
q_{U0}	1.31×10^{-7} (mol/kg). mbar^{-1}
λ_1	2.43×10^{2}
ΔH_{step}	$-68.2\ kJ/mol$
ΔH_L	$45\ kJ/mol$
ΔH_h	$54.6\ kJ/mol$
ΔH_u	$21.8\ kJ/mol$
λ_2	$4.09\ kJ/mol$

C.2. Estimation of dispersion coefficient in the bed

Dispersion in the bed is modeled using Wakao & Funazkri empirical correlation.

$$D_{ax} = (20 + 0.5 S_c Re)\frac{Dmol}{\varepsilon} \quad \text{(C13)}$$

$$\lambda = (7 + 0.5 PrRe)K_{mix} \quad \text{(C14)}$$

$$\text{Where } e = \frac{\rho_g v 2 R_p}{\mu_g}, Sc = \frac{\mu_g}{\rho_g D_{mol}} \ \& \ Pr = \frac{\mu_g}{K_{mix}} \frac{C_{p,T}}{Mw_{mix}} \quad \text{(C15)}$$

C.3. Detailed kinetic model for cooperative binding

Cooperative binding of molecular B into multisite substrate A with n sites can be modeled with following scheme. Rate constant for binding of first molecule B onto the first site A1 is k_1. Because of cooperative binding, rate constant of binding of subsequent B molecules onto the oligomer is k_2. For the case of positive cooperativity, $k_2 >> k_1$. This may lead to low concentration of intermediates. Equations C16 to C28 represent the reaction scheme for cooperative insertion of CO_2 here modeled as molecule B.

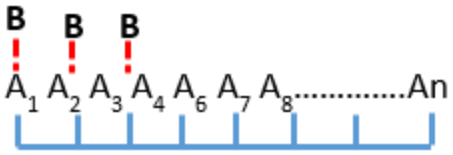

Figure C.1 Cooperative binding of molecule B into a substrate with multiple cooperative sites

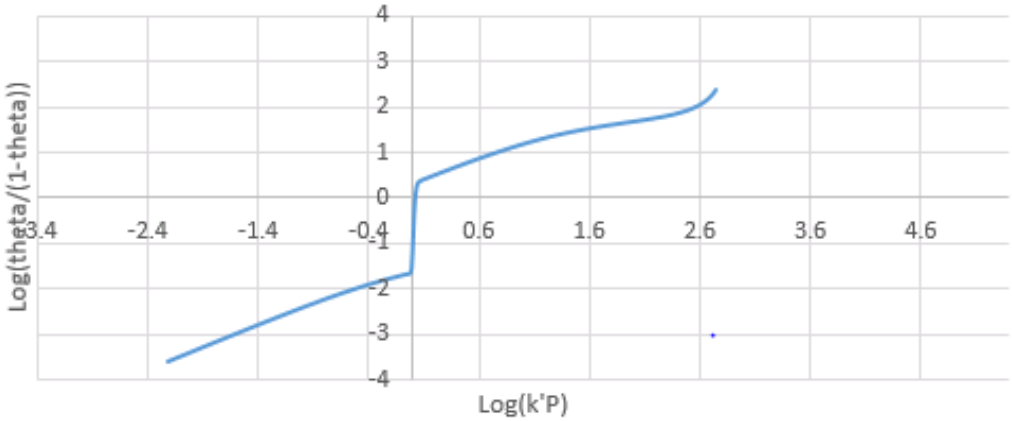

Figure C. 2 Hill plot for adsorption of CO_2 in mmen-Mg_2(dobpdc) based on the isotherm in Figure 5.5. Slope of 23 at the origin indicates a strong cooperative binding

$$(A)_n + B \underset{k_{-1}}{\overset{k_1}{\rightleftharpoons}} (A)_n \bullet B \quad . \tag{C16}$$

$$(A)_n \bullet B + B \underset{k_{-2}}{\overset{k_2}{\rightleftharpoons}} (A)_n \bullet (B)_2 \tag{C17}$$

$$(A)_n \bullet (B)_2 + B \underset{k_{-2}}{\overset{k_2}{\rightleftharpoons}} (A)_n \bullet (B)_3 \tag{C18}$$

$$(A)_n (B)_{n-1} + B \underset{k_{-2}}{\overset{k_2}{\dashrightarrow}} (A)_n (B)_{n-1} \tag{C19}$$

Rate of reactions can be written as follows where reaction 1 is rate limiting

$$r_1 = k_1 * (A)_n * B \; - k_{-1} * (A)_n B \textbf{ (rate determining step)} \quad \text{(C20)}$$

$$r_2 = k_2 * (A)_n * B * B \; - k_{-2} * (A)_n (B)_2 \quad \text{(C21)}$$

If the rate constant k_2 of the reaction is large then $r_2/k_2 = 0$,

$$[(\mathrm{A})_\mathrm{n}(\mathrm{B})2] = \mathrm{K}_2[(\mathrm{A})_\mathrm{n}\mathrm{B}][\mathrm{B}] \quad \text{(C22)}$$

Where $K_2 = k_2/k_{-2}$

Concentrations for other intermediates can be deduced in a similar manner.

$$[(\mathrm{A})_\mathrm{n}(\mathrm{B})3] = \mathrm{K}_2^2[(\mathrm{A})_\mathrm{n}\mathrm{B}][\mathrm{B}] \quad \text{(C23)}$$

$$[(\mathrm{A})_\mathrm{n}(\mathrm{B})\mathrm{n}] = \mathrm{K}_2^{\mathrm{n}-1}[(\mathrm{A})_\mathrm{n}\mathrm{B}][\mathrm{B}] \quad \text{(C24)}$$

Total site balance for n site substrate is as follows

$$[(A)_\mathrm{n}]0 = [(A)_\mathrm{n}] + [(A)_\mathrm{n}B][1 + \mathrm{K}_2\mathrm{B} + \mathrm{K}_2^2\mathrm{B}^2 + \cdots + \mathrm{K}_2^{(\mathrm{n}-1)}\mathrm{B}^{(\mathrm{n}-1)}] \quad \text{(C25)}$$

$$(\mathrm{A})_\mathrm{n}\mathrm{B} = \frac{[(\mathrm{A})_\mathrm{n}]_0 - [(\mathrm{A})_\mathrm{n}]}{[1 + \mathrm{K}_2\mathrm{B} + \mathrm{K}_2^2\mathrm{B}^2 + \cdots + \mathrm{K}_2^{(\mathrm{n}-1)}\mathrm{B}^{(\mathrm{n}-1)}]} \quad \text{(C26)}$$

Now we will revisit the equation for rate determining step as follows:

$$r_1 = k_1 * (A)_n * B \; - k_{-1} * (A)_n B$$

$$r_1 = k_1 * (A)_n * B \; - k_{-1} * \frac{[(A)_n]_0 - [(A)_n]}{\left[1 + K_2 B + K_2^2 B^2 + \cdots + K_2^{(n-1)} B^{(n-1)}\right]} \quad \text{(C27)}$$

In presence of cooperative binding, rate of reverse reactions rate decreases, so net reaction rate becomes.

$$r_1 = k_1 * (A)_n * B \qquad \text{(C28)}$$

Kinetics modeling of resultant breakthrough profile

Experimental (scatter) and simulated breakthrough profiles (solid lines) for CO_2 adsorption with the partial pressure of 0.4 mBar in the feed is presented in Figure 2 and 3. Simulated profiles were obtained at the flowrate of 17.2 mL/min, 28.2 mL/min, 48.6 mL/min and 100 mL/min at 23 °C. Linear driving force model with a zero order (Figure C.3. left), a first order (Figure C.3. right) and a third order rate dependence (Figure C.4.) on CO_2 concentration was used in this analysis to account for the cooperative CO_2 binding.

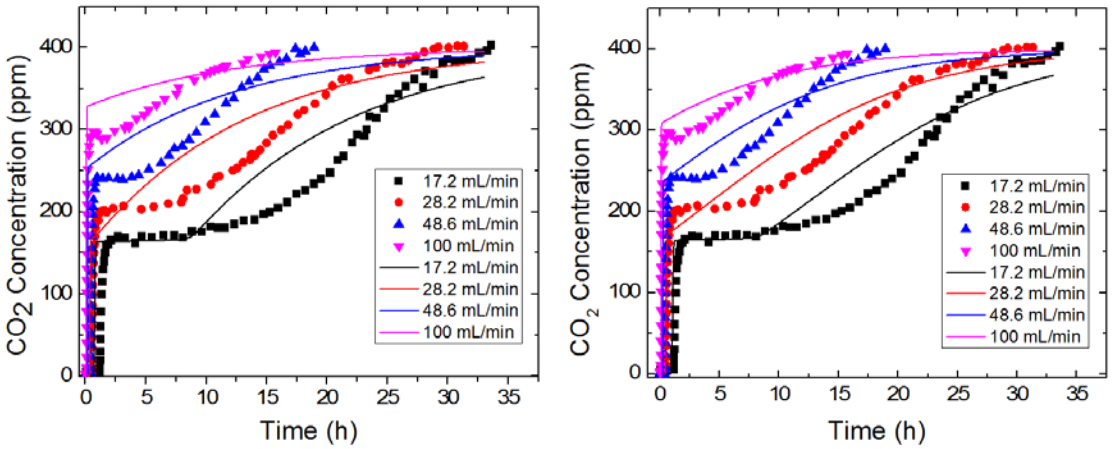

Figure C.3 Experimental (scatter) and simulated breakthrough profiles (solid lines) for CO_2 adsorption with the partial pressure of 0.4 mBar in the feed. Simulated profiles were obtained at the flowrate of 17.2 mL/min, 28.2 mL/min, 48.6 mL/min and 100 mL/min at 23 °C. Linear driving force model with a zero order (left) and first order rate dependence (right) CO_2 concentration was used in this analysis to account for the cooperative CO_2 binding.

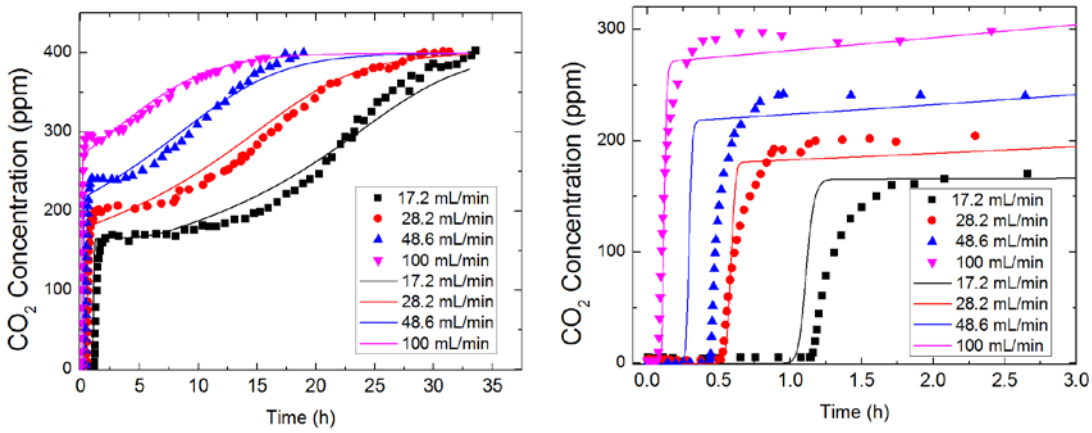

Figure C.4 Experimental (scatter) and simulated breakthrough profiles (solid lines) for CO_2 adsorption with the partial pressure of 0.4 mBar in the feed. Simulated profiles were obtained at the flowrate of 17.2 mL/min, 28.2 mL/min, 48.6 mL/min and 100 mL/min at 23 °C. Linear driving force model with a third order rate dependence CO_2 concentration was used in this analysis to account for the cooperative CO_2 binding.The data for first 3 h of adsorption is presented in the right figure.

APPENDIX D PUBLISHED WORK

Title	**CO_2 Capture via Adsorption in Amine-functionalized Sorbents**
Authors	Lalit A. Darunte, Krista S. Walton, David S.Sholl, and Christopher W. Jones
Source	Current Opinion in Chemical Engineering 2016, 12, pp 82-90.

Title	**Direct Air Capture of CO_2 Using Amine-Functionalized MIL-101(Cr)**
Authors	Lalit A. Darunte, Davin A. Oetomo, Krista S. Walton, David S. Sholl, and Christopher W. Jones
Source	ACS Sustainable Chemistry & Engineering 2016, 4 (10), pp 5761–5768

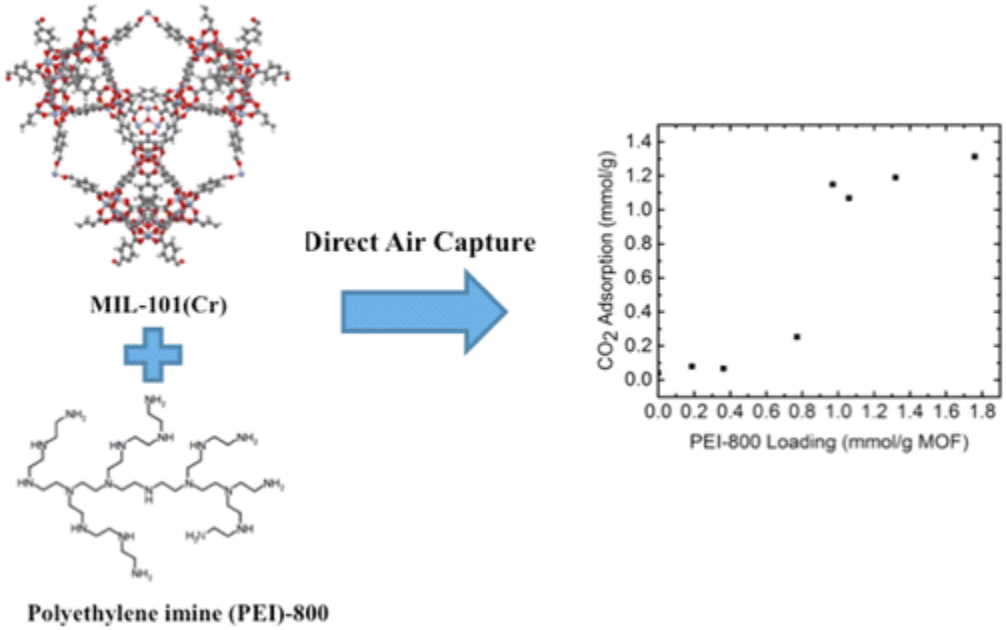

Title	**Monolith-Supported Amine-Functionalized Mg_2(dobpdc) Adsorbents for CO_2 Capture**
Authors	Lalit A. Darunte, Yuri Terada, Krista S. Walton, David S.Sholl, and Christopher W. Jones
Source	ACS Applied Materials & Interfaces 2017,9 (20), pp 17042–17050

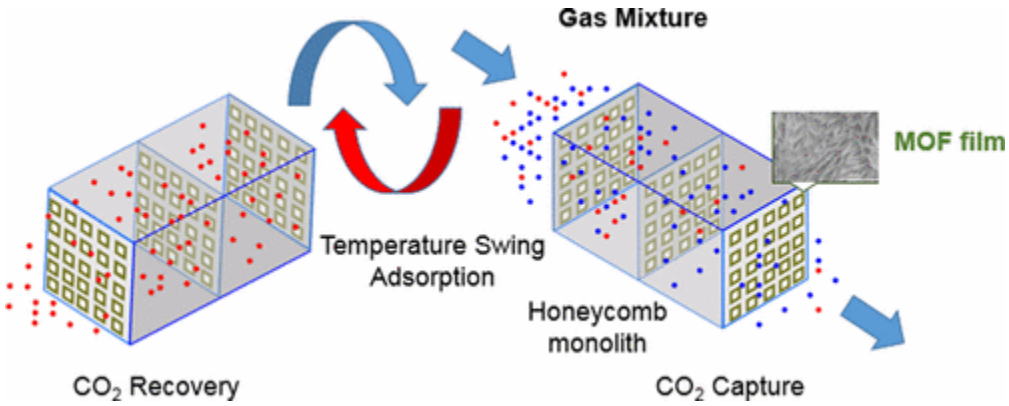

Title	**Systems Design and Economic Analysis of Direct Air Capture of CO_2 through Temperature Vacuum Swing Adsorption using MIL-101(Cr)-PEI-800 and mmen-Mg_2(dobpdc) MOF adsorbents**
Authors	Anshuman Sinha, Lalit A. Darunte, Christopher W. Jones, Matthew J. Realff, and Yoshiaki Kawajiri
Source	Industrial & Engineering Chemistry Research